Title
Measurement of electron antineutrino oscillation based on 1230 days of operation of the Daya Bay experiment

Authors
An, FP
Balantekin, AB
Band, HR
et al.

Peer reviewed

Measurement of electron antineutrino oscillation based on 1230 days of operation of the Daya Bay experiment

F. P. An,[1] A. B. Balantekin,[2] H. R. Band,[3] M. Bishai,[4] S. Blyth,[5,6] D. Cao,[7] G. F. Cao,[8] J. Cao,[8] W. R. Cen,[8] Y. L. Chan,[9] J. F. Chang,[8] L. C. Chang,[10] Y. Chang,[6] H. S. Chen,[8] Q. Y. Chen,[11] S. M. Chen,[12] Y. X. Chen,[13] Y. Chen,[14] J.-H. Cheng,[10] J. Cheng,[11] Y. P. Cheng,[8] Z. K. Cheng,[15] J. J. Cherwinka,[2] M. C. Chu,[9] A. Chukanov,[16] J. P. Cummings,[17] J. de Arcos,[18] Z. Y. Deng,[8] X. F. Ding,[8] Y. Y. Ding,[8] M. V. Diwan,[4] M. Dolgareva,[16] J. Dove,[19] D. A. Dwyer,[20] W. R. Edwards,[20] R. Gill,[4] M. Gonchar,[16] G. H. Gong,[12] H. Gong,[12] M. Grassi,[8] W. Q. Gu,[21] M. Y. Guan,[8] L. Guo,[12] X. H. Guo,[22] Z. Guo,[12] R. W. Hackenburg,[4] R. Han,[13] S. Hans,[4,*] M. He,[8] K. M. Heeger,[3] Y. K. Heng,[8] A. Higuera,[23] Y. K. Hor,[24] Y. B. Hsiung,[5] B. Z. Hu,[5] T. Hu,[8] W. Hu,[8] E. C. Huang,[19] H. X. Huang,[25] X. T. Huang,[11] P. Huber,[24] W. Huo,[26] G. Hussain,[12] D. E. Jaffe,[4] P. Jaffke,[24] K. L. Jen,[10] S. Jetter,[8] X. P. Ji,[27,12] X. L. Ji,[8] J. B. Jiao,[11] R. A. Johnson,[28] D. Jones,[29] J. Joshi,[4] L. Kang,[30] S. H. Kettell,[4] S. Kohn,[31] M. Kramer,[20,31] K. K. Kwan,[9] M. W. Kwok,[9] T. Kwok,[32] T. J. Langford,[3] K. Lau,[23] L. Lebanowski,[12] J. Lee,[20] J. H. C. Lee,[32] R. T. Lei,[30] R. Leitner,[33] J. K. C. Leung,[32] C. Li,[11] D. J. Li,[26] F. Li,[8] G. S. Li,[21] Q. J. Li,[8] S. Li,[30] S. C. Li,[32,24] W. D. Li,[8] X. N. Li,[8] Y. F. Li,[8] Z. B. Li,[15] H. Liang,[26] C. J. Lin,[20] G. L. Lin,[10] S. Lin,[30] S. K. Lin,[23] Y.-C. Lin,[5] J. J. Ling,[15] J. M. Link,[24] L. Littenberg,[4] B. R. Littlejohn,[18] D. W. Liu,[23] J. L. Liu,[21] J. C. Liu,[8] C. W. Loh,[7] C. Lu,[34] H. Q. Lu,[8] J. S. Lu,[8] K. B. Luk,[31,20] Z. Lv,[35] Q. M. Ma,[8] X. Y. Ma,[8] X. B. Ma,[13] Y. Q. Ma,[8] Y. Malyshkin,[36] D. A. Martinez Caicedo,[18] K. T. McDonald,[34] R. D. McKeown,[37,38] I. Mitchell,[23] M. Mooney,[4] Y. Nakajima,[20] J. Napolitano,[29] D. Naumov,[16] E. Naumova,[16] H. Y. Ngai,[32] Z. Ning,[8] J. P. Ochoa-Ricoux,[36] A. Olshevskiy,[16] H.-R. Pan,[5] J. Park,[24] S. Patton,[20] V. Pec,[33] J. C. Peng,[19] L. Pinsky,[23] C. S. J. Pun,[32] F. Z. Qi,[8] M. Qi,[7] X. Qian,[4] N. Raper,[39] J. Ren,[25] R. Rosero,[4] B. Roskovec,[33] X. C. Ruan,[25] H. Steiner,[31,20] G. X. Sun,[8] J. L. Sun,[40] W. Tang,[4] D. Taychenachev,[16] K. Treskov,[16] K. V. Tsang,[20] C. E. Tull,[20] N. Viaux,[36] B. Viren,[4] V. Vorobel,[33] C. H. Wang,[6] M. Wang,[11] N. Y. Wang,[22] R. G. Wang,[8] W. Wang,[38,15] X. Wang,[41] Y. F. Wang,[8] Z. Wang,[12] Z. Wang,[8] Z. M. Wang,[8] H. Y. Wei,[12] L. J. Wen,[8] K. Whisnant,[42] C. G. White,[18] L. Whitehead,[23] T. Wise,[2] H. L. H. Wong,[31,20] S. C. F. Wong,[15] E. Worcester,[4] C.-H. Wu,[10] Q. Wu,[11] W. J. Wu,[8] D. M. Xia,[43] J. K. Xia,[8] Z. Z. Xing,[8] J. Y. Xu,[9] J. L. Xu,[8] Y. Xu,[15] T. Xue,[12] C. G. Yang,[8] H. Yang,[7] L. Yang,[30] M. S. Yang,[8] M. T. Yang,[11] M. Ye,[8] Z. Ye,[23] M. Yeh,[4] B. L. Young,[42] Z. Y. Yu,[8] S. Zeng,[8] L. Zhan,[8] C. Zhang,[4] H. H. Zhang,[15] J. W. Zhang,[8] Q. M. Zhang,[35] X. T. Zhang,[8] Y. M. Zhang,[12] Y. X. Zhang,[40] Y. M. Zhang,[15] Z. J. Zhang,[30] Z. Y. Zhang,[8] Z. P. Zhang,[26] J. Zhao,[8] Q. W. Zhao,[8] Y. B. Zhao,[8] W. L. Zhong,[8] L. Zhou,[8] N. Zhou,[26] H. L. Zhuang,[8] and J. H. Zou[8]

(The Daya Bay Collaboration)

[1]*Institute of Modern Physics, East China University of Science and Technology, Shanghai*
[2]*University of Wisconsin, Madison, Wisconsin 53706, USA*
[3]*Department of Physics, Yale University, New Haven, Connecticut 06520, USA*
[4]*Brookhaven National Laboratory, Upton, New York 11973, USA*
[5]*Department of Physics, National Taiwan University, Taipei*
[6]*National United University, Miao-Li*
[7]*Nanjing University, Nanjing*
[8]*Institute of High Energy Physics, Beijing*
[9]*Chinese University of Hong Kong, Hong Kong*
[10]*Institute of Physics, National Chiao-Tung University, Hsinchu*
[11]*Shandong University, Jinan*
[12]*Department of Engineering Physics, Tsinghua University, Beijing*
[13]*North China Electric Power University, Beijing*
[14]*Shenzhen University, Shenzhen*
[15]*Sun Yat-Sen (Zhongshan) University, Guangzhou*
[16]*Joint Institute for Nuclear Research, Dubna, Moscow Region*
[17]*Siena College, Loudonville, New York 12211, USA*
[18]*Department of Physics, Illinois Institute of Technology, Chicago, Illinois 60616, USA*
[19]*Department of Physics, University of Illinois at Urbana-Champaign, Urbana, Illinois 61801, USA*
[20]*Lawrence Berkeley National Laboratory, Berkeley, California 94720, USA*
[21]*Department of Physics and Astronomy, Shanghai Jiao Tong University, Shanghai Laboratory for Particle Physics and Cosmology, Shanghai*
[22]*Beijing Normal University, Beijing*
[23]*Department of Physics, University of Houston, Houston, Texas 77204, USA*
[24]*Center for Neutrino Physics, Virginia Tech, Blacksburg, Virginia 24061, USA*
[25]*China Institute of Atomic Energy, Beijing*
[26]*University of Science and Technology of China, Hefei*
[27]*School of Physics, Nankai University, Tianjin*
[28]*Department of Physics, University of Cincinnati, Cincinnati, Ohio 45221, USA*
[29]*Department of Physics, College of Science and Technology, Temple University, Philadelphia, Pennsylvania 19122, USA*
[30]*Dongguan University of Technology, Dongguan*

[31]*Department of Physics, University of California, Berkeley, California 94720, USA*
[32]*Department of Physics, The University of Hong Kong, Pokfulam, Hong Kong*
[33]*Charles University, Faculty of Mathematics and Physics, Prague, Czech Republic*
[34]*Joseph Henry Laboratories, Princeton University, Princeton, New Jersey 08544, USA*
[35]*Xi'an Jiaotong University, Xi'an*
[36]*Instituto de Física, Pontificia Universidad Católica de Chile, Santiago, Chile*
[37]*California Institute of Technology, Pasadena, California 91125, USA*
[38]*College of William and Mary, Williamsburg, Virginia 23187, USA*
[39]*Department of Physics, Applied Physics, and Astronomy, Rensselaer Polytechnic Institute, Troy, New York 12180, USA*
[40]*China General Nuclear Power Group*
[41]*College of Electronic Science and Engineering, National University of Defense Technology, Changsha*
[42]*Iowa State University, Ames, Iowa 50011, USA*
[43]*Chongqing University, Chongqing*
(Dated: October 18, 2016)

A measurement of electron antineutrino oscillation by the Daya Bay Reactor Neutrino Experiment is described in detail. Six 2.9-$\mathrm{GW_{th}}$ nuclear power reactors of the Daya Bay and Ling Ao nuclear power facilities served as intense sources of $\overline{\nu}_e$'s. Comparison of the $\overline{\nu}_e$ rate and energy spectrum measured by antineutrino detectors far from the nuclear reactors ($\sim$1500-1950 m) relative to detectors near the reactors ($\sim$350-600 m) allowed a precise measurement of $\overline{\nu}_e$ disappearance. More than 2.5 million $\overline{\nu}_e$ inverse beta decay interactions were observed, based on the combination of 217 days of operation of six antineutrino detectors (Dec. 2011–Jul. 2012) with a subsequent 1013 days using the complete configuration of eight detectors (Oct. 2012–Jul. 2015). The $\overline{\nu}_e$ rate observed at the far detectors relative to the near detectors showed a significant deficit, $R = 0.949 \pm 0.002(\text{stat.}) \pm 0.002(\text{syst.})$. The energy dependence of $\overline{\nu}_e$ disappearance showed the distinct variation predicted by neutrino oscillation. Analysis using an approximation for the three-flavor oscillation probability yielded the flavor-mixing angle $\sin^2 2\theta_{13} = 0.0841 \pm 0.0027(\text{stat.}) \pm 0.0019(\text{syst.})$ and the effective neutrino mass-squared difference of $\left|\Delta m^2_{\text{ee}}\right| = (2.50 \pm 0.06(\text{stat.}) \pm 0.06(\text{syst.})) \times 10^{-3} \text{ eV}^2$. Analysis using the exact three-flavor probability found $\Delta m^2_{32} = (2.45 \pm 0.06(\text{stat.}) \pm 0.06(\text{syst.})) \times 10^{-3} \text{ eV}^2$ assuming the normal neutrino mass hierarchy and $\Delta m^2_{32} = (-2.56 \pm 0.06(\text{stat.}) \pm 0.06(\text{syst.})) \times 10^{-3} \text{ eV}^2$ for the inverted hierarchy.

CONTENTS

* Now at Department of Chemistry and Chemical Technology, Bronx Community College, Bronx, New York 10453, USA

I. INTRODUCTION

Recent experiments have resulted in significant advances in our understanding of neutrinos. Although neutrinos were considered massless within the Standard Model, abundant evidence of lepton flavor violation by neutrinos strongly implies small but non-zero masses. A long-standing disparity between measurement and models of the solar ν_e flux was corroborated by successive radiochemical [1–3] and water-Cherenkov [4, 5] experiments. Variation of the ratio of atmospheric ν_μ to ν_e provided initial evidence for distance-dependent neutrino disappearance [6]. Subsequent observation of the disappearance of ν_μ produced in particle accelerators confirmed atmospheric ν measurements [7]. A comparison of the solar ν_e to the total solar ν flux showed that the apparent disappearance was a consequence of the conversion of ν_e's to other neutrino flavors [8, 9]. Disappearance of $\overline{\nu}_e$'s emitted by nuclear reactors demonstrated a distinct dependence on the ratio of propagation distance to antineutrino energy, L/E_ν, cementing neutrino flavor oscillation as the explanation for the observed flavor violation [10].

The rich phenomena of neutrino flavor oscillation arise from two remarkable characteristics of neutrinos: small differences between the masses of the three neutrino states, $m_1 \neq m_2 \neq m_3$, and an inequivalence between neutrino flavor and mass eigenstates. Produced in a flavor eigenstate by the weak interaction, a neutrino state evolves as a coherent superposition of mass eigenstates. Interference between the phases of each mass component results in the oscillation of the neutrino flavor. The flavor oscillates with phases given by $\Delta m_{ji}^2 L/4E_\nu$, where L is the propagation distance, E_ν is the neutrino energy, and $\Delta m_{ji}^2 = m_j^2 - m_i^2$ is the difference of the squared masses. The amplitude of flavor oscillation is determined by the amount of mixing between the flavor and mass eigenstates. Using the unitary Pontecorvo-Maki-Nakagawa-Sakata (PMNS) matrix, $U_{\rm PMNS}$, a neutrino with flavor α can be expressed as a combination of mass states, $|\nu_\alpha\rangle = \sum_i U_{\alpha i}^* |\nu_i\rangle$. In the three-flavor model, $U_{\rm PMNS}$ is commonly parameterized using three mixing angles, θ_{12}, θ_{23}, θ_{13}, and an off-diagonal CP-violating phase $\delta_{\rm CP}$. With sensitivity to the small neutrino mass separations, oscillation experiments have provided strong evidence for three distinct neutrino mass states ν_i with masses m_1, m_2, and m_3. Evidence for matter-enhanced resonant flavor conversion of solar neutrinos has shown that $\Delta m_{21}^2 \cos(2\theta_{21}) > 0$. Whether m_3 is much lighter or heavier than m_1 and m_2, also referred to as the neutrino mass hierarchy, is currently unknown and is the focus of a broad experimental program [11]. Direct measurements of decay kinematics and indirect cosmological observations are currently consistent with massless neutrinos, implying that the absolute masses are less than $\sim$1 eV. Neutrino mass qualitatively alters the Standard Model, for example by inhibiting renormalization or by requiring a new global symmetry [12, 13].

The Daya Bay Reactor Neutrino Experiment set out to answer the question: Does the ν_3 mass eigenstate mix with the electron neutrino state ν_e? This is equivalent to asking whether the parameter θ_{13} is non-zero. Solar

and reactor experiments have established significant mixing between the ν_e and $\nu_{1,2}$ states, given by $\sin^2(2\theta_{12}) = 0.846 \pm 0.021$ [14]. Atmospheric and accelerator experiments yielded nearly maximal mixing of the ν_μ and $\nu_{2,3}$ states, with $\sin^2(2\theta_{23}) = 0.999^{+0.001}_{-0.018}$ [14]. Previous searches found no evidence of $\overline{\nu}_e$ disappearance at $\sim$1 km from reactors, limiting $\sin^2 2\theta_{13} \leq 0.17$ at the 90% C.L. [15, 16]. Measurement of θ_{13} provides a key parameter of a new Standard Model which incorporates massive neutrinos, and may allow a deeper insight into the flavor and mass structure of nature. A non-zero value for θ_{13} also makes it possible for future experiments to determine the neutrino mass hierarchy and to search for neutrino CP-violation [11].

Nuclear reactors produce an intense and pure flux of $\overline{\nu}_e$'s, which is useful for experimental searches for θ_{13}. Approximately 2×10^{20} $\overline{\nu}_e$'s per second are emitted per gigawatt of thermal power, with a steeply-falling energy spectrum showing minuscule flux above 10 MeV. Section V gives further details of $\overline{\nu}_e$ emission by nuclear reactors. Reactor $\overline{\nu}_e$ are most commonly detected via inverse beta decay (IBD),

$$\overline{\nu}_e + p \to e^+ + n. \tag{1}$$

Convolving the energy spectrum with the IBD cross-section [17] results in an expected spectrum which rises with neutrino energy from the 1.8 MeV interaction threshold, peaks at $\sim$4 MeV, and falls to a very low rate above 8 MeV. Charge-current interactions of $\overline{\nu}_\mu$ or $\overline{\nu}_\tau$ at these energies are forbidden by energy conservation, hence oscillation is observed as a reduction, or *disappearance*, of the expected $\overline{\nu}_e$ signal. In the three-flavor model of neutrino oscillation, the survival probability of detecting an $\overline{\nu}_e$ of energy E_ν at a distance L from the production source can be expressed as

$$
\begin{aligned}
P_{\rm sur} =\ & 1 - \cos^4\theta_{13}\sin^2 2\theta_{12}\sin^2\Delta_{21} \\
& - \sin^2 2\theta_{13}(\cos^2\theta_{12}\sin^2\Delta_{31} + \sin^2\theta_{12}\sin^2\Delta_{32}),
\end{aligned}
\tag{2}
$$

where $\Delta_{ji} \simeq 1.267\Delta m_{ji}^2(\text{eV}^2)L(\text{m})/E_\nu(\text{MeV})$. The KamLAND experiment measured the first term, demonstrating large-amplitude disappearance of reactor $\overline{\nu}_e$ with an oscillation length of $\sim$60 km. Atmospheric and accelerator ν measurements of $\left|\Delta m_{32}^2\right|$ predict an oscillation length of $\sim$1.6 km for the latter terms. At this distance, the two oscillation phases Δ_{31} and Δ_{32} are indistinguishable. Therefore, the expression can be approximated using a single effective $\overline{\nu}_e$ disappearance phase $\Delta_{\rm ee}$,

$$
\begin{aligned}
P_{\rm sur} \simeq\ & 1 - \cos^4\theta_{13}\sin^2 2\theta_{12}\sin^2\Delta_{21} \\
& - \sin^2 2\theta_{13}\sin^2\Delta_{\rm ee},
\end{aligned}
\tag{3}
$$

which is independent of the neutrino mass hierarchy. Here the definition of $\Delta m_{\rm ee}^2$ is empirical; it is the mass-squared difference obtained by modeling the observed reactor $\overline{\nu}_e$ disappearance using Eq. 3. The mass-squared differences obtained by modeling an observation using either Eq. 2 or Eq. 3 are expected to follow the relation $\Delta m_{\rm ee}^2 \simeq$

$\cos^2\theta_{12}\left|\Delta m_{31}^2\right| + \sin^2\theta_{12}\left|\Delta m_{32}^2\right|$ [18]. Based on current measurements, $\left|\Delta m_{31}^2\right| \simeq \left|\Delta m_{ee}^2\right| \pm 2.3 \times 10^{-5}$ eV^2 and $\left|\Delta m_{32}^2\right| \simeq \left|\Delta m_{ee}^2\right| \mp 5.2 \times 10^{-5}$ eV^2, assuming the normal (upper sign) or inverted (lower sign) mass hierarchy.

Previous searches for oscillation due to θ_{13} were limited by uncertainty in the $\overline{\nu}_e$ flux emitted by reactors [15, 16]. A differential comparison with an additional detector located near the reactor was proposed to overcome this uncertainty [19]. With a far-versus-near detector arrangement, sensitivity to neutrino oscillation depends on relative uncertainties between detectors in the number of target protons N_p, $\overline{\nu}_e$ detection efficiency ϵ, and distances from the reactor L. If these relative uncertainties are well-controlled, small differences in the oscillation survival probability P_{sur} become detectable in the ratio of the number of $\overline{\nu}_e$ interactions in the far relative to near detector,

$$\frac{N_f}{N_n} = \left(\frac{N_{p,f}}{N_{p,n}}\right)\left(\frac{L_n}{L_f}\right)^2\left(\frac{\epsilon_f}{\epsilon_n}\right)\left[\frac{P_{sur}(E_\nu, L_f)}{P_{sur}(E_\nu, L_n)}\right]. \quad (4)$$

Three experiments were constructed based on this technique: the Daya Bay [20], RENO [21], and Double CHOOZ experiments [22]. In Mar. 2012, the Daya Bay experiment reported the discovery of $\overline{\nu}_e$ disappearance due to a non-zero value of θ_{13} [23]. Oscillation due to θ_{13} has since been confirmed by the other experiments [24, 25], as well as by other techniques [26, 27]. The relatively large θ_{13} mixing has also allowed measurement of $\left|\Delta m_{ee}^2\right|$ from the variation of the disappearance probability versus $\overline{\nu}_e$ energy [28]. Compatibility of the mass-squared difference with that obtained from the disappearance of accelerator and atmospheric ν_μ's with GeV-energies firmly establishes the three-flavor model of neutrino mass and mixing.

This paper provides a detailed review of the Daya Bay measurement of neutrino oscillation. Section II gives an overview of the experiment. The calibration and characterization of the experiment are presented in Section III. Identification of reactor $\overline{\nu}_e$ interactions, signal efficiencies, and assessment of backgrounds are discussed in Section IV. Section V presents an analysis of neutrino oscillation using the measured $\overline{\nu}_e$ rate and spectra, while Section VI contains concluding remarks.

II. EXPERIMENT DESCRIPTION

The relative measurement of oscillation, as summarized in Eq. 4, motivated much of the design of the Daya Bay experiment. The disappearance signal is most pronounced at the first oscillation minimum of P_{sur}. Based on existing accelerator and atmospheric ν_μ measurements of Δm_{32}^2, this corresponded to a distance $L_f \approx 1.6$ km for reactor $\overline{\nu}_e$ with a mean energy of ~ 4 MeV. Significant $\overline{\nu}_e$ disappearance in the near detectors would have reduced the overall sensitivity of the far-to-near comparison, so L_n was kept to ~ 500 m or less. The use of identically-designed modular detectors limited variations in relative number of target protons N_p and efficiency ϵ between detectors. Situating detectors at a

sufficient depth underground reduced muon-induced neutrons and short-lived isotopes, the most prominent backgrounds for reactor $\overline{\nu}_e$ detection. Statistical sensitivity increases with $\overline{\nu}_e$ flux, target size, and detector efficiency, arguing for the use of intense reactors and large detectors.

The campus of the Daya Bay nuclear power plant near Shenzhen, China was well-suited for this purpose. At the time of this measurement the facility consisted of six 2.9 GW$_{th}$ pressurized water reactors and produced roughly 3.5×10^{21} $\overline{\nu}_e$/s, making it one of the most intense $\overline{\nu}_e$ sources on Earth. Steep mountains adjacent to the reactors provided ample shielding from muons produced by cosmic ray showers. Underground experimental halls were excavated to accommodate 160 tons of fiducial target mass for $\overline{\nu}_e$ interactions, equally divided between locations near and far from the reactors. With this arrangement, a total of ~ 2000 $\overline{\nu}_e$ interactions per day were detected near to, and ~ 250 far from, the reactors, with muon-induced backgrounds contributing less than 0.5%. The target mass was divided between 8 identically-designed modular antineutrino detectors (ADs). Installing at least two ADs in each experimental hall allowed side-by-side demonstration of $<0.2\%$ variation in $\overline{\nu}_e$ detection efficiency between detectors. A confirmation of the side-by-side performance of the first two ADs was given in [29]. These basic characteristics have yielded measurements of $\sin^2 2\theta_{13}$ with $\sim 4\%$ precision and $\left|\Delta m_{ee}^2\right|$ with $\sim 3\%$ precision, as will be discussed in this paper. This section provides an abbreviated description of the Daya Bay experiment, while a more detailed description is given in [30].
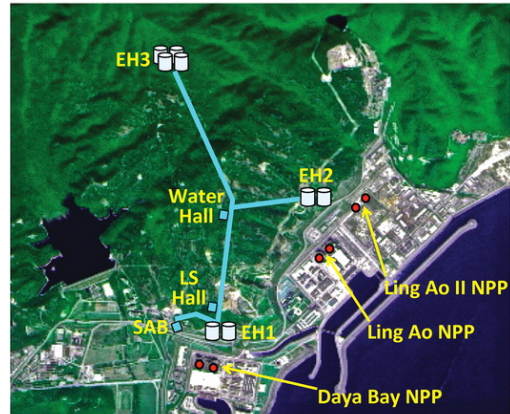

FIG. 1. Layout of the Daya Bay experiment. The Daya Bay and Ling Ao nuclear power plant (NPP) reactors (red circles) were situated on a narrow coastal shelf between the Daya Bay coastline and inland mountains. Two antineutrino detectors installed in each underground experimental hall near to the reactors (EH1 and EH2) measured the $\overline{\nu}_e$ flux emitted by the reactors, while four detectors in the far experimental hall (EH3) measured a deficit in the $\overline{\nu}_e$ flux due to oscillation. The detectors were built and initially tested in a surface assembly building (SAB), transported to a liquid scintillator hall (LS Hall) for filling, and then installed in an experimental hall.

The reactors at Daya Bay were arranged in two clusters: the Daya Bay cluster hosted two reactors (D1 and D2),

TABLE I. The surveyed coordinates of the geometric centers of the nuclear reactor cores and antineutrino detectors of the Daya Bay experiment. The detectors are labeled as AD1 through AD8, according to their order of assembly and installation. The X coordinate is due north, while the Z coordinate is vertical at the survey origin. Coordinates were determined from a combination of total station electronic theodolite and GPS measurements, with a precision of 18 mm. The corresponding neutrino oscillation baselines for each reactor-detector pair are provided. The approximate rock overburden of each experimental hall and the mass of the GdLS antineutrino target in each detector are also given in both meters and meters-water-equivalent. The average thermal power of each reactor core, in gigawatts, is given separately for the six detector and eight detector periods.

							Reactor					
							D1	D2	L1	L2	L3	L4
						$\overline{W}_{\mathrm{th}}^{6\mathrm{AD}}$	2.082	2.874	2.516	2.554	2.825	1.976
						$\overline{W}_{\mathrm{th}}^{8\mathrm{AD}}$	2.514	2.447	2.566	2.519	2.519	2.550
						X [m]	359.20	448.00	-319.67	-267.06	-543.28	-490.69
						Y [m]	411.49	411.00	-540.75	-469.21	-954.70	-883.15
						Z [m]	-40.23	-40.24	-39.73	-39.72	-39.80	-39.79
Hall	Depth [m(mwe)]	Detector	Target [kg]	X [m]	Y [m]	Z [m]	Baseline [m]					
EH1	93	AD1	19941 ± 3	362.83	50.42	-70.82	362.38	371.76	903.47	817.16	1353.62	1265.32
	(250)	AD2	19967 ± 3	358.80	54.86	-70.81	357.94	368.41	903.35	816.90	1354.23	1265.89
EH2	100	AD3	19891 ± 4	7.65	-873.49	-67.52	1332.48	1358.15	467.57	489.58	557.58	499.21
	(265)	AD8	19944 ± 5	9.60	-879.15	-67.52	1337.43	1362.88	472.97	495.35	558.71	501.07
		AD4	19917 ± 4	936.75	-1419.01	-66.49	1919.63	1894.34	1533.18	1533.63	1551.38	1524.94
EH3	324	AD5	19989 ± 3	941.45	-1415.31	-66.50	1917.52	1891.98	1534.92	1535.03	1554.77	1528.05
	(860)	AD6	19892 ± 3	940.46	-1423.74	-66.50	1925.26	1899.86	1538.93	1539.47	1556.34	1530.08
		AD7	19931 ± 3	945.17	-1420.03	-66.49	1923.15	1897.51	1540.67	1540.87	1559.72	1533.18

while the Ling Ao cluster hosted four (L1, L2, L3 and L4). Correspondingly, four near detectors were divided between two near experimental halls (EH1 and EH2) near the two clusters. The remaining four detectors were installed in a single far hall (EH3). The locations of the experimental halls were determined to optimize sensitivity to θ_{13}, considering reactor locations and mountain topography. While uncertainties in reactor flux were not completely canceled as would happen for the case of a single reactor, this arrangement of detectors reduced the far-to-near flux ratio uncertainty to $\leq 0.1\%$ (see Sec. V). The layout of the six reactors and three experimental halls is shown in Fig. 1.

When comparing the measurements between near and far detectors, the largest relative correction was from the baselines of the detectors, as seen in Eq. 4. Accurate surveys of the experiment site allowed precise correction for this effect. Surveys consisted of total station electronic theodolite measurements combined with supplemental global positioning system (GPS) measurements. Lacking GPS reception underground, surveys of the experimental halls and access tunnels relied on redundant total station measurements. Table I provides the surveyed reactor and detector coordinates, where X is due north and Z is vertical at the survey origin. Uncertainties in the survey results were 18 mm in each coordinate, dominated by the precision of the GPS measurements and the tension between GPS and total station survey results. $\overline{\nu}_e$ emission was distributed throughout the fuel elements of each reactor core, spanning a region 3.7 m in height and 3 m in diameter. Reactor models established the horizontal centroid of $\overline{\nu}_e$ emission to within 2 cm of the geometric center of each core. With the centroid determined, the spatial variation of the distribution of $\overline{\nu}_e$ emission within the core had negligible impact to the oscillation measurement.

The combination of organic liquid scintillator with photo-multiplier tubes (PMTs) results in a powerful technique for reactor $\overline{\nu}_e$ detection. Scintillator contains protons (as ^{1}H) which serve as targets for $\overline{\nu}_e$ inverse beta decay interactions (see Eq. 1). Scintillators simultaneously function as a sensitive medium, emitting photons in response to ionization by the products of IBD interactions. Detection of the photons using PMTs allows a calorimetric measurement of the prompt positron energy deposition. This energy is the sum of the IBD positron kinetic plus annihilation energy, $E_{\mathrm{prompt}} = T_{e^+} + 2m_e$, where m_e is the mass of the electron. The initial $\overline{\nu}_e$ energy can be accurately estimated using $E_\nu \simeq E_{\mathrm{prompt}} + 0.8$ MeV, based on the kinematics of inverse beta decay. The IBD neutron generally carries only a small fraction of the initial kinetic energy, O(10 keV). The neutron thermalizes and is then captured on a nucleus within the scintillator in a time of O(100 μs). The resulting nucleus rapidly de-excites by emitting one or more characteristic γ-rays. Detection of this subsequent pulse of scintillation light from the delayed neutron capture γ-rays efficiently discriminates $\overline{\nu}_e$ interactions from background.

The eight antineutrino detectors of the Daya Bay experiment relied on this technique, and were designed to specifically limit potential variations in response and efficiency between detectors. Each detector consisted of a nested three-zone structure, as shown in Fig. 2. The central $\overline{\nu}_e$ target was 20-tons of linear-alkyl-benzene-based liquid scintillator, loaded with 0.1% of $^{\mathrm{nat}}$Gd by mass (GdLS). Details of the production and composition of the scintillator are discussed in [31]. Gadolinium (Gd) efficiently captures thermalized neutrons, emitting a few γ-rays with a total energy of $\sim$8 MeV per capture. The relatively high capture energy enhanced discrimination of the signal from

backgrounds produced by natural radioactivity, primarily at energies $\lesssim 5$ MeV. Gd-loading also provided a physical method to fiducialize the detector, allowing efficient rejection of $\overline{\nu}_e$ interactions which occurred outside the target volume. The target scintillator was contained within a 3 m by 3 m cylindrical tank, referred to as the Inner Acrylic Vessel (IAV), which was made of UV-transparent acrylic. This was nested within a similar 4 m by 4 m acrylic tank, refered to as the Outer Acrylic Vessel (OAV), which was filled with scintillator without Gd-loading (LS). This outer scintillating region significantly increased the efficiency for detection of gamma rays produced in the target region, reducing systematic uncertainties from effects at the target boundary. Hence, this region was referred to as the gamma catcher. Both regions were nested within a 5 m by 5 m stainless steel vessel (SSV), which was filled with mineral oil (MO). The MO had a density matching that of the LS and GdLS, which balanced stresses across the thin-walled ($\sim$1.5 cm) acrylic vessels. It also shielded the scintillating regions from gamma rays from radioactivity in the SSV and PMTs, and provided a transparent medium for propagation of scintillation light to the PMTs.
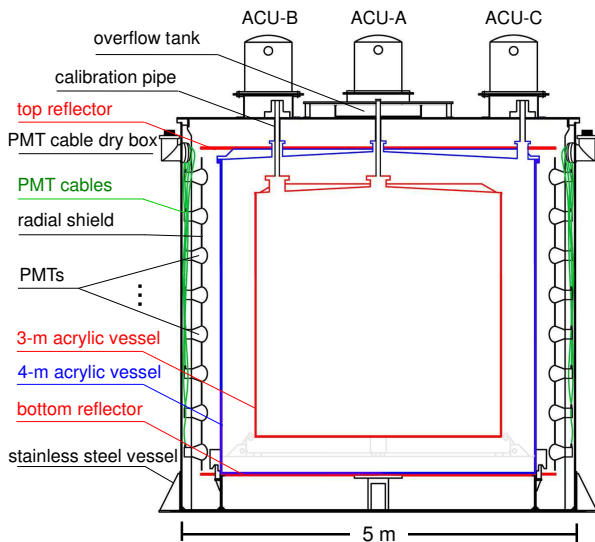

FIG. 2. Cross-sectional diagram of an antineutrino detector (AD). Scintillation light was produced when a reactor $\overline{\nu}_e$ interacted within the central 20-ton GdLS target, which was contained in a transparent acrylic vessel. The target was nested within an additional 20-tons of pure LS to increase efficiency for detection of gamma rays produced within the target. Scintillation light was detected by 192 photomultipliers mounted on the inner circumference of a 5 m by 5 m stainless steel vessel, which was filled with mineral oil (MO).

Scintillation light was detected using 192 8-inch PMTs (Hamamatsu R5912) which were immersed in the MO, and mounted in 8 rings of 24 on the inner cylindrical surface of each SSV. Specular reflectors located above and below the OAV improved the uniformity of light collection versus position within the scintillating regions. In the radial direction, a black light-absorbing radial shield masked all but the photocathode of the PMTs, simplifying and unifying the optical characteristics of the eight detectors. Liquid overflow

tanks on the top of the detector allowed for small changes in liquid volume of each region in response to changes of temperature and pressure. Three automated calibration units (ACUs) were used to deploy radioactive sources (^{60}Co, ^{68}Ge, and ^{241}Am-^{13}C) and light-emitting diodes (LEDs) through narrow teflon-bellow penetrations into the GdLS and LS regions. Details of the calibration system are provided in [32].

Small differences ($<$0.5%) in the total number of protons within each AD target region was the next most significant correction when comparing the measurements of the far versus near detectors (i.e. N_p in Eq. 4). After mechanical assembly and testing within a surface assembly building (SAB), each dry AD was transported to an underground liquid scintillator hall for filling. All GdLS was produced in advance and divided equally between the eight ADs in order to ensure a consistent proton and Gd density, as well as optical performance. Each AD target was filled with GdLS from a reservoir mounted on precision weigh-bridge load cells, whose performance was confirmed using calibrated test masses. Drift in the load cell readings over several days provided the dominant systematic uncertainty of ± 2 kg. An independent measurement used a coriolis flow meter to confirm the relative differences in mass delivered to each AD with few-kg precision, although this instrument measured the absolute mass with far less precision than the load cells. A 0.13% correction accounted for the weight of nitrogen gas which displaced the GdLS within the reservoir during filling. After filling, another correction was made for the small fraction of GdLS present within the calibration tubes and overflow tank, and hence outside of the IAV target volume. Table I summarizes the measured GdLS mass within each IAV target. The 5-kg precision of the target mass correction corresponded to a negligible 0.03% systematic uncertainty in the comparison of antineutrino interaction rates among the ADs.

After filling, the antineutrino detectors were installed in a 10 m deep water pool in each underground experimental hall, as shown in Fig. 3. The water shielded the detectors from γ-rays arising from natural radioactivity and muon-induced neutrons, which were primarily emanating from the cavern rock walls. The pool was optically separated into two independent regions, the inner (IWS) and outer water shield (OWS). Both regions were instrumented with PMTs to detect the Cherenkov light produced by muons. A 4-layer modular resistive plate chamber (RPC) system was installed over the pool, which served in studies of muons and muon-induced backgrounds. Identification of muons which passed through the IWS, OWS, and RPC system enhanced the rejection of background from neutrons generated by muon interactions in the immediate vicinity of the antineutrino detectors. A detailed description of the muon system was given in [33] and muon-induced backgrounds are discussed in Sec. IV.

A single coaxial cable delivered positive high-voltage to, and returned the signal from, each PMT. A passive circuit AC-decoupled the fast PMT signal from the HV, and the signal was input to a channel of the front-end electronics (FEE). The HV for each PMT was tuned for detecting single photoelectrons (PE), with gains matched at $\sim 1.0 \times 10^7$ to
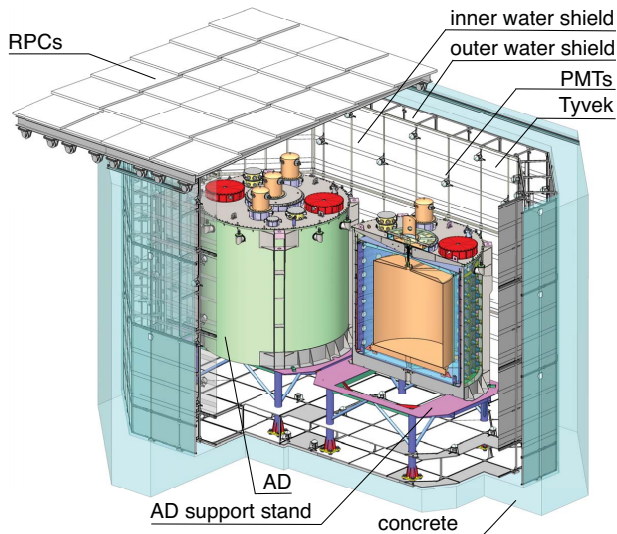
FIG. 3. Diagram of a near site detector system. Two ADs were immersed in a water Cherenkov muon detector which functioned as both a passive radiation shield and an active muon tag. Tyvek sheets divided the pool into two optically separate detectors, the inner and outer water shields. An RPC system covered the pool, providing additional muon identification.

within 5%. After an initial fast amplification, the FEE split the signal for separate measurements of the charge and relative arrival time. One copy of the signal was passed to a discriminator with a threshold of ∼0.25 pe, which served as the start signal for a TDC with 1.6 ns resolution. The other copy was sent to a CR-(RC)^4 pulse shaping circuit which provided an integral measure of the incoming signal charge with a ∼100 ns time constant [34]. The signal was ×10 amplified and then sampled by a 40 MHz 12-bit ADC, which provided better than 0.1 pe resolution. To increase the dynamic charge range for processing very large signals, an additional copy of the shaper output was passed to a ×0.5 amplifier and sampled by an equivalent ADC. The peak sample value obtained by each ADC, as well as a measure of each ADC pedestal preceding the signal, was buffered and awaited triggering of the detector.

Each detector (ADs, IWS, OWS) operated as an independently triggered system using a Local Trigger Board (LTB). Each FEE board accepted signals from up to 16 PMTs, and transmitted a count of the number of channels over threshold, as well as an analog sum of all signals, to the LTB. A trigger was issued for each detector under the following conditions:

- AD: The total count of channels over threshold (NHIT) was ≥45 or analog sum (ESUM) was ≥65 PE (∼0.4 MeV).

- IWS: The NHIT was ≥6 for an IWS.

- OWS: The NHIT was ≥7 for a near-hall OWS, or ≥8 for the far-hall OWS.

- RPC: 3 of 4 layers of a module were above threshold.

- Random: Randomly issued at a rate of ∼10 Hz in order to monitor the level of sub-threshold or accidental activity in each detector.

- Calibration: Simultaneous with each pulse of light emitted from a light-emitting diode (LED).

- Cross-detector: A Master Trigger Board (MTB) at each site could forward triggers from one detector to another. An intended use was to capture activity within the muon systems when an AD detected a potential reactor $\bar{\nu}_e$ (e.g. two AD triggers separated by ≤200 μs).

When a detector received a trigger, it served as a stop signal for the TDCs. The TDC, peak ADC, and pedestal ADC values for each channel over threshold within the past 1.2 μs were then recorded. A digital hit map was recorded for each RPC module which satisfied the 3 of 4 layer trigger threshold. A GPS-synchronized time stamp (25 ns resolution) provided a measure of the absolute time for each triggered event.

The analysis presented here relied on the combination of data from two periods of operation. Extending from Dec. 24, 2011, to Jul. 28, 2012, the first period consisted of 217 days of operation with the first 6 ADs: 2 in EH1, 1 in EH2, and 3 in EH3. The final two ADs, AD7 and AD8, were completed and installed in EH3 and EH2 respectively during the Summer of 2012. An additional 1013 days of data were collected from Oct. 19, 2012, to Jul. 28, 2015. For these two periods, 189 days (87%) and 920 days (91%) of livetime were accepted for the oscillation analysis, with the majority of the downtime attributed to weekly detector calibration.

III. DETECTOR CALIBRATION

As a first step in the analysis, the recorded digital information was converted to time and charge. From the converted values we established the energy scale, and studied the temporal and spatial response of the detectors to particle interactions. The details of the calibration process are discussed in this section. Descriptions of the calibration systems are given in [32] and [33].

A. Time Calibration

As discussed in the previous section, the time at which each detector triggered was recorded with 25 ns precision. Calibration LEDs were used to measure the relative time responses of the PMTs within a single detector. The time delays observed in each channel were corrected for LED-to-PMT distances and were fitted as a function of light intensity. The results were recorded to a database and used to correct TDC values during data analysis. The timing calibration was repeated whenever a modification was made to a detector system (e.g. replacement of FEE, LTB, or MTB board).

B. Energy Calibration

The most critical calibration task was to reduce potential differences in reactor $\overline{\nu}_e$ detection efficiency between ADs, as shown in Eq. 4. Therefore, a calibration process was implemented to reduce detector-to-detector variations in the energy estimated for equivalent particle interactions. At the lowest level, the uncalibrated charge from each PMT i was determined from the difference between the ADC peak value and the ADC pedestal value reported by the FEE, $Q_i = ADC_i^{\text{peak}} - ADC_i^{\text{ped}}$. Each AD was principally a calorimetric detector, hence the estimate of the total energy deposited by a particle interaction, E_{rec}, was proportional to a calibrated sum of the charges measured by each PMT, Q_i. This sum can be expressed as

$$E_{\text{rec}} = \left(\sum_i \frac{Q_i}{\overline{Q}_i^{\text{SPE}}(t)} \right) \frac{f_{\text{act}}(t)}{N^{\text{PE}}(t)} f_{\text{pos}}(\mathbf{r}_{\text{rec}}, t), \quad (5)$$

including the following calibration terms:

- PMT charge scale, $\overline{Q}_i^{\text{SPE}}(t)$: a scale conversion from charge to detected light unique for each PMT plus electronics channel, roughly 19 ADC counts per single photoelectron (SPE).

- Active PMT correction, $f_{\text{act}}(t)$: a unitless factor which compensated for the reduced light collected when a PMT channel was temporarily disabled. The factor is defined as the ratio of total to active AD PMTs, and amounts to a minor correction of $(1/192) \simeq 0.5\%$ per inactive PMT in an AD.

- Light yield, $N^{\text{PE}}(t)$: a scale conversion from total AD detected light to mean particle interaction energy, approximately 170 photoelectrons per MeV of deposited energy.

- AD nonuniformity correction, $f_{\text{pos}}(\mathbf{r}_{\text{rec}}, t)$: a unitless factor which compensated for the observed variation in collected light versus the estimated position $\mathbf{r}_{\text{rec}}$ of a particle interaction in the AD. The correction was $\pm 5\%$ within the target region, and from -6% to +15% including interactions in the gamma catcher.

The following sections discuss how these calibration factors were determined and validated.

1. PMT Charge Calibration

The first step in the energy scale calibration chain consisted of correcting for the few-percent differences that exist in the gain of each PMT and the associated electronics versus time, $\overline{Q}^{\text{SPE}}(t)$. The operating voltages necessary to achieve a common gain of 1×10^7, $\pm 5\%$, were determined for each PMT prior to installation. Each electronics channel introduced an additional 3% variation in gain. Since the response of each channel drifts with changing environmental conditions

as well as with hardware replacements, a calibration method that operated concurrently with regular antineutrino data collection was developed. In this method, the gain was determined using individual PMT signals uncorrelated with particle interactions within the scintillator. These signals were primarily single photoelectrons from thermal emission, also referred to as PMT dark noise, and were captured by the data acquisition system in the few hundred nanoseconds prior to a particle interaction which triggered a detector. The baseline subtracted charge distributions of these uncorrelated signals for each channel were used to estimate the SPE gain versus time. The gain was re-estimated every ~ 6 hours, as this was the minimum time required to collect sufficient uncorrelated signals from each PMT channel.

The probability distribution of charge signals Q from a PMT was modeled using the convolution of a Poisson distribution with a Gaussian function [35],

$$S(Q) = \sum_n^\infty \frac{\mu^n e^{-\mu}}{n!} \frac{1}{\sigma_{\text{SPE}}\sqrt{2n\pi}} \exp\left(-\frac{(Q - n\overline{Q}^{\text{SPE}})^2}{2n\sigma_{\text{SPE}}^2} \right), \quad (6)$$

where μ is the mean number of photoelectrons (PEs) collected by the first dynode, and $\overline{Q}^{\text{SPE}}$ and σ_{SPE} are the mean charge and resolution of the SPE distribution in units of ADC counts. The values of these three parameters which best described the observed distribution S were determined for each PMT. Signals from PMT dark noise were predominantly single photoelectrons, hence the sum was limited to $n \leq 2$ without loss of precision. Noise resulted in fluctuations of the distributions below 10 ADC counts, and the results were more stable when this region was not used to constrain the model. Fig. 4 shows an example SPE charge distribution and corresponding model.
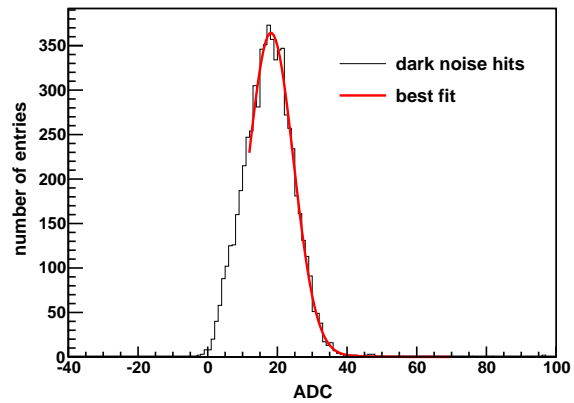

FIG. 4. Example of the baseline-subtracted ADC charge distribution of uncorrelated PMT signals modeled using Eq. 6.

This procedure was applied to each PMT channel, and Fig. 5 shows the mean charge per SPE averaged over all channels within each AD as a function of time. The typical gain calibration constant was on the order of 19 ADC counts per SPE, although several-percent differences existed in the average gain between ADs. A slight upwards drift in gain

was observed for all detectors. This drift was partially but not completely attributable to changes in temperature of the front-end electronics. Jumps correlated among the ADs within the same hall were correlated with power-cycling of the PMT high voltage mainframes. An independent method of determining PMT channel gains, based on weekly low-intensity calibration LED data samples, reproduced all of these observed features.
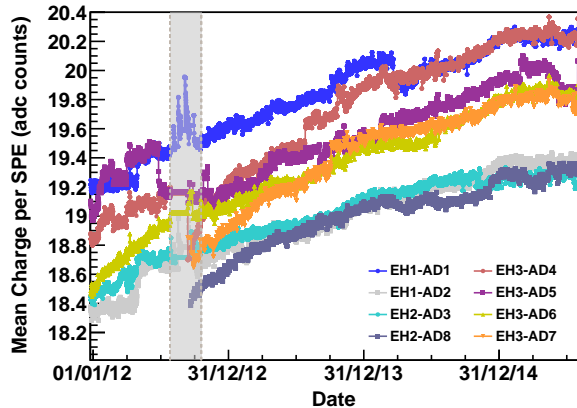

FIG. 5. Average number of ADC counts per single photoelectron, averaged over all PMT channels within each AD versus time. The shaded vertical band delineates the Summer 2012 shutdown period, during which the high-voltage mainframes were frequently power-cycled and data-taking was partially interrupted for installation activities.

2. Active PMT Correction

An extensive data monitoring process was implemented in order to ensure all data were of high quality. In this process, suspect PMT channels were temporarily removed from the analysis due to poor gain, high noise, or other features, as identified by an automated algorithm run concurrently with data collection. The most common cause for disabling a PMT channel was temporary instability in the supplied high voltage. The total number of disabled channels at any one time typically fluctuated around five, combined across all eight detectors, with rarely more than one in a given detector. The absence of a single channel biased the total number of detected photoelectrons within an AD by an average of $1/192 \simeq 0.5\%$. Adjusting the observed number of photoelectrons using the simple factor $f_{\mathrm{act}}(t) = N_{\mathrm{total}}/N_{\mathrm{active}}(t)$, where N_{active} is the number of active PMT channels and $N_{\mathrm{total}} = 192$, was found to sufficiently compensate for this bias.

3. Light Yield Determination

For a particle interaction of fixed energy, the mean number of detected photoelectrons slightly varied between detectors,

as well as versus time within a single detector. The mean number of observed PEs per MeV, $N^{\mathrm{PE}}(t)$, was estimated with two independent and complementary methods: (i) weekly ^{60}Co deployments at the detector center (calibration A), and (ii) uniformly distributed spallation neutrons concurrent with antineutrino data collection (calibration B).

The light yield was determined from the mean of a known gamma-ray peak in the corresponding energy spectrum, either 2.506 MeV for ^{60}Co or the dual peaks of 7.95 MeV and 8.54 MeV for neutron capture on Gd. Escape of gamma-rays from the scintillator regions introduced a low-energy tail, which was modeled using a Crystal Ball function for each peak [36]. The resulting energy scale constants obtained with both ^{60}Co and spallation neutrons can be seen in Fig. 6. The observed light yield varied slightly with the particle
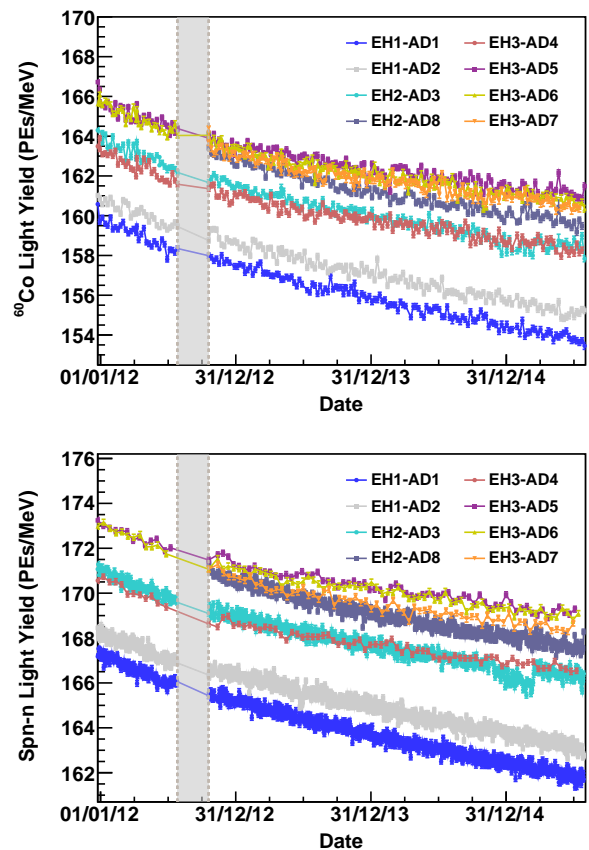

FIG. 6. *Top*: Observed light yield versus time, in units of observed photoelectrons (PEs) per MeV, as obtained using weekly deployments of a ^{60}Co source at the center of each detector. *Bottom*: Observed light yield obtained using spallation neutron capture on Gd distributed throughout the target volume. A consistent $\sim 1\%$ per year decline in the light yield was observed for all detectors. The offset in light yield between these two calibration references was due to the nonlinear response of the detectors. The vertical shaded band indicates the summer 2012 shutdown period, during which data-taking was partially interrupted for installation of the final two detectors.

energy and type, primarily due to the intrinsic nonlinear light emission of the scintillator (see Sec. III D). Given that this

variation was very similar for all detectors, it was sufficient to choose the light yield at the 7.95 MeV peak of n-Gd capture as a common convention. Therefore the light yields obtained using the ^{60}Co source were scaled using the ratio of light yield relative to that from n-Gd capture observed with an ^{241}Am-^{13}C neutron source deployed weekly at the detector centers. A clear drift downwards of about 1% to 1.5% per year was seen in the energy scale with both methods, the origin of which has not yet been conclusively identified. The drift was slightly more pronounced when measured with the ^{60}Co source at the center compared to the uniformly distributed spallation neutrons, which suggested that the effect was related to a slight degradation of light transmission in the liquid scintillator. The drift resulted in a second-order time-dependent spatial nonuniformity and a negligible degradation in energy resolution, neither of which had a significant impact on the neutrino oscillation analysis discussed here. Likewise, it is not expected to compromise the operation of the detectors in the near future.

4. Spatial Nonuniformity

The observed light yield varied with the position of a particle interaction within a detector. This spatial nonuniformity was attributed to the optical characteristics of the detector, primarily from the geometric acceptance of the PMTs. It was similar for all detectors, and was reproduced using Monte-Carlo simulation. Correcting for this effect improved the energy resolution of each detector, and improved the similarity of response among the detectors.

In order to correct for the spatial nonuniformity, a method for determining the position of each particle interaction was needed. Two independent reconstruction methods were developed. Reconstruction A calculated a center-of-charge (COC) for each signal,

$$\mathbf{r}_{\mathrm{COC}} = \left(\sum_i \mathbf{r}_i \frac{Q_i}{\overline{Q_i^{\mathrm{SPE}}}(t)} \right) \Big/ \left(\sum_i \frac{Q_i}{\overline{Q_i^{\mathrm{SPE}}}(t)} \right), \quad (7)$$

where r_i is the position of the i'th PMT. The observed $\mathbf{r}_{\mathrm{COC}}$ was converted to the estimated reconstructed position $\mathbf{r}_{\mathrm{rec}}$ in cylindrical coordinates according to the relations

$$r_{\mathrm{rec}} = c_1 \times r_{\mathrm{COC}} - c_2 \times r_{\mathrm{COC}}^2,$$
$$z_{\mathrm{rec}} = (z_{\mathrm{COC}} - c_3 \times z_{\mathrm{COC}}^3) \times (c_4 - c_5 \times r_{\mathrm{COC}}),$$
$$\phi_{\mathrm{rec}} = \phi_{\mathrm{COC}}. \quad (8)$$

In this cylindrical coordinate system, the origin is the center of the AD target region, z gives the vertical distance from the origin, while r and ϕ define the position in the horizontal plane of the detector. A simulation, based on Geant4 [37], motivated the functional form of this model with the five parameters c_i. The values of c_i were determined from data obtained by deploying ^{60}Co sources at known positions within the detectors. The alternate method, reconstruction B, compared the distribution of charge observed by the 192 PMTs with a
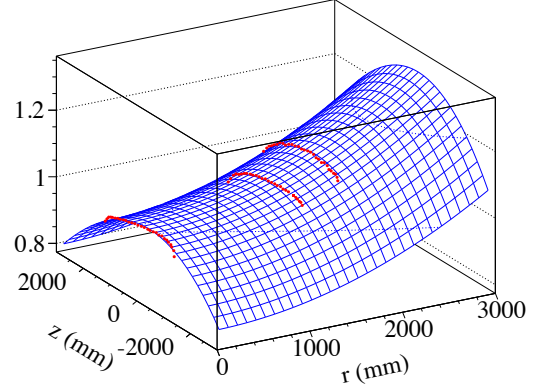

FIG. 7. Variation in light yield versus vertical (z) and radial (r) position of an interaction within EH1-AD1 for reconstruction A (blue surface). The functional form of the variation $f_{\mathrm{b}}(z,r)$ was motivated by simulation, and constrained using the relative light yield of ^{60}Co calibration data from ACU A (r=0 mm), ACU B (r=1350 mm) and ACU C (r=1772.5 mm) (red points). While the modeled correction was between -6% to 17% over the volume of a detector, only slight differences (<3.2%) were observed between the eight detectors.

library obtained from simulation. A library of 9600 charge-pattern templates was constructed by simulating interactions in the detector on a grid with 20 bins in the r direction, 20 in the z direction, and 24 in the ϕ direction. The observed charge pattern was compared to a template using

$$\chi^2 = \sum_i \left(-2 \ln \frac{P(N_i^{\mathrm{obs}}; N_i^{\mathrm{temp}}(\mathbf{r}_{\mathrm{rec}}))}{P(N_i^{\mathrm{obs}}; N_i^{\mathrm{obs}})} \right), \quad (9)$$

where $P(n, \mu)$ is the Poisson probability of finding n photoelectrons when the mean value is μ, N_i^{obs} is the observed number of photoelectrons in the i-th PMT, and $N_i^{\mathrm{temp}}(r, z, \phi)$ is the expected number of photoelectrons in the i-th PMT as predicted by the template. The χ^2 function was interpolated for $\mathbf{r}_{\mathrm{rec}}$ located between simulated templates. The reconstructed position was determined as the $\mathbf{r}_{\mathrm{rec}}$ that gave the minimum value of χ^2. The performance of both reconstruction methods was studied using calibration data, and was found to be similar. In particular, both methods estimated the position of signals from ^{60}Co sources with < 20 cm of bias and with < 40 cm resolution within the GdLS and LS regions. Both vertex reconstruction methods accounted for bad PMT channels by not including them in the COC calculation (reconstruction A) or by removing them from both the data and templates (reconstruction B)

The reconstructed position was used to correct for the observed variation in light yield versus interaction position in the detector. The correction $f_{\mathrm{pos}}(\mathbf{r}_{\mathrm{rec}}, t)$ was decomposed into azimuthal, z-r, and t-r variations,

$$f_{\mathrm{pos}}(\mathbf{r}_{\mathrm{rec}}, t) = [f_{\mathrm{a}}(\phi) \, f_{\mathrm{b}}(z, r) \, f_{\mathrm{c}}(t, r)]^{-1}. \quad (10)$$

Only the radial component showed a significant variation versus time t. A $\sim 1\%$ dependence of the light yield with
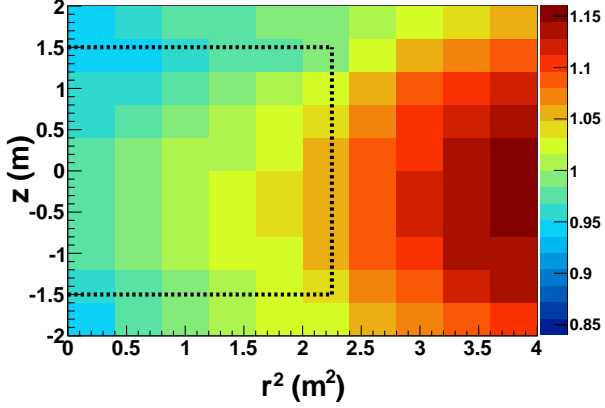
FIG. 8. Variation in light yield versus vertical (z) and radial (r^2) position of neutron capture interactions within EH1-AD1 for reconstruction B. Each pixel shows the ratio of the observed light yield over the average for the entire GdLS region. The dashed lines indicate the boundary between the GdLS and LS regions. Neutrons which captured on Gd were used for the innermost GdLS region, while neutrons captured on hydrogen were used for the outermost LS region. Only slight differences ($<3.0\%$) in the nonuniformity were observed between the eight detectors.

azimuthal angle ϕ was observed in all detectors, and was correlated with the orientation of the PMTs relative to the local geomagnetic field. The effect was modeled as

$$f_a(\phi) = 1 + \alpha^a \sin(\phi - \phi_0), \qquad (11)$$

where the parameters α^a and ϕ_0 were determined from the observed azimuthal variation in the light yield of spallation neutron capture signals. The variation in light yield versus r and z was more significant. For this component, reconstruction A used a parameterization motivated by simulation,

$$f_b(z, r) = \left(\alpha_0^b r^2\right) \times \left(\alpha_1^b + \alpha_2^b z + \alpha_3^b z^2 + \alpha_4^b z^3\right), \quad (12)$$

where the parameters α_i^b were determined using ^{60}Co sources located at known positions within each detector. The variation modeled for EH1-AD1 is shown in Figure 7.

Reconstruction B used signals from spallation neutron capture, divided into 100 pixels in z and r^2, to construct a nonuniformity correction map. For each pixel the ratio of the observed light yield over the average light yield for the entire GdLS region was calculated, as illustrated in Figure 8 for the case of EH1-AD1. The map was estimated using neutrons captured on Gd for the innermost GdLS region, while neutrons captured on H were used for the outermost LS region. The average of the two were used for those pixels spanning the boundary between the GdLS and LS.

Both techniques found consistent nonuniformities. Variations on the order of 10% and 17% were observed in the vertical and horizontal directions respectively across the volume formed by the GdLS and LS regions. Differences in nonuniformity of a few percent were observed for signals at the extremities of the eight detectors, as shown in Figure 9.
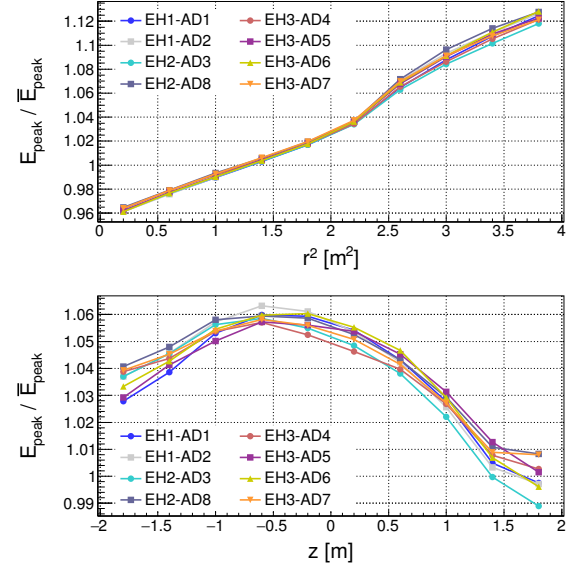

FIG. 9. Comparison of variation in light yield versus radial (*top*) and vertical (*bottom*) position of neutron capture interactions for reconstruction B. Each point shows the ratio of the observed light yield over the average for the entire the GdLS region. The variation was primarily due to the optical acceptance versus position, and was reproduced by optical simulation. Only slight differences ($<3.0\%$) in the nonuniformity were observed between the eight detectors.

The spatial nonuniformity of the light yield showed a slight variation with time. Given that the average drift in light yield over time was accounted for by $N^{PE}(t)$, the time-dependent nonuniformity correction only accounted for time-dependent drifts that differed based on position in the detector. The change of the nonuniformity over time was adequately modeled using

$$f_c(t, r) = \left(\alpha_0^c + \alpha_1^c r^2\right) t. \qquad (13)$$

The parameters α_i^c were determined using data from ^{60}Co sources taken over the first 3 years of operation, while reconstruction B relied on signals from spallation neutron capture on ^{1}H. The time-dependence was sufficiently similar between detectors, so common values for the parameters were used for all eight detectors. The correction was largest for signals near the edge of the LS region, for which a $<0.5\%$ shift in energy response per year was observed.

5. Calibration Performance

a. Energy stability As discussed in the preceding section, the charge calibration, channel quality, AD light yield, and spatial nonuniformity calibration corrections all varied with time. The performance of the full energy calibration process was assessed by examining the stability of the reconstructed energy over time for a variety of calibration reference data. Figure 10 shows the reconstructed mean energy of spallation neutrons captured on H for

the entire period considered in this analysis, for both the ^{60}Co (Calibration A) and spallation neutron (Calibration B) methods. Both methods yielded an energy for n-H capture that was stable to within 0.2%, as determined from the RMS of the distributions in Figure 10.
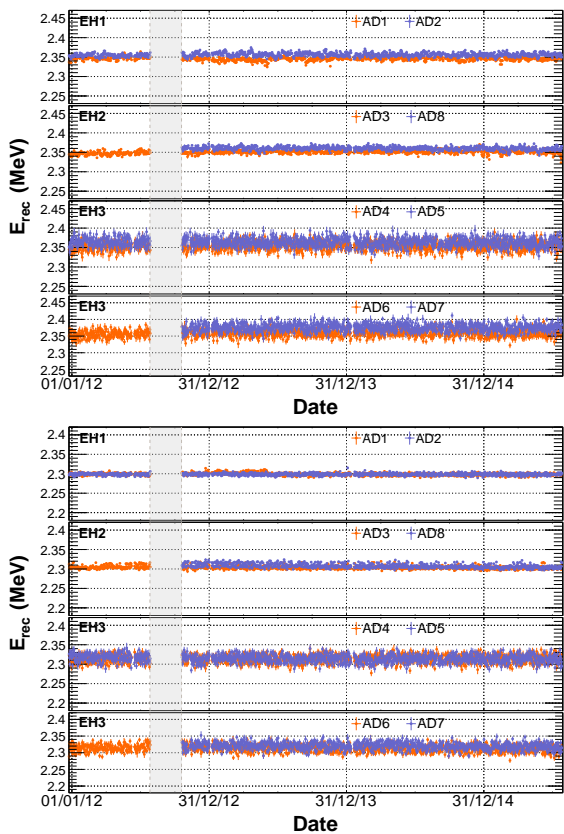

FIG. 10. *Top*: Stability of the mean reconstructed energy of signals from spallation neutron capture on H versus time, obtained from calibration using a ^{60}Co source located at the detector center (reconstruction A). *Bottom*: The same, but for the calibration method which relies on spallation neutrons (reconstruction B). Each point corresponds to one day. The shaded vertical band represents the 2012 shutdown period.

b. AD-to-AD differences Calibration was crucial to ensure that the reconstructed energy for antineutrino interactions within all eight antineutrino detectors was as identical as possible. Small differences in the energy response between detectors could distort the relative efficiency of the far versus near detectors, biasing the measurement of θ_{13} as highlighted by Eq. 4. Slight distortions of the energy response between detectors could also introduce an artificial distortion in the comparison of the antineutrino energy spectra of the near and far detectors, degrading the measurement of Δm^2_{ee}.

AD-to-AD differences were estimated using 13 different calibration references, both deployed and naturally occurring in the ADs. Data from sources deployed on a weekly basis included γ-rays from ^{68}Ge and ^{60}Co, and neutrons from ^{241}Am-^{13}C. Signals generated by natural radioactivity, including α-decays of ^{212}Po, ^{214}Po, ^{215}Po and ^{219}Po and γ-rays from ^{40}K and ^{208}Tl, were also compared

between detectors. Neutrons from IBD and muon spallation that capture on H and Gd provided additional calibration references. These calibration reference data span the full time period used for the oscillation analysis.

The spatial distribution of interactions differed among the calibration references. Some of the sources, e.g. neutron-capture on hydrogen and gammas from external ^{40}K and ^{208}Tl decays, were concentrated at the edge of the scintillating volumes close to the PMTs. Selecting signals with reconstructed positions within the target volume still resulted in distributions dominated by interactions outside the target due to the limited precision of position reconstruction. Rejecting signals within 20 cm of the target boundary gave a distribution sufficiently similar to that of antineutrinos. This tightened selection had negligible impact on the estimated mean energy for α's from ^{212}Po, ^{215}Po and ^{219}Po decays and γ-rays from neutrons capturing on Gd, which were distributed nearly uniformly within the target volume.

Variations in the mean reconstructed energies of these calibration references for all eight ADs are shown in Fig. 11. These calibration references span the range of energies expected for both the prompt and delayed signals from inverse beta decay. Systematic variations were <0.2% with typical deviations around 0.1%, independent of the choice of the calibration and reconstruction methods. Therefore, a conservative 0.2% systematic uncertainty in the potential variation of the relative energy response between detectors was used.

From 2012 until 2014, the levels of the liquids in the MO and LS overflow tanks of EH3-AD4 shifted slowly relative to each other [30]. The changes were consistent with a slow leak of 50 l of LS into the 42,800 l MO region of this detector over this two year period. An increase in the absorbance of short-wavelength light in the MO and an increase in the amount of light detected for muons which traversed the MO verified that a leak had occurred. Despite close examination of the data from this detector, no significant deviation in performance was found. Simulations which accounted for potential light production in the MO supported this conclusion [38]. As will be discussed, the rate of $\overline{\nu}_e$ interactions measured in EH3-AD4 was consistent with the other three detectors in the far hall, which confirmed that the leak did not adversely impact this detector.

C. Energy resolution

The energy resolution of the detectors was modeled using the expression

$$\frac{\sigma_E}{E_{\mathrm{rec}}} = \sqrt{a^2 + \frac{b^2}{E_{\mathrm{rec}}} + \frac{c^2}{E_{\mathrm{rec}}^2}}. \qquad (14)$$

The parameters a, b, and c reflect the contributions to the resolution from detector nonuniformity, photoelectron counting statistics, and noise, respectively. The resolutions observed for calibration sources, neutron captures following inverse beta decay, and natural α radioactivity within the
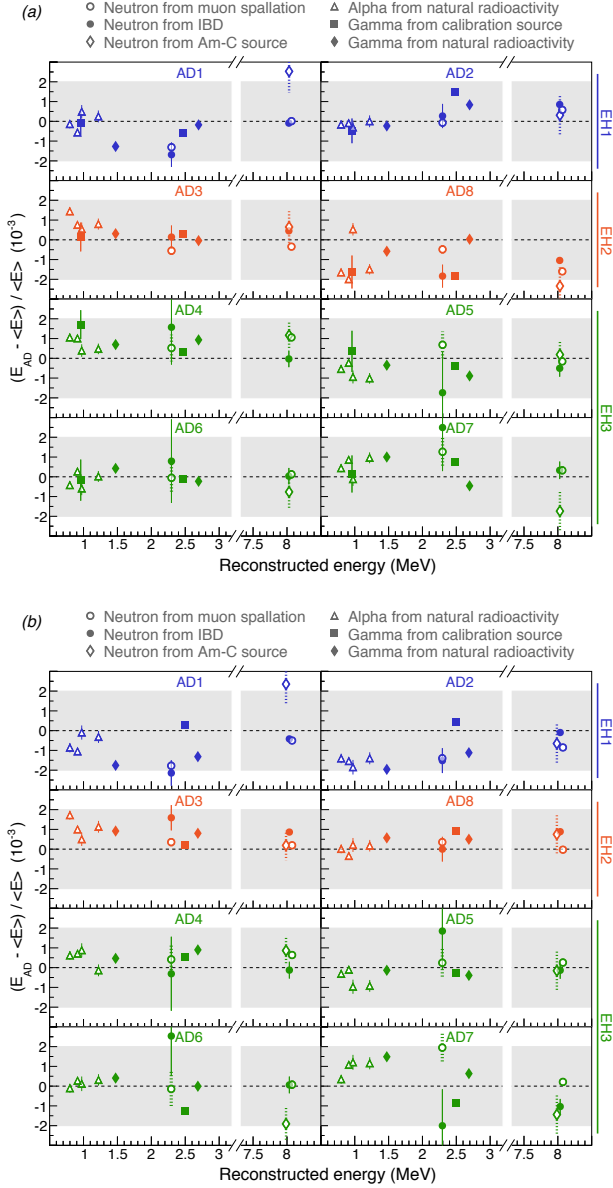
(a)

FIG. 12. Energy resolutions measured for calibration sources, neutron captures following inverse beta decay, and natural α radioactivity within the scintillator (open blue markers). The detector resolution was limited by the statistical uncertainty of photoelectron counting, as modeled using Eq. 14 (blue solid line). The resolutions were consistent with Monte-Carlo simulation (solid orange markers). The simulation predicted that the intrinsic detector resolution (dashed orange line) was slightly better than that estimated for the calibration sources (solid orange line), since the latter suffered from optical shadowing by the source encapsulation. The energy resolutions for α particles emitted by natural radioactivity (open blue triangles) confirmed the intrinsic energy resolution.

(b)

FIG. 11. Comparison of the mean reconstructed energy between antineutrino detectors for a variety of calibration references using (a) calibration with ^{60}Co sources (reconstruction A) and (b) calibration with spallation neutrons (reconstruction B). $E_{\rm AD}$ is the reconstructed energy determined for each AD, while $\langle E \rangle$ is the eight-detector average. The mean energy for each calibration reference was obtained from the corresponding peak in the energy spectrum of all regular data (natural alphas and gammas, neutrons from IBD and muon spallation) and all weekly calibration runs (gammas from ^{68}Ge and ^{60}Co sources, neutrons from Am-C sources) taken during the time period when all eight ADs were in operation. An effective fiducial volume selection has been applied on distributed sources to suppress interactions outside the antineutrino target where AD-to-AD differences are larger. Error bars are statistical only, and systematic variations between detectors for all calibration references were <0.2% for both reconstruction methods.
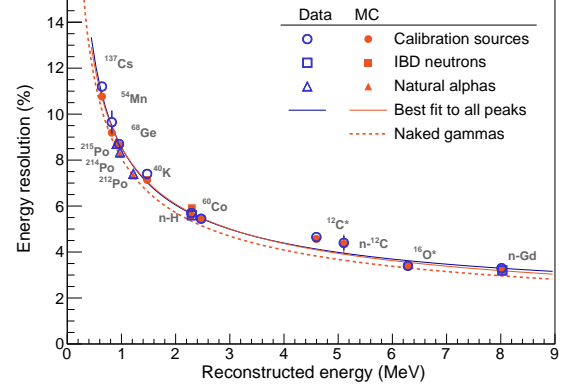
scintillator are shown in Figure 12. Modeling of the detector resolution using Eq. 14 gave $a = 0.016$, $b = 0.081$ MeV$^{1/2}$, and $c = 0.026$ MeV. The total resolution was dominated by photoelectron counting statistics. Simulation predicted that the intrinsic resolution was slightly better than that observed for the calibration sources, since the latter suffered from optical shadowing by the source encapsulation. The intrinsic resolution was confirmed using natural α radioactivity within the scintillator. No significant variations in detector energy resolution were observed among the eight detectors.

D. Absolute Antineutrino Energy

Aside from the relative calibration of the energy response between detectors, it was also necessary to calibrate the detectors in an absolute sense. In particular, interpretation of the distortion in the antineutrino energy spectrum by oscillation required characterization of the relationship between true $\overline{\nu}_e$ energy and the corresponding reconstructed IBD positron energy. While the uncertainty in absolute calibration had negligible impact on the measurement of θ_{13}, it influenced the estimate of the neutrino mass-squared difference. This can be seen as a direct consequence of the ratio of $\Delta m^2_{\rm ee}$ over E_ν in Eq. 3.

To the lowest order, the kinematics of the IBD interaction implied $E_{\rm prompt} \simeq E_\nu - 0.8$ MeV, where the prompt positron energy included 1.022 MeV from annihilation. The angular distribution of neutron recoil introduced a small energy-dependent correction to the above relation, and negligibly

broadened the energy resolution. The most significant bias arose from the nonlinear response of the detector. Nonlinearity of the reconstructed positron energy relative to the true interaction energy originated from two sources: particle-dependent nonlinear light yield of the scintillator, and charge-dependent nonlinearity associated with the electronic readout of the PMT signal. Positron interactions with the scintillator are predominantly identical to electrons, except for their eventual annihilation. Therefore, the visible energy for a positron was effectively modeled as $E_{\mathrm{vis},e^+} = E_{\mathrm{vis},e^-} + 2 \times E_{\mathrm{vis},\gamma}(0.511\,\mathrm{MeV})$.

The scintillation light output for low-energy electrons was suppressed due to ionization quenching. A semi-empirical analytic approach based on Birks' law was used to model this mechanism, expressed as the ratio of the quenched to true electron energy f_q. The energy-dependent contribution from Cherenkov light, predicted to be at the level of a few percent relative to scintillation light, induced an additional nonlinearity. The average Cherenkov light emitted by an electron versus energy, f_c, was extracted from a Geant4-based simulation and confirmed by an independent analytic calculation. A scale factor k_c, defined as the ratio of detected Cherenkov to scintillation photons for 1 MeV electrons, accounted for the difference in the magnitude and detection efficiency between these two components of light. The total detectable light from an electron in the scintillator, here called the *visible* energy E_{vis}, was therefore related to the true kinetic energy E_{true} via

$$\frac{E_{\mathrm{vis}}}{E_{\mathrm{true}}} = \beta_{\mathrm{vis}} \left[f_q(E_{\mathrm{true}}, k_B) + k_c f_c(E_{\mathrm{true}}) \right], \tag{15}$$

where k_B is the Birks' constant for electrons and β_{vis} is an arbitrary normalization.

A Geant4-based simulation was used to model the effective scintillator response to γ-rays as a function of k_B, k_c and the γ-ray energy using this electron model. Monoenergetic γ-rays were tracked in the scintillator until all energy was converted to scattered e^-'s and e^+'s. The E_{vis} for each γ-ray was obtained from the sum of the visible energy for each of these scattered electrons, calculated according to Eq. 15.

The charge nonlinearity induced by the electronics arose from a complex interplay of the time distribution of detected light and the response of the readout electronics, which could not be easily calibrated at the single PMT channel level. Instead, the resulting nonlinearity was modeled at the detector level. A combination of measurements and modeling of the electronics response suggested that the ratio of the reconstructed energy E_{rec} to the visible energy E_{vis} could be effectively parameterized using

$$\frac{E_{\mathrm{rec}}}{E_{\mathrm{vis}}} = \beta_{\mathrm{rec}} \left[1 + \alpha \exp\left(-\frac{E_{\mathrm{vis}}}{\tau} \right) \right], \tag{16}$$

where α determines the amplitude of the nonlinearity, τ sets the energy-dependence, and β_{rec} is an arbitrary normalization.

The complete energy model, relating the reconstructed energy to true particle kinetic energy, therefore contained four free parameters: Birks' constant k_B, the contribution from
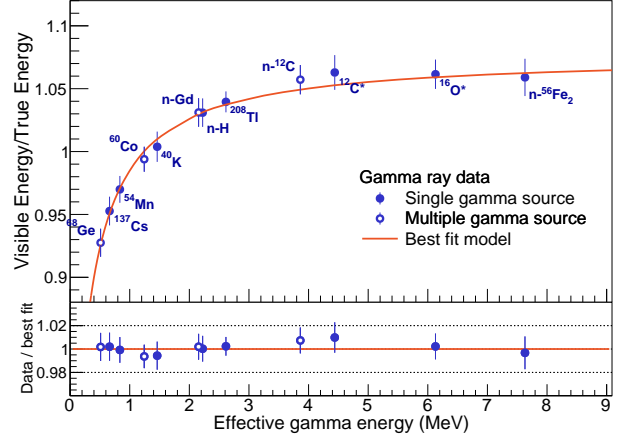

FIG. 13. Ratio of observed energy to true energy for γ-ray reference data relative to the estimated model of the nonlinear scintillation and Cherenkov light emission. For sources which consist of multiple γ-rays, the mean energy is used as an 'effective' energy for the purposes of modeling the scintillator nonlinearity. The best fit for a model of the scintillator nonlinearity is also shown (red solid line). For clarity, the estimated nonlinearity contributed by the electronics has been removed from both the data and the model.

Cherenkov radiation k_c, and the two parameters α and τ of the electronics model. The product of β_{vis} and β_{rec} were defined such that $E_{\mathrm{rec}} = E_{\mathrm{true}}$ at the reference energy of neutron capture on Gd. There was no significant deviation in the nonlinearity between detectors, so a common model was used for all eight ADs. The parameter values were obtained from an unconstrained χ^2 fit to various AD calibration data, consisting of twelve gamma lines from both deployed and naturally-occurring sources, as well as the continuous electron spectrum from the decays of ^{12}B produced by muon interactions with the scintillator. The study accounted for residual position-dependent variations in light yield between the calibration references. Figures 13 and 14 compare the resulting energy response model with the calibration data.

The resulting estimate of the detector response to positrons is shown in Figure 15. The depicted uncertainty band corresponds to variations of model parameters consistent with the fitted calibration data within 68% C.L. The χ^2-based approach was used to constrain the energy response, and resulted in sub-percent uncertainties of the absolute positron energy scale above 2 MeV. The best model gave the values $k_B = 15 \times 10^{-3}\,\mathrm{cm\,MeV^{-1}}$, $k_c = 0.5\%$, $\alpha = 0.078$, and $\tau = 2.55\,\mathrm{MeV}$. Strong correlations among the parameters resulted in large uncertainties for each individually, although the combined model was well-constrained as shown in Figure 15. Reproduction of the model from the best fit parameters was also dependent on the specific configuration of low-energy electron transport and quenching in Geant4. Therefore, the best model is provided in a more convenient tabulated form as Supplemental Material [39].

This model of the detector response to positrons was validated using independent calibration reference data. These
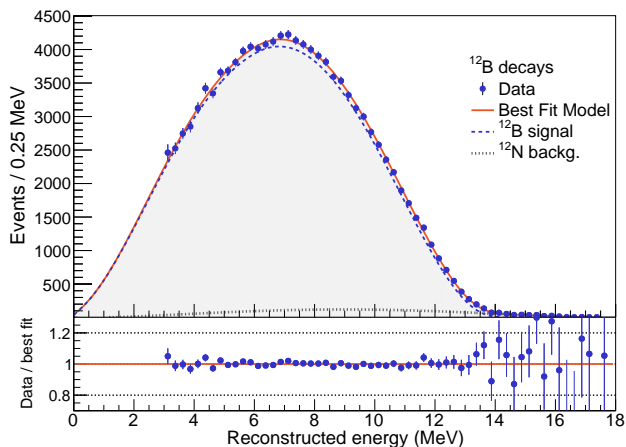
FIG. 14. Comparison of the electron energy spectrum from ^{12}B decay with simulation, including the estimated nonlinearity of the scintillator and electronics.
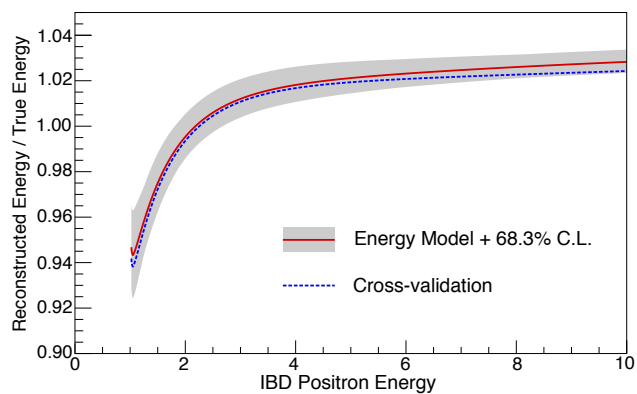

FIG. 15. Estimated ratio of reconstructed over true energy, E_{rec}/E_{true}, for positron interactions totally contained within the antineutrino detector target (red solid line). The two 0.511-MeV γ-rays from positron annihilation were included in the energy. The resulting 68% C.L. region (gray shaded band) constrains this ratio to better than 1% over most of the energy range of interest. An independent estimate, which relied on the $\beta + \gamma$ spectra from bismuth and thallium decay as well as the Michel electron spectrum endpoint, produced a consistent model (blue dotted line).

included the 53 MeV endpoint in the Michel electron spectrum of muon decay, and the continuous $\beta + \gamma$ spectra from natural bismuth and thallium decays. The estimated model of the electronics nonlinearity was corroborated by comparison with PMT data obtained using an independent waveform digitizer system. All measurements have been found to be consistent with the estimated model within their respective uncertainties. In turn, the estimated positron response model was stable within the 1-σ uncertainty band under addition or removal of any single calibration reference data set. As a result of this extensive modeling of the positron energy response, the final $\sim$1% uncertainty is small when compared with the overall uncertainty for Δm^2_{ee} found in the

study presented here.

IV. ANTINEUTRINO SIGNAL AND BACKGROUNDS

The relative far-versus-near measurement of neutrino oscillation, as expressed in Eq. 4, motivated a particular approach to $\overline{\nu}_e$ selection. The selection criteria were not necessarily designed to maximize the $\overline{\nu}_e$ detection efficiency and minimize backgrounds. Instead, the criteria were chosen specifically to minimize relative uncertainties in the comparison of signals observed among the eight detectors. The following section provides a detailed description of the $\overline{\nu}_e$ selection criteria, assessment of the relative efficiencies between detectors, and estimation of the residual backgrounds for the analysis of neutrino oscillation. To briefly summarize, a total of more than 2.5×10^6 $\overline{\nu}_e$ candidate interactions were identified, with potential variation in efficiency between detectors estimated at 0.13%, while background contamination was less than a few percent with an uncertainty of $\lesssim$0.2% in the sample.

Two independent methods and software were developed for selection of the antineutrino candidates. Here we refer to these two approaches as antineutrino selection A and selection B. These methods differed most significantly in their choice of energy calibration and reconstruction: selection A used reconstruction A and selection B used reconstruction B. The two methods also differed slightly in their approach to background rejection. Both methods are discussed here, with their differences highlighted. Table II provides a side-by-side comparison of the two selection methods.

Fig. 16 shows the reconstructed energy spectra of all signals in EH1-AD1 as successive cuts from selection A were applied to the data. This figure provides a brief but helpful introduction to the selection of $\overline{\nu}_e$ signals and rejection of backgrounds. The spectrum for all signals (A) consisted of two prominent components: radioactivity from natural sources below 3 MeV, and muons generated in cosmic ray showers above 3 MeV. A first step in the selection removed a minor instrumentation-related background resulting from light emission by the PMTs, giving (B). A veto following muon signals in the Water Shield efficiently rejected muons and muon-induced neutrons, yielding (C). The muon veto revealed an additional component of natural radioactivity from 3 to 5 MeV (^{208}Tl decay within the scintillator), as well as signals above 5 MeV from the β-decay of unstable isotopes produced by muon-nuclear interactions in the scintillator. From these remaining signals, $\overline{\nu}_e$ inverse beta decay interactions were identified by selecting pairs of signals consistent with a positron, (D-prompt), followed soon after by the capture of a neutron by Gd, (D-delayed). As seen in the figure, the selection of prompt-delayed signal pairs reduced the background by more than five orders of magnitude. A veto following muon signals in the AD suppressed a small residual muon-induced background, and gave the final prompt and delayed energy spectra (E) of the $\overline{\nu}_e$ candidates. Qualitatively similar results were found when the selection was applied to the remaining seven antineutrino detectors. The rest of

TABLE II. Summary of two independent methods used in the selection of reactor $\bar{\nu}_e$ inverse beta decay interactions. See text for details.

Criterion	Selection A	Selection B
Calibration	^{60}Co and ^{241}Am-^{13}C method	Spallation neutron method
Reconstruction	Corrected center-of-charge	Charge template matching
8-inch PMT light emission	Reject $f_{ID} \geq 0$	Reject $f_{ID} \geq 0$ or $f_{PSD} \geq 0$
2-inch PMT light emission	Reject Q_{max}(2-inch PMTs) > 100 p.e.	
Prompt energy	(0.7, 12.0) MeV	
Delayed energy	(6, 12.0) MeV	
Prompt-delayed Δt	(1, 200) μs	
Multiplicity veto (pre)	No signal >0.7 MeV 200 μs before prompt	Only one signal (0.7, 12) MeV 400 μs before delayed
Multiplicity veto (post)	No signal >0.7 MeV 200 μs after delayed	No signal (6, 12) MeV 200 μs after delayed
Water Shield muon veto	Veto (-2, 600) μs after NHIT > 12 in OWS or IWS	
AD muon veto	Veto (0, 1) ms after >20 MeV signal	Veto (0, 1.4) ms after >3,000 p.e. (~18 MeV) signal
AD shower veto	Veto (0, 1) s after >2.5 GeV signal	Veto (0, 0.4) s after >3×10^5 p.e. (~1.8 GeV) signal

this section describes the details of this selection, including assessment of the residual background in the $\bar{\nu}_e$ candidate sample.
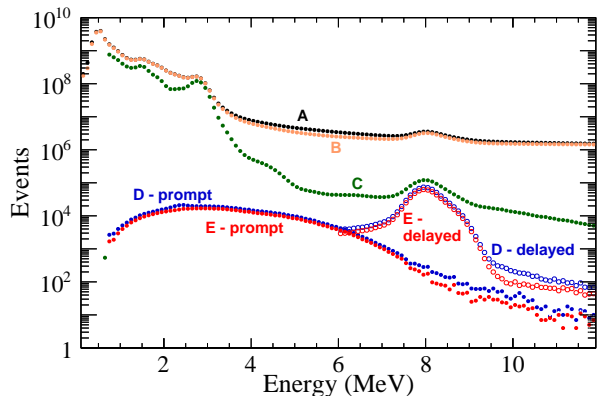

FIG. 16. Reconstructed energy spectra of all signals in EH1-AD1 as successive cuts from selection A were applied: (A) all signals, (B) rejection of signals from PMT light emission, (C) Water Shield muon veto, (D) IBD signal pair selection: prompt energy, delayed energy, prompt-delayed time separation, and multiplicity veto, and (E) AD muon and shower vetos. The spectra E are the final prompt and delayed energy spectra of the $\bar{\nu}_e$ candidates for EH1-AD1.

A. Antineutrino Selection

As discussed in Sec. I, antineutrino inverse beta decay interactions provide a very characteristic pattern of two time-correlated signals of specific energies. The first, or prompt, signal is an e^+ which slows via ionization and then annihilates in the scintillator, generating from 1 to 8 MeV of visible energy. The observed energy can be used to accurately estimate the original energy of the incident $\bar{\nu}_e$. Each IBD interaction also produces a free neutron. Carrying only O(10 keV) of kinetic energy, the neutron thermalizes in ~10 μs via collisions with nuclei in the scintillator. For IBD interactions within the Daya Bay GdLS targets, the

thermalized neutron was subsequently captured by a nucleus with a characteristic time constant of $\tau \simeq 28$ μs. The excited nucleus then relaxed via emission of γ-rays. The interactions of these γ-rays within the scintillator produced the second, or delayed, signal. Within the Gd-loaded target region, ~84% of the captures occurred on either ^{157}Gd or ^{155}Gd. The relative probability for capture on these two Gd isotopes are ~81.5% and ~18.5%, respectively. The total γ-ray energy release per capture is 7.95 MeV for ^{157}Gd and 8.54 MeV for ^{155}Gd. These γ-rays were distinguished from natural radioactive backgrounds, with energies predominantly below 5 MeV.

The remaining ~16% of neutrons captured almost entirely on ^{1}H, releasing a single 2.2-MeV γ-ray. For capture on ^{1}H, it was not possible to clearly discriminate whether the $\bar{\nu}_e$ interacted within the target region or in the gamma-catcher region. Analysis of the n-^{1}H data therefore suffered from larger uncertainties in the target volume and detector response, as well as a much more significant background contamination. Despite these obstacles, independent measurements of neutrino oscillation have been obtained using these interactions [38, 40], with results that were consistent with the analysis of signals identified by n-Gd capture, albeit with less precision.

IBD interactions followed by neutron capture on Gd are the focus of the study presented here. Antineutrino IBD interactions were selected by searching for pairs of interactions separated by 1 to 200 μs, with a reconstructed prompt energy, E_p, between 0.7 and 12 MeV, and a reconstructed delayed energy, E_d, between 6 and 12 MeV. All remaining selection criteria were designed for background rejection, which will be discussed later in this section.

Fig. 17 shows the temporal separation between prompt and delayed signals of the IBD candidates, after applying all selection criteria, of each detector for the entire data period used in this study. Delayed signals with $\Delta t > 200$ μs were rejected since they would not significantly improve signal statistics, yet they would increase background contamination. Signals with $\Delta t < 1$ μs were rejected since they were captured within a single triggered readout of the detector and were therefore not easily discerned as separate interactions. An absolute efficiency of (98.70±0.01)% was estimated by

integrating the temporal distribution from 1 μs to 200 μs, and was confirmed via simulation. Potential variation in the efficiency of the prompt-delayed Δt requirement between detectors was estimated to be 0.01%, by considering potential variation in the Gd concentration and detector timing.
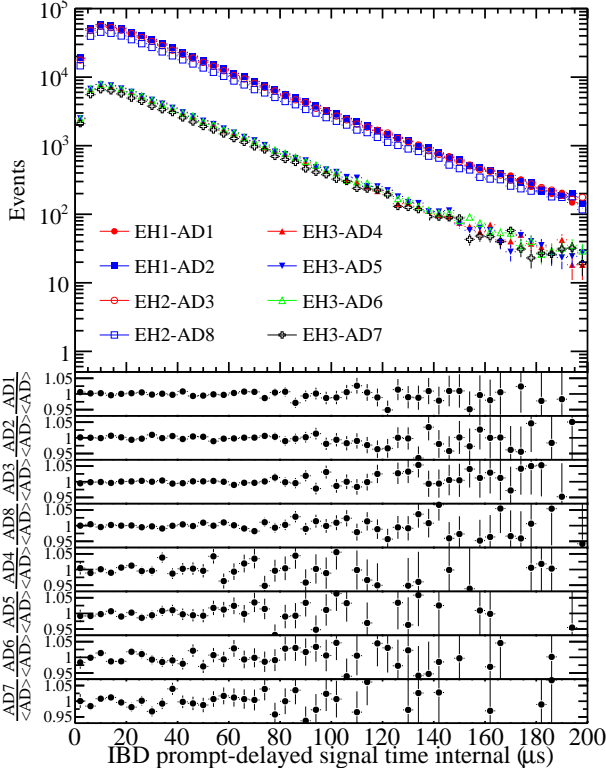

FIG. 17. (*Top*) Distribution of the time separation between prompt and delayed $\overline{\nu}_e$ inverse beta decay interaction candidates for each detector. (*Bottom*) Ratio of the observed distribution to the normalized average for all eight detectors. The consistency of these distributions constrained potential systematic variation in the fraction of IBD neutrons which captured on Gd among the eight detectors.

The fraction of IBD neutrons that were captured on Gd was estimated to be (84.2±0.8)%. This was evaluated using the distributions of neutron capture time for a variety of neutron sources, including muon spallation, ^{241}Am-^{13}C, ^{241}Am-^{9}Be, ^{239}Pu-^{13}C, and IBD interactions, and confirmed by comparison with Monte-Carlo simulation. More importantly, the similarity of the capture time distributions between detectors for each of the neutron sources, as shown in Fig. 18, constrained potential differences in Gd capture fraction to <0.10% [38]. A difference in capture fraction could have resulted from differences in the Gd concentration between the detectors, which was avoided by using a common reservoir of GdLS to fill all eight detectors.

As discussed in Sec. II, each detector was individually triggered when the total number of channels over threshold (NHIT) was ≥45 or the analog sum of all channels (ESUM) was ≥65 PE. This corresponds to a reconstructed energy threshold of ∼0.4 MeV. Comparisons of the measured rates and energy spectra of ^{68}Ge positron annihilation sources
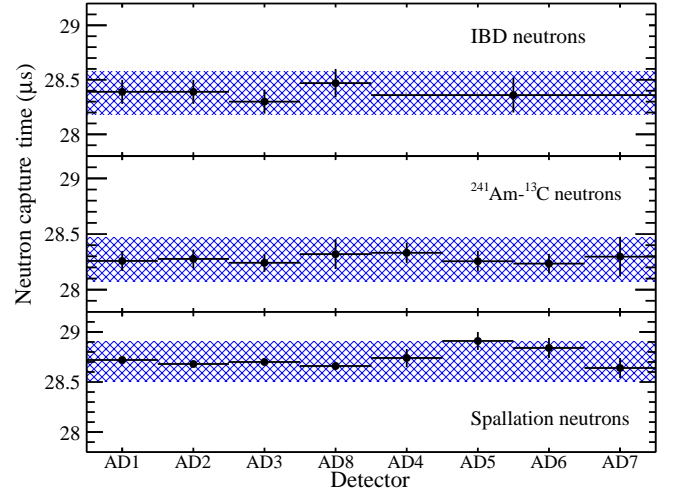

FIG. 18. Comparison of the capture time of neutrons on Gd measured in each detector, for neutrons from IBD, ^{241}Am-^{13}C, and muon spallation. The IBD neutron data is combined for the four detectors in EH3 (AD4–AD7) in order to reduce the statistical uncertainty. The observed capture times vary by less than ±0.2μs between detectors (blue band). The spatial distributions of neutrons emitted by these sources differed, introducing slight offsets in their absolute capture times.

as a function of trigger threshold demonstrated negligible inefficiency in detecting positrons for this trigger threshold (see Fig. 9 of [29]). A combined study of both data and simulation showed that 0.19% of the prompt signals had $E_p < 0.7$ MeV, resulting from finite detector resolution and e^+ energy loss in the IAV acrylic for $\overline{\nu}_e$ interactions close to the target boundary. Variation of the model of the detector response, in particular for positrons which lose energy in the IAV, introduced a 0.10% uncertainty to this selection. Therefore, the absolute efficiency of this selection was estimated to be (99.81±0.10)%. Considering a conservative 2% difference in energy scale at $E_p = 0.7$ MeV, a 0.01% relative uncertainty between detectors was obtained. Models of reactor $\overline{\nu}_e$ emission suggested no detectable signals with $E_p \gtrsim 11$ MeV, which was consistent with the observations presented here. This analysis included signals with E_p up to 12 MeV, introducing no additional inefficiency for reactor $\overline{\nu}_e$ detection.

As shown, the selections based on prompt energy and time difference had very limited potential for introducing differences in efficiency between detectors. This was not the case for the delayed energy selection. In particular, escape of n-Gd γ-rays from the scintillating regions of the detector introduced a low-energy tail to the peak at 8 MeV in the energy spectrum of delayed interactions. The primary purpose of the gamma-catcher region surrounding each antineutrino target was to significantly reduce the magnitude of this spectral tail. According to a Geant4-based simulation, the shape of this tail depended on the γ-ray multiplicity and energy distribution from neutron capture on Gd, which was not accurately known. The observed energy spectra from n-Gd capture of neutrons from muon spallation, ^{241}Am-^{13}C

sources, and IBD interactions were used to constrain potential variations in the simulated n-Gd γ-ray distributions. Based on those simulated γ-ray distributions, an absolute efficiency of $(92.7\pm0.97)\%$ was determined for a selection of $E_{\mathrm{d}} > 6$ MeV. The simulation determined $\sim 6\%$ of the selection inefficiency was from signals with E_{d} between 3.6 MeV and 6 MeV, which was strongly constrained by data. Simulation predicted an additional $\sim 1\%$ inefficiency due to signals with $E_{\mathrm{d}} < 3.6$ MeV, but this estimate was poorly constrained by data due to background from n-^{1}H capture in the observed spectra. Assuming a conservative 100% uncertainty on this part of the distribution resulted in a total uncertainty for the $E_{\mathrm{d}} > 6$ MeV selection of 0.97%. The same studies demonstrated that the selection of $E_{\mathrm{d}} < 12$ MeV was 100% efficient.

Potential variation of the delayed energy selection efficiency between detectors was of greater concern. Three approaches all suggested a similar value for this systematic uncertainty. Direct χ^2 comparisons of the observed n-Gd spectra between detectors were consistent within the expected minor variations in detector resolution and energy scale calibration. A 0.2% linear shift in energy scale between detectors, as discussed in Sec. III B 5 b, corresponded to a 0.05% shift in efficiency, as evaluated from the observed data. With slightly more rigor, correlations of position-dependent variations in energy scale and n-Gd efficiency were considered. Variations in energy scale between detectors were compared using data from 16 regions of equal volume within the GdLS target. Simulation of the n-Gd capture spectrum in each region determined the relative impact of energy scale variations on the efficiency of each region. A volume-weighted average over the entire GdLS target estimated potential variations in efficiency between detectors of 0.07%.

An alternate technique, outlined in [38], provided a more general approach for assessing this uncertainty. The efficiency for each detector i is equivalent to the ratio of the number of n-Gd signals above the 6 MeV threshold, N_i^{d}, to the total number of n-Gd signals, N_i^{t},

$$\epsilon_i = \frac{N_i^{\mathrm{d}}}{N_i^{\mathrm{t}}}. \qquad (17)$$

It was not possible to directly measure N_i^{t}, given that backgrounds overwhelmed the observed spectra for $E_{\mathrm{d}} < 3.6$ MeV. The number of signals above 3.6 MeV, N_i^{a}, served as a close approximation for N_i^{t}, given that it contained $\sim 99\%$ of all n-Gd capture signals. Therefore, differences in the ratios of N_i^{d} to N_i^{a} among the detectors were strongly correlated to potential variations in efficiency ϵ_i. Explicitly, a linear model

$$\bar{N}_i^{\mathrm{d}} = a + bN_i^{\mathrm{a}} \qquad (18)$$

was fit to the distribution of N_i^{d} versus N_i^{a} for the eight detectors. The model estimate of $\bar{N}_i^{\mathrm{d}}$ for each detector showed small deviations from the observed N_i^{d}. Variation in the efficiency of each detector from the model average, $\delta\epsilon_i/\epsilon_i$, was then given by

$$\frac{\delta\epsilon_i}{\epsilon_i} = \frac{\delta N_i^{\mathrm{d}}}{N_i^{\mathrm{d}}} = \frac{N_i^{\mathrm{d}} - \bar{N}^{\mathrm{d}}(N_i^{\mathrm{a}})}{N_i^{\mathrm{d}}} = 1 - \frac{a + bN_i^{\mathrm{a}}}{N_i^{\mathrm{d}}}. \qquad (19)$$

Variations of 0.08% were observed among the detectors, which was adopted for the analysis here.

Figure 19 shows the distribution of prompt versus delayed energy for all signal pairs which satisfied the $\bar{\nu}_e$ selection criteria. Only the $E_{\mathrm{d}} > 6$ MeV selection truncated a significant fraction of true signal events, which visibly span the boundary of the selected region.
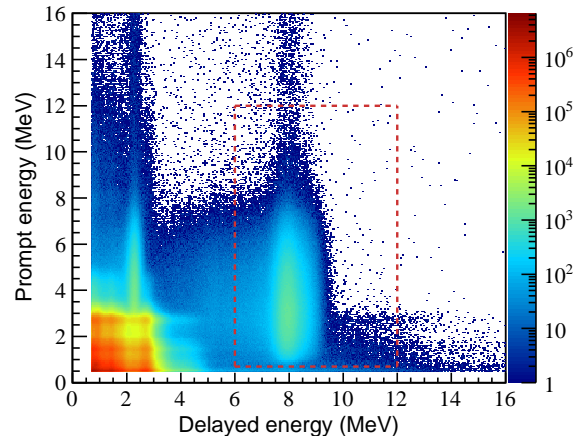

FIG. 19. The distribution of prompt versus delayed energy for signal pairs which satisfied the $\bar{\nu}_e$ inverse beta decay selection criteria. Interactions with prompt energy of 0.7 MeV $< E_{\mathrm{p}} < 12$ MeV and delayed energy of 6 MeV $< E_{\mathrm{d}} < 12$ MeV were used for the neutrino oscillation analysis discussed here (red dashed box). A few-percent contamination from accidental backgrounds (symmetric under interchange of prompt and delayed energy) and ^{9}Li decay and fast neutron backgrounds (high prompt and ~ 8 MeV delayed energy) are visible within the selected region. Inverse beta decay interactions where the neutron was captured on ^{1}H provided an additional signal region with $E_{\mathrm{d}} \sim 2.2$ MeV, albeit with much higher background.

B. Background Rejection

The vast majority of triggered signals in each detector were caused by natural radioactive backgrounds, with less than one in $\sim 10^5$ resulting from reactor $\bar{\nu}_e$ interactions. This section describes the methods employed to reduce background contamination to less than a few percent of the reactor $\bar{\nu}_e$ sample used to measure neutrino oscillation. Aside from natural radioactivity, a minor PMT instrumentation-related background was discovered during detector assembly and commissioning. Rejection of this instrumental background is also discussed here. Selecting pairs of prompt plus delayed signals with the proper energies and time separations rejected almost all backgrounds caused by natural radioactivity. Occasionally two such uncorrelated interactions would *accidentally* satisfy the antineutrino selection criteria. Detailed studies of all uncorrelated interactions measured this background contamination to be from 1% to 2% depending on detector, with negligible uncertainty. All remaining backgrounds were from physical processes that produce a pair of correlated interactions that potentially mimic inverse

beta decay. The majority of such correlated background were attributable to atmospheric muons produced in cosmic ray showers. Energetic muons penetrated the rock to reach the experimental halls, and interacted with the detector or nearby environment. Vetoing signals that occur during and soon after muon interactions with the detector or muon systems effectively reduced the contamination caused by these backgrounds to less than 0.5%. Lastly, three or more signals would occasionally occur close in time, resulting in confusion as to which pair was most likely the result of an antineutrino interaction. To avoid this ambiguity, sets of signals with multiplicity >2 were rejected. The detailed characterization and mitigation of these backgrounds are presented in the following sections.

1. Instrumental Background

Assessment of the PMTs during detector assembly revealed that some PMTs emitted light. Such emission is commonly called *flashing*, although the mechanism of light emission can vary between PMT designs. For the Daya Bay PMTs, direct imaging of the base using an astronomical CCD camera pinpointed the light emission to an electrical discharge occurring at the point of connection of the incoming HV cable with the base circuit board. Most of the PMTs were found to emit light at some level, with rates and intensities which varied over time. Once installed within an AD, the black radial shield prevented most of the emitted light from entering the central AD volume. A small fraction of the light propagated within the PMT, striking the photocathode or passing into the scintillator region. The emitted light produced background signals with reconstructed energies up to ~100 MeV, with a rate in the energy range of the delayed IBD signals (6 MeV to 12 MeV) of approximately 0.7 Hz per AD.

Were they not removed, these false delayed signals would have contributed a significant accidental background, comparable to the observed antineutrino rate. Fortunately, these signals had characteristic patterns in space and time, easily distinguishable from genuine particle interactions within the scintillator. In particular, both the discharging PMT and those PMTs directly opposite within the AD observed a large fraction of the charge. Figure 20 shows a typical charge distribution from PMT light emission.

A parameter was constructed to discriminate PMT light emission from genuine particle interactions. For every triggered signal, the single PMT which observed the greatest charge, Q_{max}, was identified as a potential light emitter. The spatial charge distribution of the AD signal was then quantified using two variables, f_{max} and f_{quad}. f_{max} was the ratio of the maximum PMT charge over the total observed charge, Q_{max}/Q_{total}. The twenty-four columns of PMTs in one AD were grouped into four quadrants such that the potential emitter was at the center of the first quadrant. The total charge observed in the i-th quadrant was defined as Q_{qi}. f_{quad} was the ratio of the charge observed in the opposite quadrant over the two adjacent quadrants, $f_{quad} = Q_{q3}/(Q_{q2} + Q_{q4})$. The discriminator, f_{ID}, combined these
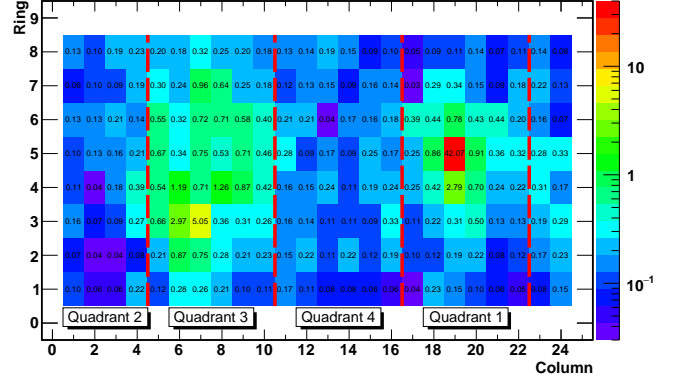

FIG. 20. Typical charge distribution from PMT light emission. The 8 ring by 24 column cylindrical PMT array has been projected onto a plane. The logarithmic color scale, as well as numbers, provides the percentage of the total signal charge observed by each PMT. In this example, light was emitted by the PMT at column 19 in ring 5. The discharging PMT and those PMTs directly opposite in Quadrant 3 observed a significant fraction of the total charge. The distinct charge pattern allowed efficient rejection of this instrumental background.

two aspects of the spatial distribution of light,

$$f_{ID} = \log_{10}\left[f_{quad}^2 + \left(\frac{f_{max}}{0.45} \right)^2 \right]. \quad (20)$$

Figure 21 shows the normalized distributions of this discriminator for the delayed signals of the antineutrino candidates, including the background from PMT light emission. The discriminator had a consistent distribution for
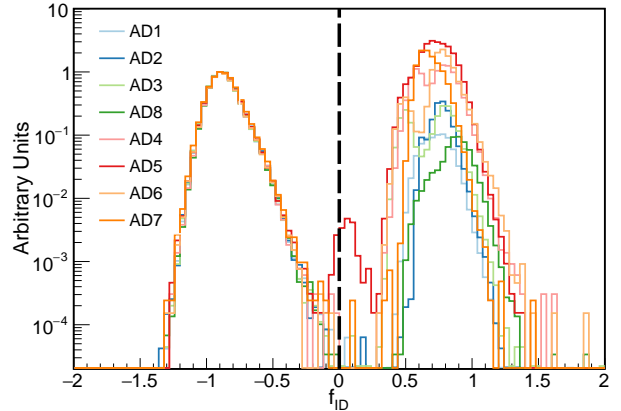

FIG. 21. Distributions of the discriminator f_{ID} for all inverse beta decay delayed signal candidates from the eight detectors. The distributions are normalized to demonstrate the consistency of the distributions among the ADs for genuine antineutrino candidates ($f_{ID} < 0$), while the background distributions depended on the characteristics of the light-emitting PMTs in each AD ($f_{ID} \geq 0$).

genuine IBD candidates ($f_{ID} < 0$) among the eight ADs,

while the signals from light emission ($f_{ID} \geq 0$) varied as a result of the particular characteristics of the light-emitting PMTs in each AD. Light emission by a PMT located in the bottom ring of AD5 produced the small peak near $f_{ID} = 0$ in Fig. 21.

PMT light emission also generally exhibited a broader distribution of relative times between the PMT signals. An additional discriminator, f_{t1}, was defined as the ratio of the number of PMT signals in the first 200 ns of the signal, relative to the total number of PMT signals in the first 400 ns. The variable f_{t2} was the same except for only using the number of PMT signals in the first 150 ns in the numerator. A time-based discriminator f_{PSD} combined these two variables using an optimized weighting,

$$f_{PSD} = \log_{10}\left[4 \cdot (1 - f_{t1})^2 + 1.8 \cdot (1 - f_{t2})^2\right]. \quad (21)$$

Signals with $f_{PSD} \geq 0$ were identified as PMT light emission and rejected from further studies. This discriminator had the added benefit of rejecting pile-up, in which two independent particle interactions occurred within a single triggered readout of the detector.

Each AD also included six 2-inch PMTs which were located at the top and bottom of the detector adjacent to the paths for ACU calibration deployment. These PMTs were used to monitor the scintillator characteristics, and were not employed for triggering or energy and position reconstruction. Light emission by these PMTs was easily rejected whenever the charge observed by any one of them exceeded 100 PE.

After applying the f_{ID} and f_{PSD} discriminators, negligible background from PMT light emission remained in the antineutrino candidate sample. A study of high-purity samples of particle interactions showed that very few were incorrectly rejected by these discriminators, and an efficiency of 99.98% was determined for antineutrino signals. Negligible uncertainties of 0.01% correlated among the detectors and 0.01% uncorrelated among the detectors were also determined from this study. Any residual light emission was incorporated into the assessment of uncorrelated backgrounds, as discussed in the next section.

2. Uncorrelated Backgrounds

Two uncorrelated signals occasionally satisfied the antineutrino selection criteria, giving rise to backgrounds that are commonly referred to as *accidentals*. The rate, energy spectrum, and other characteristics of these backgrounds were precisely modeled from studies of individual uncorrelated signals. Each day, only a few of the $\sim 10^7$ uncorrelated signals were estimated to form a pair which satisfied the antineutrino selection. As a result, the residual accidental backgrounds in the final sample of antineutrino candidates were reliably determined to be only $\sim 1\%$ in the near detectors and $\sim 2\%$ in the far detectors, with negligible systematic uncertainty. The detailed assessment of this background is discussed here.

An uncorrelated signal was identified as prompt-like if it satisfied the prompt energy selection 0.7 MeV $<$ $E_{rec} < 12$ MeV. Correspondingly, it was also identified
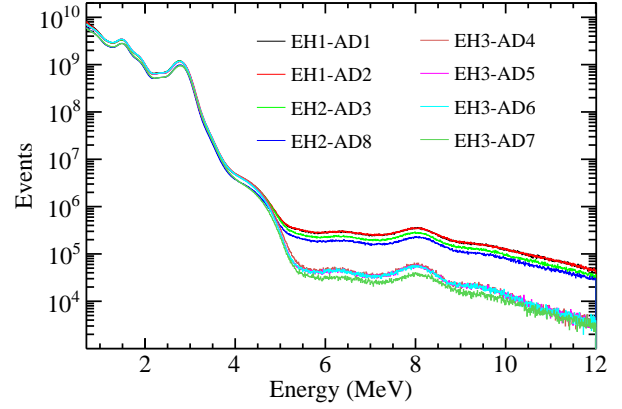

FIG. 22. The reconstructed energy spectra of isolated uncorrelated signals for all eight detectors. The prompt-like signal rate was dominated by natural radioactivity with energies below 3 MeV. The delayed-like signal rate was dominated by beta decay of muon-induced unstable isotopes, mainly ^{12}B, and γ-rays from capture of ^{241}Am-^{13}C calibration source neutrons on materials at the top of each detector. The energy spectrum of the accidental background prompt signals in each AD were equivalent to these distributions.

as delayed-like if it satisfied 6 MeV $< E_{rec} < 12$ MeV. The majority of prompt-like uncorrelated signals were from natural radioactivity in the detector components and the surrounding environment, and had $E_{rec} < 3$ MeV. Delayed-like uncorrelated signals were primarily from two sources. Muon-nuclear interactions produced unstable nuclei within the detectors, which would subsequently beta decay. ^{12}B was by far the most prominent of such isotopes, although others such as ^{12}N were also produced. The second were high-energy γ-rays produced by the capture of neutrons emitted by the ^{241}Am-^{13}C calibration sources located in the ACUs on the AD lid. A small fraction of these γ-rays reached the scintillator volume and produced delayed-like signals. Figure 22 shows the reconstructed energy spectrum for all isolated prompt-like signals for all eight detectors. Note that uncorrelated signals which occurred during time periods vetoed by the muon or multiplicity selections were appropriately excluded from the studied samples. Delayed-like signals were the subset with $E_{rec} > 6$ MeV. The prompt signal energy spectra of the accidental background for each detector were estimated directly from these distributions.

The accidental background was modeled using combinations of these uncorrelated prompt-like and delayed-like signals. The accidental background rate for selection A was

$$R_{acc}^A = R_d \left(1 - e^{-R_p \Delta t}\right) e^{-2R_p \Delta t}, \quad (22)$$

where R_p was the measured rate of prompt-like signals, R_d was the measured rate of delayed-like signals, and $\Delta t \cong 200$ μs was the length of the time window for selection of antineutrino candidate pairs. The factor in parentheses was the probability for an uncorrelated prompt-like signal to fall in the selected time window preceding a delayed-like signal. The final term accounted for the efficiency of

the multiplicity veto, which rejected accidental backgrounds when a second prompt-like signal occurred either before the prompt or after the delayed signal. Given that all other antineutrino selection criteria (e.g. light emission rejection, muon veto, etc.) were applied when selecting uncorrelated signals for the calculation of $R_{\rm p}$ and $R_{\rm d}$, the estimated background rate $R_{\rm acc}^{\rm A}$ automatically included these selection efficiencies.

The slight difference in the multiplicity requirement for selection B, as outlined in Table II, resulted in an alternate expression for the rate of accidental backgrounds. The accidental rate for selection B was

$$R_{\rm acc}^{\rm B} = R_{\rm d}\, R_{\rm p}\, \Delta t\, e^{-2R_{\rm p}\Delta t}\, e^{-R_{\rm d}\Delta t}. \tag{23}$$

The rates of uncorrelated signals varied over time for each detector. For the first few months following commissioning of each detector, the prompt-like signal rate $R_{\rm p}$ showed an initial decline of $\sim$20% attributed to removal of natural radioactivity during purification of the water in the Water Shields. The rates eventually stabilized in the range of 55 Hz to 60 Hz for all eight detectors. As can be seen in Figure 22, $R_{\rm p}$ was dominated by signals which occurred just above the 0.7 MeV selection threshold. Small changes in the electrical noise environment within each experimental hall would result in slight changes in the efficiency of this threshold. These shifts are consequently visible as slight instability in the rate of accidental background versus time. The delayed-like signal rate $R_{\rm d}$ showed significant differences between experimental halls; a decrease in the muon flux versus hall depth resulted in a corresponding reduction in ^{12}B production. The neutron production by the ^{241}Am-^{13}C sources declined over time, which reduced the delayed-like rate of high-energy γ-rays from this source. During installation of the final two detectors in the summer of 2012, the ^{241}Am-^{13}C sources were removed from ACU-B and ACU-C for all detectors in EH3. While reduction of the ^{241}Am-^{13}C correlated background was the primary purpose, as will be described in the next section, it had the added benefit of cutting the delayed-like signal rate in half for the far detectors. In summary, each detector initially had about 1000 (EH1), 800 (EH2), and 250 (EH3) delayed-like signals per day, but this has declined by $\sim$20% for the near detectors and $\sim$65% for the far detectors. Since the rates of uncorrelated signals varied with time, so did the accidental background. Consequently, the data was divided into short intervals in time and the accidental background was independently estimated for each. For selection A, these periods corresponded to every four hours, while for selection B this was once every day. Figure 23 shows the estimated rate of accidental background for each detector as a function of time.

The accidental rates determined according to Eqs. 22 and 23 were cross-checked by using an *offset-window* method. In this approach the antineutrino selection was repeated, but with a time offset $t^{\rm off}$ introduced between prompt and delayed signal pairs (i.e. $1\ \mu{\rm s} + t^{\rm off} < \Delta t < 200\ \mu{\rm s} + t^{\rm off}$). A minimum offset of 1 ms suppressed correlated signals such as IBD, fast neutrons, and ^{9}Li, thereby providing a sample enriched in accidental background. Repeating the
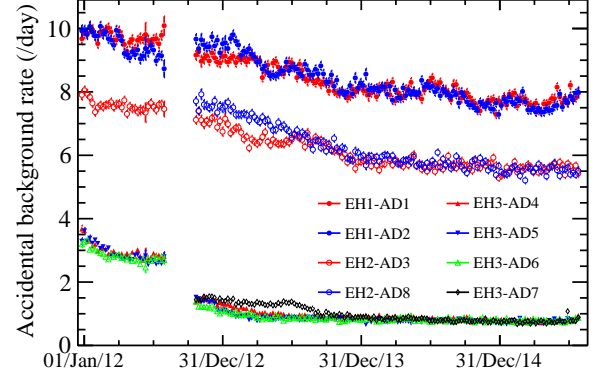

FIG. 23. The accidental background rate for selection A as a function of time for each antineutrino detector, as calculated from measurements of the rates of uncorrelated signals which satisfy the prompt $\overline{\nu}_e$ signal selection, $R_{\rm p}$, and delayed $\overline{\nu}_e$ signal selection, $R_{\rm d}$. The accidental rate primarily depended on experimental hall depth due to the relative rate of unstable isotope production by muons. The decline of the accidental background versus time was due to combination of a decrease in the natural radioactivity following detector installation and a reduction of the neutron emission by the ^{241}Am-^{13}C calibration sources. $R_{\rm p}$ was sensitive to small changes in electrical noise, which resulted in the observed instability in the accidental background rate. Installation of the final two detectors in the summer of 2012 is evident as a gap during this time. Removal of two of the three ^{241}Am-^{13}C sources in each far detector during the installation period reduced the accidental background rate by $\sim$50%.

process with $t^{\rm off}$ from 1 ms to 20 ms in 200 μs steps increased the statistical precision of this method. Figure 24 shows the distribution of distances between the reconstructed positions of the prompt and delayed signals, $\Delta r_{\rm p,d}$, for the $\overline{\nu}_e$ candidates and for the accidental background determined using this method. Genuine correlated signals favor small $\Delta r_{\rm p,d}$, as shown by simulation, while accidentals dominate for $\Delta r_{\rm p,d} > 2$ m. Both the shape and normalization of the accidental background distribution agreed with that of the $\overline{\nu}_e$ candidate sample for $\Delta r_{\rm p,d} > 2$ m, confirming the estimate of this background. The rate determined from the offset-window method was also consistent with those obtained using Eqs. 22 and 23, albeit less precise.

Uncertainty in the estimation of the accidental background was negligible. The largest statistical contribution was from the uncertainty in $R_{\rm d}$, which was 0.2% in the near detectors and 0.4% in the far detectors. Variation in the methods used to select only isolated prompt-like signals resulted in 0.3% variation in $R_{\rm p}$ in the most extreme cases. In the end, the total uncertainty was dominated by the 1% precision of the cross-check of the accidental rate using the offset-window method, which was used as a conservative estimate of potential systematic uncertainty. Given that the estimated accidental background contamination amounted to only 1% to 2% of the antineutrino candidates, accidentals contributed $\lesssim$0.01% uncertainty to the observed rate of antineutrinos.
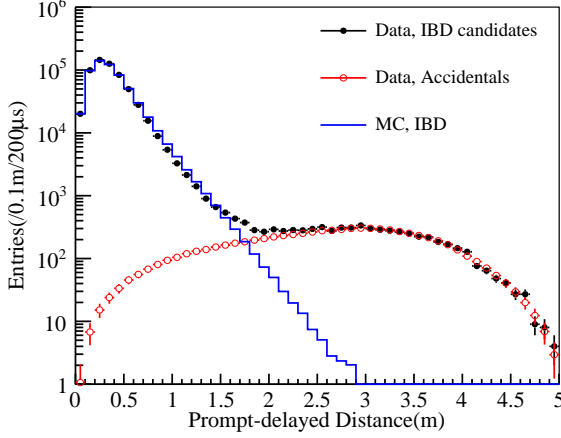
FIG. 24. Distribution of distances between the reconstructed positions of the prompt and delayed signals of the antineutrino inverse beta decay candidate signals from all detectors (black points). The positions were highly correlated for true $\bar{\nu}_e$ interactions, as demonstrated by Monte-Carlo simulation (blue line). Repeating the selection of $\bar{\nu}_e$ interactions, but with the time window for selection of the delayed signals offset by 1 ms to 20 ms, enhanced the uncorrelated accidental background (red points) and suppressed correlated signals. The consistency of the distributions confirmed the estimate of contamination by accidental backgrounds, which varied from 1% to 2% depending on detector.

3. Correlated Backgrounds

The remaining backgrounds were from physical processes which produced correlated pairs of prompt and delayed signals, capable of mimicking $\bar{\nu}_e$ inverse beta decay. Six potential sources of correlated backgrounds were identified:

- Muons: Muons produced in cosmic ray showers would fragment stable nuclei in or near the detectors, creating free neutrons and unstable nuclei. The signals from the initial muon interaction, subsequent neutron captures, or beta decays of unstable nuclei could potentially form a pair which satisfied the antineutrino selection. Muons were easily identified by their large scintillation light production or by Cherenkov light in the water shield. Vetoing concurrent or subsequent signals rendered this background negligible, at the cost of 2% of the far-hall and 14%–18% of the near-hall livetimes.

- Fast neutrons: Muon interactions in the environment near the detector generated energetic, or *fast*, neutrons. A nuclear collision of a fast neutron within the scintillator could mimic a prompt signal, while the subsequent neutron capture was identical to a true IBD delayed signal. The contamination from this background was $\lesssim 0.1\%$.

- β-n decays: Muon interactions occasionally produced the rare unstable isotopes ^{9}Li and ^{8}He, which β-decay with a chance of simultaneously emitting a neutron. The muon veto reduced contamination from this

background to 0.3%–0.4% depending on experimental hall, with a $\sim$50% systematic uncertainty.

- ^{241}Am-^{13}C neutron sources: During detector operation it was found that neutrons from the ^{241}Am-^{13}C calibration sources within the ACUs occasionally introduced several γ-rays, correlated in time, into the detector. Contamination from this backgrounds was $\lesssim 0.1\%$.

- (α,n) interactions: α's emitted by natural radioactivity within the detector could eject neutrons from stable nuclei, with ^{13}C(α,n)^{16}O being the most prevalent interaction. Protons scattered by the neutron or ^{16}O* de-excitation γ-rays could mimic a prompt signal, while the eventual neutron capture provided a delayed signal. Contamination from this background was $\lesssim 0.07\%$.

- High-multiplicity signals: The pile-up of correlated $\bar{\nu}_e$ signal pairs with uncorrelated radioactive backgrounds resulted in three or more signals within the correlation time for IBD candidates. While not a background per se, such sets of signals with multiplicity $\geq$3 resulted in ambiguity in determination of the actual prompt and delayed $\bar{\nu}_e$ signals. Complete rejection of these high-multiplicity combinations resolved this ambiguity, but introduced a $\sim$2.5% loss of $\bar{\nu}_e$ efficiency.

The characteristics of each of these backgrounds, the methods used to mitigate them, and their residual contamination in the $\bar{\nu}_e$ candidates will be discussed in the following sections. The mitigation methods, e.g. the muon and high-multiplicity vetoes, and their associated impact on $\bar{\nu}_e$ detection efficiency, are also presented here. Of the correlated backgrounds, only β-n decays contributed enough residual background contamination as well as systematic uncertainty to significantly impact the oscillation measurement.

a. Muon Background and Veto Minimization of the muon background was a primary reason behind the selection of the Daya Bay site for the measurement of neutrino oscillation. The mountains directly adjacent to the nuclear power facility provided ample shielding for each experimental hall, as listed in Table I. The attenuated muon fluxes for EH1, EH2, and EH3 were found to be 1.16, 0.86, and 0.054 Hz/m^2 respectively, defined according to a spherical acceptance [33].

Muons which traversed the antineutrino detectors deposited an average of $\sim$0.6 GeV in the scintillator, and were easily discriminated from antineutrino signals. Selection A identified these *AD muons* as any signal with reconstructed energy $>$20 MeV, while selection B used any signal with $>$3,000 PE ($\gtrsim$18 MeV). Any delayed-like candidate signal following an AD muon signal within a veto time window of $t_{AD\mu}^{veto}$ was rejected. This veto was applied independently for each antineutrino detector. For selection A, $t_{AD\mu}^{veto} = 1$ ms, while selection B used a longer 1.4 ms veto to avoid correlations between the muon and multiplicity veto efficiencies. The length of the veto was dictated by the timescale for neutron capture in the antineutrino detectors. Although the veto may seem rather long in comparison with the $\sim$28 μs neutron capture time in the GdLS target, some

neutrons lingered in the LS region and slowly diffused into the GdLS. Given a mean neutron capture time in the LS region of ~200 μs, the veto corresponded to an $\sim \exp(-5)$ (or $\sim \exp(-7)$, for selection B) suppression for such neutrons.

Both of the selections identified *Water Shield muons* as any signal in either the IWS or OWS in which more than 12 PMTs were above threshold. Neutrons generated by muon interactions in the water shield also had the potential to reach the GdLS target, although with a much lower probability. A shorter veto time of $t_{\mathrm{WS}\mu}^{\mathrm{veto}} = 600$ μs was sufficient to reject these neutrons. As discussed in Sec. II, the IWS, OWS, and AD were all independently triggered. Small differences in detector latency resulted in some AD signals arriving in advance of simultaneous signals in the water shield. Therefore, any delayed-like AD signal which occurred in the 2 μs preceding a WS muon was also rejected. This veto was applied to all ADs within an experimental hall for both selections A and B.

A minority of muons produced a significantly higher proportion of neutrons and unstable nuclei in the ADs. Such interactions were associated with scintillation light production in excess of that expected for minimum-ionizing muons, and were assumed to be associated with muon-induced particle showers. Selection A identified these *AD showers* as any signal with reconstructed energy >2.5 GeV, while selection B used any signal with >30,000 PE ($\gtrsim$1.8 GeV). The veto time following these signals, $t_{\mathrm{shower}}^{\mathrm{veto}}$, was significantly longer; 1 s for selection A and 0.4 s for selection B. This significantly longer veto was necessitated by the 178.3 ms half-life of ^{9}Li, as will be discussed. This veto was applied independently to each detector for both selections A and B.

The combination of these muon veto criteria resulted in negligible background contamination from muons, with the exception of fast neutrons and β-n decays discussed in the following sections.

The veto reduced the livetime for $\overline{\nu}_e$ detection, which was quantified as an effective contribution ϵ_μ to the antineutrino selection efficiency for each detector. This efficiency was directly measured from the data using

$$\epsilon_\mu = \left(\sum_i t_{\mathrm{s}}^i\right)/t_{\mathrm{DAQ}}, \qquad (24)$$

where t_{s}^i were the individual segments i of livetime between each vetoed period in a detector. The total DAQ livetime, t_{DAQ}, was the time between the first and last signal in the data period, accounting for gaps in the data due to downtime and periods of poor data quality. The resulting efficiency was ~82%, ~86%, and ~98% for the detectors in EH1, EH2, and EH3, respectively. The dominant uncertainty in this calculation was from jitter in the recorded time of each signal, but was found to be negligible.

b. Fast Neutron Background While muon interactions within the detectors or water shield were efficiently identified, interactions with the cavern rock surrounding the experimental hall were missed. Neutrons produced in these interactions could reach the detectors without producing a detectable signal in the water shield. In order to attenuate these neutrons,

the thickness of the water shield surrounding the ADs was at least 2.5 m in all directions. As a result, only the most energetic, or *fast*, neutrons had the potential to penetrate all the way to the GdLS target. A fast neutron could stop in the scintillator target through an energetic collision with a nucleus, primarily ^{1}H. Ionization of the scintillator by a recoiling proton could mimic a prompt $\overline{\nu}_e$ interaction, while the slowed neutron could capture and provide a delayed signal.

The broad and smooth energy spectrum of recoils from fast neutrons resulted in a reconstructed prompt spectrum that was approximately flat up to energies of ~100 MeV. Fast neutrons were the dominant correlated signal at these high energies. Correlated signals with prompt energy greater than the selection for $\overline{\nu}_e$ interactions, $E_{\mathrm{p}} >$12 MeV, were used to directly measure this background. A smooth extrapolation of the background into the $\overline{\nu}_e$ prompt energy range, 0.7 MeV< E_{p} <12 MeV, provided an initial estimate of the contamination of this background in the $\overline{\nu}_e$ sample.

Although simulation supported the validity of a linear extrapolation of this background into the $\overline{\nu}_e$ signal region, a method which solely relied on data was more robust. The energy spectrum of prompt recoils was directly measured using $\overline{\nu}_e$-like correlated signals coincident with muons. In particular, a sample of *boundary muons* were selected when a muon was identified only in the OWS or the RPC, but not in the IWS. Figure 25 compares the observed prompt energy spectra for the standard antineutrino candidate sample for selection A but with the prompt signal extended up to 100 MeV. The spectra for candidates whose delayed signal was within 200 μs after a boundary muon are also shown. The energy spectra above 12 MeV were consistent for the two samples, and the prompt recoil spectrum in the range of 0.7 MeV to 12 MeV is clearly visible for the boundary muon sample. The spectra from only the OWS or the RPC boundary muon samples are also consistent with each other.

The residual fast-neutron contamination rate R_{fn}^i in the $\overline{\nu}_e$ sample for each detector i was estimated from the observed rate of $\overline{\nu}_e$-like candidates with high prompt energy, 12 MeV $\leq E_{\mathrm{p}} \leq$ 99 MeV, R_{he}^i. The fast neutron sample identified, or *tagged*, using boundary muons was used to estimate the proportion of the background in the low energy region of interest, 0.7 MeV< E_{p} <12 MeV. The tagged spectra were consistent between detectors, so the entire tagged sample from all eight detectors was combined to improve the statistical accuracy of this technique. From the tagged fast neutron rate at low, R_{fn}^μ, and high, R_{he}^μ, prompt energies, the actual fast neutron background rate was determined as

$$R_{\mathrm{fn}}^i = R_{\mathrm{he}}^i \frac{R_{\mathrm{fn}}^\mu}{R_{\mathrm{he}}^\mu}. \qquad (25)$$

This method found the fast neutron contamination in the $\overline{\nu}_e$ candidate sample to be less than $\lesssim$0.1% for all detectors. The contamination varied by a negligible amount, $\lesssim$0.03%, assuming a range of variations in spectra between the tagged and untagged fast neutron samples.

c. β-n Decay Background An unstable nuclide which β-decayed with the simultaneous emission of a neutron
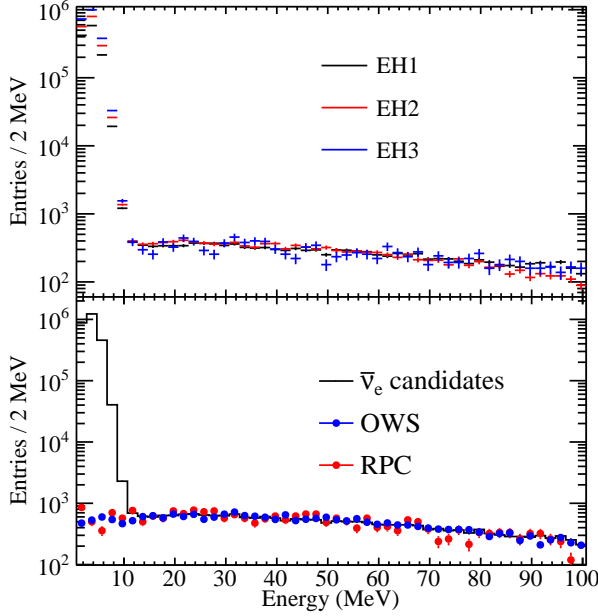
FIG. 25. (*Top*) An expanded selection of $\overline{\nu}_e$ candidate signals with prompt energies from 0.7 MeV to 100 MeV revealed a broad continuum of background, attributed to energetic, or *fast*, neutrons. Actual $\overline{\nu}_e$ signals were visible as the dominant signals below $\sim$12 MeV. The energy spectra of the fast neutron background above 12 MeV were similar in all three experimental halls (EH1: black, EH2: red, EH3: blue). (*Bottom*) The sum of the $\overline{\nu}_e$ candidate spectra from all three halls (black line) was compared to a high-purity fast neutron sample obtained by selecting those $\overline{\nu}_e$ candidate signals which had been vetoed in the 200 μs after an OWS or an RPC, but not an IWS, muon signal (OWS: blue, RPC: red). The energy spectra of the vetoed samples were consistent with the background observed above 12 MeV in the $\overline{\nu}_e$ candidate sample. The normalization of the vetoed samples were adjusted to match the $\overline{\nu}_e$ candidates above 12 MeV. The fast neutron contamination in the $\overline{\nu}_e$ candidate sample below 12 MeV was estimated using the vetoed sample.

generated a correlated pair of signals nearly identical to those from $\overline{\nu}_e$ inverse beta decay. The production of β-n nuclides by muon spallation in organic liquid scintillator has been measured [41]. ^{9}Li, with a lifetime of $\tau = 257.2$ ms and a maximum β energy of 13.6 MeV, and ^{8}He, with a lifetime of $\tau = 171.8$ ms and maximum β energy of 10.7 MeV, are the most prominent β-n nuclides. A FLUKA-based simulation suggested that the dominant production method was the fragmentation of ^{12}C by π^- in muon-induced hadronic showers, with a relative yield of 10:1 for these two β-n nuclides [41].

The natural site-dependent variation in β-n production presented the most direct route for a potential bias in the far versus near detector measurement of neutrino oscillation. As will be shown, uncertainty in the β-n background contributed the most significant systematic uncertainty in the oscillation measurement.

β-n background was discriminated from $\overline{\nu}_e$ interactions by association with a preceding muon signal in the same detector. This association was complicated by the high muon

rates in the detectors relative to the lifetime of these nuclides, rendering signal-by-signal discrimination impossible. Still, the distribution of times between each $\overline{\nu}_e$ candidate and the most recent AD muon signal could be used to estimate the β-n production rate [42], allowing statistical estimation of this background. The distribution of total correlated signal rate R_{total} versus time since the most recent muon signal was expressed

$$R_{\text{total}} = R_{\text{IBD}} R_\mu e^{-R_\mu t} + \sum_i^{^9\text{Li},^8\text{He},^{12}\text{B}} R_i \lambda_i e^{-\lambda_i t}, \quad (26)$$

where $\lambda_i = R_\mu + \frac{n_i}{\tau_i}$ was the effective time constant for nuclide i with lifetime τ_i and rate R_i, accounting for the impact of the muon rate R_μ. The factor n_i is 1 for ^{9}Li and ^{8}He. A term for ^{12}B with n_i equal 2 was included to accommodate a potential increase in the background following muons, where two ^{12}B decays mimicked a prompt and delayed $\overline{\nu}_e$ signal.

A fit to the distribution of R_{total} for all $\overline{\nu}_e$ candidates, not including the muon veto, unfortunately does not provide a precise estimate of the β-n background. As reported previously [41], unstable isotope production was generally associated with muons which yield significantly higher scintillation light and was attributed to energetic particle showers. Limiting the time distribution to the most recent *AD shower*, as defined earlier, enhanced the signature of β-n decays relative to $\overline{\nu}_e$ signals. Also, accidental background in the distribution was suppressed by further limiting the sample to correlated signals with 3.5 MeV $< E_p <$ 12 MeV, and 1 μs $< \Delta t <$ 100 μs. From the modeled spectra of ^{9}Li and ^{8}He, this selection reduced the β-n acceptance to 67%. Figure 26 shows the resulting distribution for selection A, with the contribution from ^{9}Li and ^{8}He clearly visible.

The observed β-n decay constant preferred ^{9}Li over ^{8}He, consistent with the observation by the KamLAND experiment. Varying the ^{8}He contribution from 0 to 15% resulted in only a 4% change in the estimated β-n rate. The veto following AD showers, 1 s for selection A and 0.4 s for selection B, removed the majority of this background. The residual background contamination following showering muons was estimated at <0.01% from integration of the tail of the fitted β-n time distribution beyond the veto window.

Although β-n production was primarily associated with muon-induced particle showers, a fraction of this background was also produced by those muons with no associated shower. While the β-n yield was expected to be much lower for an individual non-showering muon, this was compensated by the much higher non-showering muon rate. The high muon rate resulted in a time-since-muon distribution where the time constants for the β-n background and $\overline{\nu}_e$ signal are nearly degenerate. Therefore, an alternate technique was required. Given that β-n production required nuclear fragmentation, the presence of free neutrons was correlated with unstable nuclide production [43]. A neutron-tagged muon sample was identified as those muons which were followed within 20 μs to 200 μs by a potential neutron capture signal, identified using the loose criteria 1.8 MeV$<E_{rec}<$12 MeV. Table III
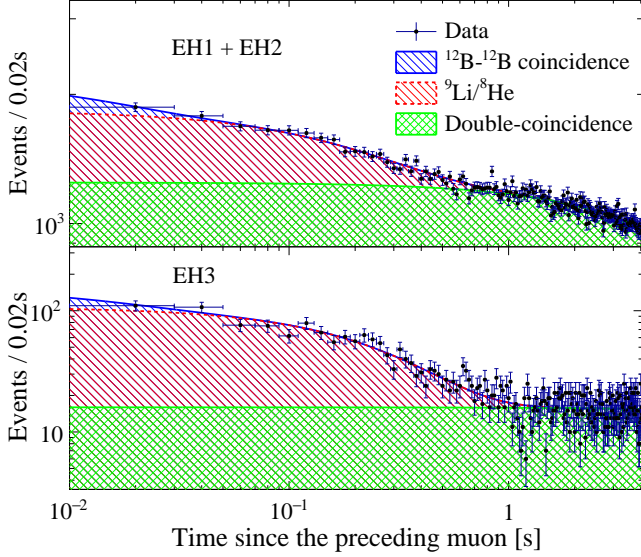
FIG. 26. The distribution of $\overline{\nu}_e$ inverse beta decay candidates versus time since the most recent muon-induced particle shower ($E_{rec} > 2.5$ GeV) in the same detector (blue points). A fit to this distribution statistically distinguishes the muon-uncorrelated $\overline{\nu}_e$ and accidentals (green hatched region), from the muon-correlated background from β-n decay (red lined region). A minor contribution from accidental background, where the delayed signal was from ^{12}B β decay, is barely visible in the first bin (blue lined region). A more restrictive $\overline{\nu}_e$ selection of 3.5 MeV $< E_p < 12$ MeV, and 1 μs $< \Delta t < 100$ μs suppressed the accidental contribution, providing a more precise estimate of the β-n background.

summarizes the number of β-n decays for all muons as well as for the the neutron-tagged subset, as estimated using the time distribution to the preceding muon (e.g. Fig. 26).

TABLE III. The estimated number of β-n decays in the $\overline{\nu}_e$ candidate sample from each experimental hall, based on the characteristics of the preceding muon. The values were determined from modeling the distribution of time since the preceding muon, as shown in Figure 26. Modeling the distribution for all muons with 0.02 GeV$<E_{rec}^{\mu}<1.8$ GeV was inconclusive. Instead, the values given in parentheses were estimated using the neutron-tagged sample, with the assumption that the efficiency of the neutron tagging of β-n production was independent of E_{rec}^{μ}.

Hall	Muon energy deposition, E_{rec}^{μ} [GeV]		
	0.02–1.8	1.8–2.5	>2.5
	β-n decays (all muons)		
EH1	(2106±193)	1169±185	4086±177
EH2	(1282±165)	879±162	3065±154
EH3	(276±36)	167±29	1142±43
	β-n decays (neutron-tagged muons)		
EH1	1847±169	818±63	3793±97
EH2	1087±140	614±47	2730±81
EH3	245±32	120±14	994±34

More than half of the β-n decays followed the small number of muons with associated particle showers, identified using

$E_{rec}^{\mu} > 2.5$ GeV. Muons with 1.8 GeV$<E_{rec}^{\mu}<2.5$ GeV contributed $<20\%$ of the estimated β-n decays. The estimates for muons with lower reconstructed energy, 0.02 GeV$<E_{rec}^{\mu}<1.8$ GeV, were inconclusive due to degeneracy of the β-n and $\overline{\nu}_e$ time constants in the distribution relative to those muons. Instead, β-n production by these muons was estimated using the neutron-tagged muon sample. For muons with $E_{rec}^{\mu}>1.8$ GeV, $\sim86\%$ of β-n production was found to follow neutron-tagged muons. The neutron-tagging efficiency for β-n production was assumed to be the same for those muons with $E_{rec}^{\mu}<1.8$ GeV. A limited variation in the observed tagging efficiency versus E_{rec}^{μ} was consistent with this assumption, with a $\sim40\%$ systematic uncertainty.

The total β-n background in the final $\overline{\nu}_e$ sample was determined using the values given in Table III, corrected for the selection efficiency and sample livetime. The showering muon veto efficiently rejected the contribution from muons with $E_{rec}^{\mu}>2.5$ GeV. The contamination was estimated at $(0.37\pm0.16)\%$, $(0.29\pm0.13)\%$, and $(0.20\pm0.08)\%$ per detector in EH1, EH2, and EH3 respectively.

An independent analysis of the β-n background was done for selection B. Although the shower muon threshold for selection B was more stringent, the veto time was less so. Analysis of the time distribution to all muons in the past 5 s, instead of only the most recent, resulted in a flat distribution for muon-uncorrelated $\overline{\nu}_e$ and accidental signals. Discrimination of the muon-correlated β-n component from this flat distribution was easier in principle, but came at the cost of increased statistical uncertainty from the larger number of muons considered in the study. Despite these alternate choices, this analysis found a similar background contamination of $(0.41\pm0.14)\%$, $(0.32\pm0.12)\%$, and $(0.30\pm0.09)\%$ per detector in EH1, EH2, and EH3 respectively.

In addition to measuring the β-n background rate, characterization of the energy spectrum was also necessary for the spectral analysis of neutrino oscillation. The prompt energy spectrum was determined from the β-n sample following muon-induced particle showers. An off-time window from 10 ms to 1010 ms after the shower was used to measure and then subtract the $\overline{\nu}_e$ and accidental contribution to the spectrum. Figure 27 shows the measured prompt energy spectrum. The poorer statistical precision at lower prompt signal energies was a consequence of the subtraction of the $\overline{\nu}_e$ and accidental signals. A prediction of the prompt energy spectrum was calculated from the known β-n decay of ^{9}Li. After decay, the nucleus fragments into an energetic neutron and two α-particles. An empirical model was constructed to match the observed branching β-n decay fractions [44], and observed neutron and α energy spectra [45, 46]. Although their impact on the spectrum was minor, the contribution of the neutron and α's to the observed energy were included based on the detector response model previously discussed. The spectrum was consistent with sole production of ^{9}Li, as also suggested by the fit to the lifetime.

d. ^{241}Am-^{13}C Neutron Source Background The three automated calibration units (ACUs) present on the lid of each antineutrino detector each contained a low-intensity ^{241}Am-^{13}C neutron source which was used to assess the response
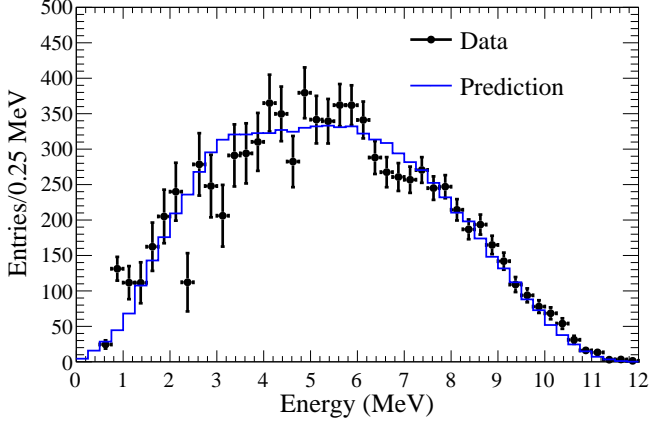
FIG. 27. A comparison of the observed (black points) and predicted (blue line) prompt reconstructed energy spectrum from ^{9}Li β-n decay. The observed spectrum was obtained from those $\overline{\nu}_e$ candidate interactions which followed muon-induced particle showers, with the expected background from $\overline{\nu}_e$ and accidentals subtracted. The prediction was estimated considering the known β-n decay branches and contribution from the nuclear break-up to a neutron and two α's.

of the detector to neutron capture [47]. When not in use for calibration, these $\sim$0.7 Hz neutron sources were withdrawn into each ACU. Concerns about correlated backgrounds motivated the choice and design of the neutron source. For example, ^{252}Cf was avoided due to the emission of multiple neutrons and associated γ-rays. In the chosen design, α's from an ^{241}Am source were degraded using a thin gold foil. With their energy reduced, they were below the threshold for γ-ray production upon interaction with ^{13}C. Design simulations had demonstrated that there was a negligible probability that a neutron emitted by the withdrawn source would reach the GdLS target and introduce background.

Despite these efforts, correlated signals were produced by the following rare mechanism. First, a neutron collided inelastically with an Fe, Cr, Mn, or Ni nucleus, present in the stainless steel of the detector, which emitted prompt γ-rays. The neutron was subsequently captured by a nucleus in the stainless steel, or by Gd present in the GdLS overflow tank, generating delayed γ-rays. When an energetic γ-ray from each of these prompt and delayed interactions happened to penetrate into and interact in the scintillator region of the detector, it could mimic a $\overline{\nu}_e$ interaction.

Initial observation of the background from the ^{241}Am-^{13}C sources came from an excess of uncorrelated γ-rays signals above the delayed signal threshold of $E_{rec} > 6$ MeV. This γ-ray excess had reconstructed positions primarily in the upper half of each detector [48], with a rate and energy spectrum in agreement with simulation. As discussed in Sec. IV B 2, these uncorrelated γ-rays enhanced the rate of accidental backgrounds. Monte-Carlo studies suggested the corresponding correlated background, discussed previously. The detailed modeling of this background is discussed in [49].

Simulation of the correlated background was uncertain

since it depended on accurate knowledge of many factors: the initial neutron energy spectrum, the γ-ray spectra of inelastic nuclear collisions, the eventual location and isotope of the neutron capture, and the penetration plus degradation of the γ-rays which reach the scintillator all impacted the modeling of this background. Therefore, an empirical approach was used to assess this background. A more intense $\sim$59 Hz ^{241}Am-^{13}C source was prepared and installed on the lid of EH3-AD5 for ten days during the summer of 2012. An increase in the rate of uncorrelated single interactions with $E_{rec} > 6$ MeV was measured in the upper half of the detector. An extra 613 ± 64 correlated backgrounds were observed in AD5 relative to the neighboring detector AD4, after accounting for the enhanced accidental background in the former. For the intense ^{241}Am-^{13}C source, the ratio of the rates of correlated to uncorrelated signals,

$$f^{int} = \frac{R_{corr}^{int}}{R_{uncorr}^{int}}, \qquad (27)$$

was $(1.5 \pm 0.3) \times 10^{-3}$. The simulation of this background was benchmarked against the observed signal rates, energy spectra, and distribution of reconstructed positions for both correlated and uncorrelated signals. Figure 28 shows the energy spectrum of uncorrelated ^{241}Am-^{13}C signals with $E_{rec} > 5$ MeV measured using the intense source. Simulation produced a consistent spectrum, with peaks attributed to prominent γ-rays from neutron capture on stainless steel. For correlated signal pairs, the γ-ray spectrum from prompt
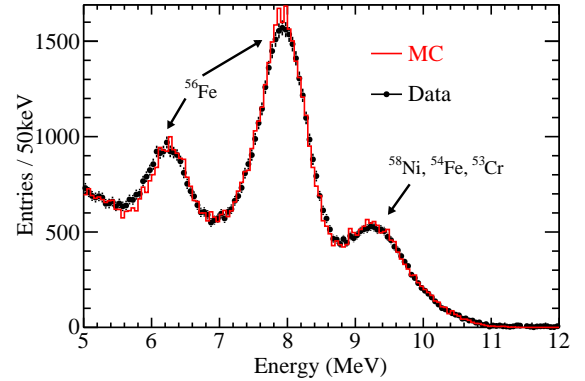

FIG. 28. Uncorrelated individual signals with $E_{rec} > 5$ MeV generated by a $\sim$59 Hz ^{241}Am-^{13}C neutron source temporarily installed on the lid of EH3-AD5 (black points). Peaks in the spectra are attributable to neutron capture on Fe, Cr, or Ni nuclei present in stainless steel of the lid, where an energetic capture γ-ray subsequently penetrates to the scintillating region of the detector. The measurement was used to benchmark a Monte-Carlo simulation of the uncorrelated and correlated background induced by this source (red solid line), and thereby estimate the correlated background induced by the regular weak $\sim$0.7 Hz ^{241}Am-^{13}C sources present in the automated calibration units (ACUs), also on the detector lid.

inelastic neutron collisions on nuclei in stainless steel is shown in Figure 29. The simulation predicted a consistent energy spectrum for prompt signals from both the intense
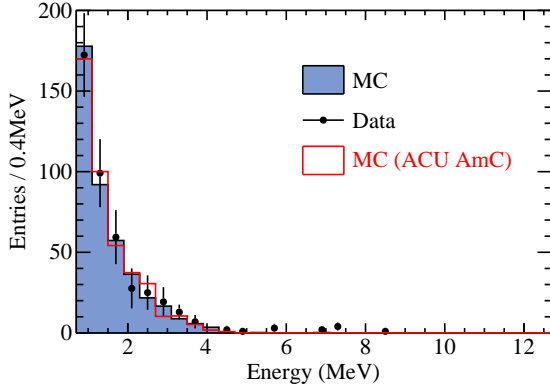
FIG. 29. The prompt reconstructed energy spectrum from correlated $\overline{\nu}_e$-like signal pairs induced by a ~59 Hz ^{241}Am-^{13}C neutron source temporarily installed on the lid of EH3-AD5 (black points). Inelastic collisions of a neutron with nuclei present in stainless steel produced γ-rays which occasionally penetrated to the scintillating region of the detector, generating signals with a steeply-falling energy spectrum. A benchmarked Monte-Carlo simulation predicted a consistent spectrum (solid blue region). The prompt energy spectrum for correlated background from the regular ~0.7 Hz ^{241}Am-^{13}C sources present in the automated calibration units (ACUs) was estimated to be identical, within the statistical precision of the simulation (red line).

and regular ^{241}Am-^{13}C sources. The prompt spectrum shape was effectively modeled using $S(E) = \exp(-E/E_o)$ with $E_o = 0.8 \pm 0.1$ MeV.

Simulation of the regular ^{241}Am-^{13}C sources predicted fewer correlated signals for an equivalent number of uncorrelated signals, given that they were located further from the scintillator. This offset was captured by a simulated double-ratio of the relative correlated-to-uncorrelated rates for the two sources,

$$\eta = \frac{f^{\text{reg}}}{f^{\text{int}}}, \tag{28}$$

where simulation predicted η to be 0.8 ± 0.2. The differences in rates for data and simulation determined the systematic uncertainty in η.

The rate of correlated background from the regular ^{241}Am-^{13}C sources, $R^{\text{reg}}_{\text{corr}}$, was estimated as

$$R^{\text{reg}}_{\text{corr}} = \eta f^{\text{int}} R^{\text{reg}}_{\text{uncorr}}, \tag{29}$$

where $R^{\text{reg}}_{\text{uncorr}}$ was the excess rate of uncorrelated signals with $E_{\text{rec}} > 6$ MeV attributed to the regular ^{241}Am-^{13}C sources. This method found a daily background rate of ~0.27±0.12 per near detector and ~0.22±0.10 per far detector during the operation of the first six detectors. While this background was negligible compared to the $\overline{\nu}_e$ rate in the near detectors, the rate in the far detectors was almost equal to that of the β-n background. To mitigate this background, the ^{241}Am-^{13}C sources present in ACU-B and ACU-C were removed from each of the far site detectors during the installation of the final two detectors in 2012. Removal of these sources reduced

the correlated background by a factor of ~3. The remaining sources each showed a ~50% decline in neutron emission rate during the first two years of operation. This decline was attributed to scintillator infiltration into the sources, which reduced the efficiency of (α,n) neutron production. Combined, the two effects reduced the background rate by a factor of ~6 for far detector data collected after the summer of 2012. For the entire data period presented here, the ^{241}Am-^{13}C background contamination in the $\overline{\nu}_e$ sample was 0.03% for the near detectors and 0.09% for the far detectors. A 45% uncertainty in the correlated background rate covered the range of variations between simulation and measurement obtained when comparing the regular and intense sources.

e. α-n Interaction Background The last minor correlated background resulted from (α,n) nuclear interactions. In these interactions, an α-particle, produced by natural radioactivity in the scintillator, fused with a nucleus in the detector materials, resulting in the emission of a neutron. ^{13}C$(\alpha,n)^{16}$O was the dominant process of this type, as determined from the composition of organic scintillator and the known cross-sections for (α,n) interactions. Details of modeling the ^{13}C$(\alpha,n)^{16}$O background are presented in [50].

Capture of the neutron emitted by ^{13}C$(\alpha,n)^{16}$O interactions is identical to the delayed signal from $\overline{\nu}_e$ interactions. The false prompt signal was not as obvious, and resulted from three different potential processes. In the first process, the neutron was ejected with sufficient energy such that successive collisions with protons generated enough scintillation light to mimic a prompt signal with $E_{\text{rec}} > 0.7$ MeV. For the second process, the energetic neutron collided inelastically with ^{12}C, leaving this nucleus in the first excited state, ^{12}C*(4.4 MeV). The nucleus would immediately de-excite via emission of a 4.4-MeV γ-ray, producing a prompt signal. In the third process, α-particles with energy greater than ~5 MeV would preferentially leave the ^{16}O in an excited state. The ^{16}O* would de-excite via emission of a γ-ray or an electron-positron pair.

The rate and energy of natural alpha activity was determined for each detector. Within the GdLS, the dominant alpha sources are the ^{238}U, ^{232}Th, and ^{227}Ac actinide decay chains. With chemical properties similar to Gd, these nuclides were introduced at trace levels during the scintillator doping process. Each actinide chain contains a polonium cascade decay, which generates a time-correlated pair of β-α or α-α interactions. The half-life of the delayed polonium α decay for each actinide chain is 164.3 μs, 0.3 μs, and 1.781 ms, respectively. The scintillator quenched the alpha from polonium decay, as discussed in Sec III D, producing a delayed signal with $E_{\text{rec}} \approx 1$ MeV. Given the low-energy of the delayed signal, it did not mimic a $\overline{\nu}_e$ interaction. Instead, the time-correlated signals were used to determine the α production rate for each of these actinide decay chains. Figure 30 shows the correlated prompt-delayed energy distributions for various time intervals corresponding to these Po cascade decays. A time interval of 1 to 3 μs revealed ^{212}Bi-^{212}Po decays from the ^{232}Th decay chain. An interval from 10 to 400 μs revealed ^{214}Bi-^{214}Po decays from the ^{238}U decay chain. A 1 to 4 ms interval showed ^{219}Rn-^{215}Po

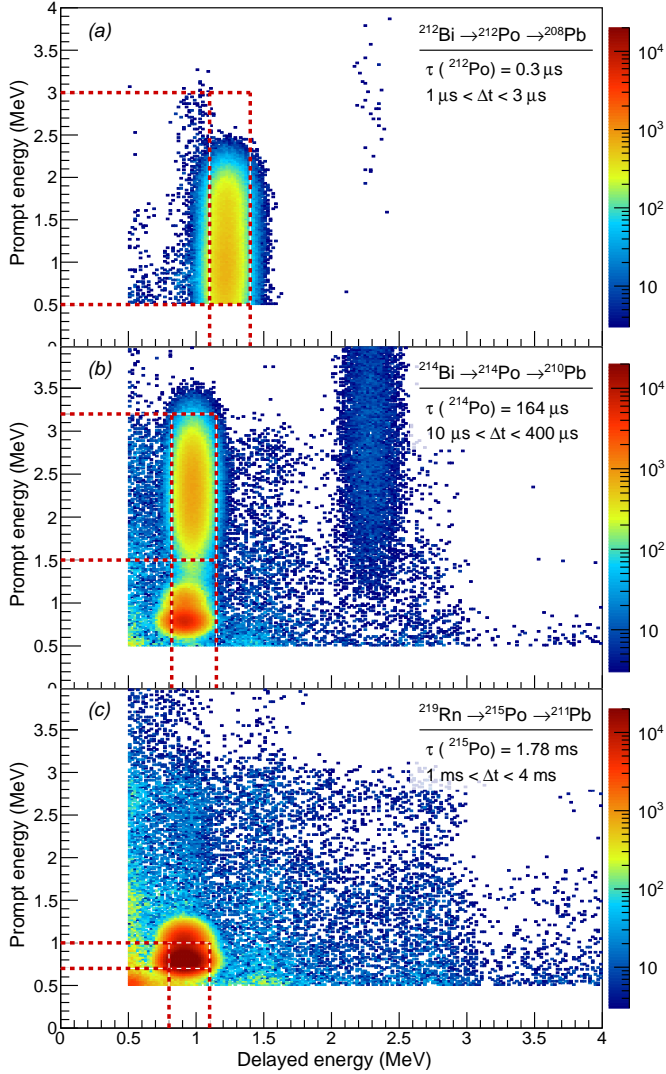decays from the ^{227}Ac decay chain. Assuming each chain

FIG. 30. The distributions of low-energy prompt versus delayed reconstructed energy for the time intervals (a) 1 μs to 3 μs, (b) 10 μs to 400 μs, and (c) 1 ms to 4 ms for all detectors combined. The distributions revealed time-correlated signal pairs from actinide contamination in the GdLS regions of each detector. While these interactions were not a background for $\bar{\nu}_e$ detection, the resulting estimates of actinide α-particle activity constrained potential background from subsequent ^{13}C(α,n)^{16}O interactions.

was in equilibrium with the observed Po cascades, the average decay rates of 0.009, 0.16 and 0.2 Bq were found for the ^{238}U, ^{232}Th, and ^{227}Ac chains within the GdLS region for the first two years of data. The measured rates were consistent among all eight detectors. A 40% decrease of the ^{212}Bi-^{212}Po rate and 9% decrease of the ^{219}Rn-^{215}Po rate were observed, consistent with the half-lives of ^{228}Th (1.9 yr) and ^{227}Ac (21.8 yr).

Monoenergetic 5.3 MeV α-particles were also emitted by

^{210}Po, a long-lived daughter of ^{222}Rn. These α-particles were visible as a peak at $E_{\rm rec} \simeq 0.5$ MeV in the energy spectrum of uncorrelated signals in each detector. The amplitude of these peaks determined a ^{210}Po α rate of 4 Hz for AD3-AD7, while larger rates of 8 to 10 Hz were found for AD1, AD2, and AD8. The distribution of reconstructed positions for these signals suggests that the ^{210}Po background was concentrated on the wall of the inner acrylic vessel. This observation agreed with previous experiments which reported ^{210}Po contamination on detector surfaces, with a variable amount of contamination dependent on the history of material exposure to ^{222}Rn [51].

A Geant4-based simulation was used to model the probability for ^{13}C(α,n)^{16}O interactions in the detector. Each α-particle was attenuated via interactions with the detector material, with the probability for an ^{13}C(α,n)^{16}O interaction determined using the JENDL tabulated cross-sections [52]. Table IV summarizes the estimated probability for a ^{13}C(α,n)^{16}O interaction to occur, per initial α decay for the various natural α sources. Probabilities of interaction to the ^{16}O ground state only, to the excited states, and the sum of the two are provided. The uncertainty in the simulated probability was determined from comparison with an alternate simulation which relied on EXFOR tabulated cross-sections [53] and a SRIM simulation of alpha attenuation [54].

TABLE IV. The simulated probability for a ^{13}C(α,n)^{16}O interaction to occur, per equilibrium decay of the natural actinide contaminants in the detectors. The separate probability for the interaction to occur to the ^{16}O ground state and the excited states, as well as the sum of the two, are given. The uncertainty in the probability $\sigma_{\rm tot}$ was determined from a comparison of simulation techniques.

α Source	$P_{\rm gnd}$ [10^{-8}]	$P_{\rm exc}$ [10^{-8}]	$P_{\rm tot}$ [10^{-8}]	$\sigma_{\rm tot}$ [%]
^{210}Po	5.26	0.49	5.75	7.2%
^{238}U	43.40	29.60	73.00	16.9%
^{232}Th	44.90	49.20	94.10	27.7%
^{227}Ac	47.20	61.80	109.00	25.9%

The same simulation was also used to estimate the reconstructed energy spectra for prompt signals from ^{13}C(α,n)^{16}O interactions, as presented in Figure 31. Energetic neutrons produced a broad peak from proton recoils below 4 MeV, and a small peak near 5 MeV from inelastic scattering on ^{12}C. Higher-energy α-particles increasingly populated the excited states of ^{16}O, resulting in a broad peak from 5 MeV to 8 MeV from ^{16}O* de-excitation. Uncertainties in the spectra, although substantial, were safely ignored due to the insignificant contribution of this background to the $\bar{\nu}_e$ sample. The rate of correlated (α,n) background was estimated from the product of the measured α activity, the simulated probabilities of ^{13}C(α,n)^{16}O interaction, and the modeled efficiency for the corresponding signals to satisfy the $\bar{\nu}_e$ signal selection. The contamination of this background in the $\bar{\nu}_e$ candidate sample was found to be negligible, 0.07% for the far detectors and 0.01% for the near detectors. A conservative $\sim$50% total uncertainty in the rate of this background resulted from a combination of uncertainties in Po
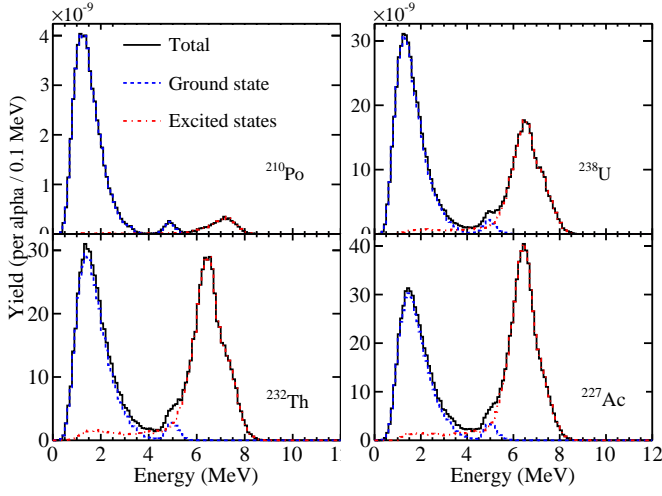
FIG. 31. Simulation of energy spectra of the prompt signals for the $^{13}C(\alpha,n)^{16}O$ background, for each of the primary sources of natural α activity in the detectors. Energetic neutrons produced a broad peak from proton recoils below 4 MeV, and a small peak near 5 MeV from inelastic scattering on ^{12}C. Higher-energy α-particles increasingly populated the excited states of ^{16}O, resulting in a broad peak from 5 MeV to 8 MeV from $^{16}O^*$ de-excitation.

cascade selection, assumptions of actinide chain equilibrium, and simulation of $^{13}C(\alpha,n)^{16}O$ interactions.

f. High-Multiplicity Background In the search for a pair of prompt and delayed signals consistent with $\overline{\nu}_e$ inverse beta decay, occasionally three or more signals were found within the relevant time window. Such signal sets, referred to as having multiplicity ≥ 3, were generally from the pile-up of actual $\overline{\nu}_e$ interactions with additional uncorrelated signals from natural radioactivity. Classification of each signal as a potential prompt or delayed interaction was ambiguous in these cases. Rejection of signal sets with multiplicity ≥ 3 removed all concerns about this ambiguity, while resulting in an insignificant loss of efficiency. Two different techniques were implemented to reject these ambiguous signals.

For selection A, a $\overline{\nu}_e$ candidate was rejected if one or more additional signals with reconstructed energy >0.7 MeV occurred within 200 μs before the prompt signal, or within 200 μs following the delayed signal. The requirement for selection B differed slightly. Each delayed signal was required to have one and only one signal with energy >0.7 MeV in the preceding 400 μs. It was also required to have no other signal which satisfied the delayed energy selection 6 MeV$<$ E_{rec} <12 MeV in the 200 μs following the delayed signal. This approach had an efficiency which was independent of the time between the prompt and delayed signals, and also avoided unwanted correlations in the estimation of the muon and multiplicity veto efficiencies.

Both methods effectively resolved signal ambiguities, while maintaining a signal acceptance efficiency of $\sim 97.5\%$. The efficiency was estimated in a fashion similar to that used for the accidental background, by calculating the probability for an uncorrelated signal to randomly occur in close time proximity to a true $\overline{\nu}_e$ interaction. For selection A, the

efficiency was

$$\epsilon_m^A = e^{-R_p \Delta t} \epsilon_{mid} \epsilon_{post}, \tag{30}$$

where R_p was the rate of prompt-like signals defined in the discussion of the accidental background, and Δt was 200 μs. The probability for an uncorrelated signal to fall between the true prompt and delayed signals, ϵ_{mid}, varied with the time between these signals. On average it was

$$\epsilon_{mid} = \int_0^{\Delta t} e^{-R_p t} f(t)\,dt \cong 1 - R_p \bar{t}_c, \tag{31}$$

where $f(t)$ was the distribution of times between prompt and delayed signals within 200 μs, and $\bar{t}_c$ was the mean of this distribution. At lowest order, the probability for an uncorrelated signal to occur after the delayed signal, ϵ_{post}, was simply $\exp(-R_p \Delta t)$. The probability that the muon veto truncated the time window after the candidate signal, reducing the probability for detecting uncorrelated signals after the $\overline{\nu}_e$ interaction, was not negligible. A correction for this time-truncation was incorporated into ϵ_{post}. As a result, for a time segment t_s^i between vetoed periods,

$$\epsilon_{post}^i = \begin{cases} \left(1 - \frac{\Delta t}{t_s^i}\right) e^{-R_p \Delta t} + \frac{1 - e^{-R_p \Delta t}}{R_p t_s^i}, & \text{for } t_s^i \geq \Delta t, \\ \frac{1 - e^{-R_p \Delta t}}{R_p t_s^i}, & \text{for } t_s^i < \Delta t. \end{cases} \tag{32}$$

Given the correlation of the multiplicity selection and muon veto, the combined $\overline{\nu}_e$ selection efficiency was calculated from a time-weighted average of the multiplicity efficiency over the time segments t_s^i between muon-vetoed periods,

$$\epsilon_\mu \bar{\epsilon}_m^A = \left(\sum_i \epsilon_m^i t_s^i \right) / t_{DAQ}, \tag{33}$$

where t_{DAQ} was the total DAQ livetime before application of the muon veto. The average efficiency of the multiplicity veto could be determined from comparison of $\epsilon_\mu \bar{\epsilon}_m^A$ with ϵ_μ calculated using Eq. 24. Uncertainty in $f(t)$ resulted in a systematic uncertainty of 0.02% in $\bar{\epsilon}_m^A$, correlated between detectors. Similarity of the observed $f(t)$ between detectors constrained potential uncorrelated variations in efficiency to $<0.01\%$.

Estimation of the multiplicity efficiency for selection B was trivial by design. The efficiency was calculated from the expression

$$\epsilon_m^B = e^{-2R_p \Delta t} e^{-R_d \Delta t}. \tag{34}$$

The probability of simultaneous multiplicity and muon vetos was reduced to a negligible level, given the very low rate of delayed-like signals. Uncertainty in ϵ_m^B was insignificant.

C. Summary of Antineutrino Selection

1. Detection Efficiencies

Table V summarizes the efficiencies for detection of $\overline{\nu}_e$ inverse beta decay in the GdLS target of each detector. The

combined efficiency was estimated to be 80.6%. Neutrons which did not capture on Gd, as well as those n-Gd captures which failed to produce signals with $E_{rec} > 6$ MeV, had the greatest impact on the efficiency. The number of target protons and multiplicity cut efficiencies varied slightly between detectors, and their precisely measured differences are provided in Table I and Table VI.

TABLE V. A summary of the estimated efficiencies and their relative uncertainties for detection of $\overline{\nu}_e$ inverse beta decay in the GdLS target region of each antineutrino detector. The values are provided for selection A, but differ negligibly for selection B. The number of target protons and multiplicity cut efficiencies varied slightly between detectors, and their precisely measured differences are provided in Table I and Table VI. The estimated uncertainties are divided into a correlated component, which was common for all detectors, and an uncorrelated component, which captured potential variations in efficiency between detectors. This latter component was relevant for the measurement of neutrino oscillation.

	Efficiency	Correlated	Uncorrelated
Target protons	-	0.92%	0.03%
Flasher cut	99.98%	0.01%	0.01%
Delayed energy cut	92.7%	0.97%	0.08%
Prompt energy cut	99.8%	0.10%	0.01%
Multiplicity cut		0.02%	0.01%
Capture time cut	98.7%	0.12%	0.01%
Gd capture fraction	84.2%	0.95%	0.10%
Spill-in	104.9%	1.00%	0.02%
Livetime	-	0.002%	0.01%
Combined	80.6%	1.93%	0.13%

Uncertainties in the detection efficiencies were divided into correlated components, which were common for all detectors, and uncorrelated components, which captured potential variations in efficiency between detectors. The total correlated relative uncertainty in efficiency was estimated to be 1.93%. Spill-in neutrons, generated by $\overline{\nu}_e$ interactions outside the GdLS target but which diffused into the target and captured on Gd, caused the largest correlated uncertainty in detection efficiency. Absolute uncertainties in the fraction of neutrons in the GdLS target which captured on Gd, as well as in the fraction of n-Gd captures which produced signals with $E_{rec} < 6$ MeV, were also significant. A detailed assessment of correlated uncertainties is given in [55].

The absolute efficiencies and their correlated uncertainties canceled when comparing the ratio of signals in the far versus near detectors, as presented in Eq. 4. Therefore, only the uncorrelated uncertainties were relevant for the far versus near detector measurement of neutrino oscillation. Variations in efficiency between detectors were estimated to be 0.13%. The most significant variation in efficiency came from potential differences in the fraction of neutrons which captured on Gd, as constrained by comparisons of the capture time distributions between detectors.

The Daya Bay experiment was designed to minimize potential variations in efficiency between detectors, but the actual detectors exceeded the design goal. Given this achievement, it was important to have an independent method

to verify the low 0.13% estimate of uncorrelated variation between detector efficiency. Comparison of the $\overline{\nu}_e$ rates observed in detectors located side-by-side within the same experimental hall provided a direct test of the estimated variations between detector efficiency. The results of these tests are discussed in the following section.

2. Final Antineutrino Sample

Table VI summarizes the antineutrino candidate data sample. Refer to Table II for an overview of the selection criteria. More than 2.5×10^6 $\overline{\nu}_e$ inverse beta decay interactions were identified using the eight detectors. Backgrounds were estimated to contribute 1.8% to the sample from EH1, 1.5% to EH2, and 2.0% to EH3, primarily from uncorrelated accidentals. Uncertainty in the background was 0.2%, 0.1%, and 0.1% for the three experimental halls, and was dominated by the contribution from β-n decay of ^{9}Li and ^{8}He. For each detector i, the observed rate of $\overline{\nu}_e$ interactions was

$$R_{\overline{\nu}}^i = \frac{N_{cand}^i}{t_{DAQ}^i \, \epsilon_\mu^i \, \epsilon_m^i} - R_{bkg}^i, \qquad (35)$$

where N_{cand} was the number of $\overline{\nu}_e$ candidates selected, t_{live} was the DAQ operation live time, ϵ_μ was the reduced signal efficiency from live time rejected by the muon veto, ϵ_m was the same for the multiplicity veto, and R_{bkg} was the total background rate. These rates have not been corrected for the absolute selection efficiencies shown in Table V, nor for the slight differences in the number of protons, ΔN_p, in the target region of each detector.

Figure 32 compares the $\overline{\nu}_e$ rates obtained using selection A with those from selection B. The consistency of the two results served as an independent cross-check of the $\overline{\nu}_e$ selection process. 10% of the candidates differed between the two selections. For the near detectors, differences in the muon vetoes caused most of the discrepant candidate signals. For the far detectors, discrepancies were primarily a result of the different multiplicity veto criteria.

The rates observed by detectors located side-by-side within the same experimental hall were used to independently assess potential variations in $\overline{\nu}_e$ efficiency between detectors. Figure 33 compares the observed rates for detectors within the same hall. Slight differences in distances from the reactors and ΔN_p predict $\lesssim 1\%$ deviations between detectors. Comparisons for the detectors in EH2 and EH3 are shown separately for the 6-AD and 8-AD operation periods. The consistency of the detected rates, relative to the slight differences in predictions, provided independent confirmation of the estimated 0.13% variation in efficiency between detectors.

Potential variation in performance between detectors was assessed by comparing the capture time, prompt energy, and delayed energy distributions for the selected $\overline{\nu}_e$ candidates for side-by-side detectors. Figures 17, 34, and 35 compare these three distributions for all eight detectors. For spectral comparisons, simple ratios of the distributions for AD2 to

TABLE VI. Summary of the $\overline{\nu}_e$ inverse beta decay interaction candidate sample. Results obtained using both selection A and selection B are provided for comparison (Selection criteria are given in TableII). The number of signals selected as $\overline{\nu}_e$ inverse beta decay candidates, DAQ livetime, efficiency lost to vetoes, and estimated background rates are listed for each antineutrino detector. The background-subtracted rates of $\overline{\nu}_e$ interactions for each detector were estimated from these quantities. All rates are corrected for the detector-dependent loss of live time from the muon and multiplicity vetoes, expressed as the efficiencies ϵ_μ and ϵ_{m}. Slight differences in the number of protons in each target region, ΔN_{p}, relative to AD1 in EH1 are also provided.

|	EH1		EH2		EH3			
	AD1	AD2	AD3	AD8	AD4	AD5	AD6	AD7
ΔN_{p} [%]	0.00 ± 0.03	0.13 ± 0.03	-0.25 ± 0.03	0.02 ± 0.03	-0.12 ± 0.03	0.24 ± 0.03	-0.25 ± 0.03	-0.05 ± 0.03
	Selection A							
$\overline{\nu}_e$ candidates	597616	606349	567196	466013	80479	80742	80067	66862
DAQ live time [days]	1117.178	1117.178	1114.337	924.933	1106.915	1106.915	1106.915	917.417
ϵ_μ	0.8255	0.8221	0.8573	0.8571	0.9824	0.9823	0.9821	0.9826
$\overline{\epsilon}_{\mathrm{m}}$	0.9744	0.9747	0.9757	0.9757	0.9759	0.9758	0.9756	0.9758
Accidentals [day^{-1}]	8.46 ± 0.09	8.46 ± 0.09	6.29 ± 0.06	6.18 ± 0.06	1.27 ± 0.01	1.19 ± 0.01	1.20 ± 0.01	0.98 ± 0.01
Fast neutron [AD^{-1} day^{-1}]	0.79 ± 0.10		0.57 ± 0.07		0.05 ± 0.01			
^{9}Li,^{8}He [AD^{-1} day^{-1}]	2.46 ± 1.06		1.72 ± 0.77		0.15 ± 0.06			
^{241}Am-^{13}C, 6-AD [day^{-1}]	0.27 ± 0.12	0.25 ± 0.11	0.28 ± 0.13		0.22 ± 0.10	0.21 ± 0.10	0.21 ± 0.10	
^{241}Am-^{13}C, 8-AD [day^{-1}]	0.15 ± 0.07	0.16 ± 0.07	0.13 ± 0.06	0.15 ± 0.07	0.04 ± 0.02	0.03 ± 0.02	0.03 ± 0.02	0.05 ± 0.02
^{13}C$(\alpha, \mathrm{n})^{16}$O [day^{-1}]	0.08 ± 0.04	0.07 ± 0.04	0.05 ± 0.03	0.07 ± 0.04	0.05 ± 0.03	0.05 ± 0.03	0.05 ± 0.03	0.05 ± 0.03
$\overline{\nu}_e$ rate, $R_{\overline{\nu}}$ [day^{-1}]	653.03 ± 1.37	665.42 ± 1.38	599.71 ± 1.12	593.82 ± 1.18	74.25 ± 0.28	74.60 ± 0.28	73.98 ± 0.28	74.73 ± 0.30
	Selection B							
$\overline{\nu}_e$ candidates	594737	603092	562681	462129	80508	80769	80112	67018
DAQ live time [days]	1117.162	1117.162	1114.334	924.930	1106.898	1106.898	1106.898	917.401
ϵ_μ	0.8210	0.8178	0.8502	0.8496	0.9824	0.9821	0.9820	0.9825
ϵ_{m}	0.9768	0.9773	0.9782	0.9781	0.9783	0.9783	0.9781	0.9784
Accidentals [day^{-1}]	7.99 ± 0.01	7.88 ± 0.01	5.94 ± 0.01	5.81 ± 0.01	1.20 ± 0.00	1.13 ± 0.00	1.14 ± 0.00	0.92 ± 0.00
Fast neutron [AD^{-1} day^{-1}]	0.84 ± 0.08		0.64 ± 0.06		0.05 ± 0.01			
^{9}Li,^{8}He [AD^{-1} day^{-1}]	2.71 ± 0.90		1.91 ± 0.73		0.22 ± 0.07			
^{241}Am-^{13}C, 6-AD [day^{-1}]	0.26 ± 0.12	0.25 ± 0.11	0.28 ± 0.12		0.22 ± 0.10	0.21 ± 0.09	0.21 ± 0.09	
^{241}Am-^{13}C, 8-AD [day^{-1}]	0.15 ± 0.07	0.15 ± 0.07	0.13 ± 0.06	0.15 ± 0.07	0.04 ± 0.02	0.03 ± 0.02	0.04 ± 0.02	0.05 ± 0.02
^{13}C$(\alpha, \mathrm{n})^{16}$O [day^{-1}]	0.08 ± 0.04	0.07 ± 0.04	0.05 ± 0.03	0.07 ± 0.04	0.05 ± 0.03	0.05 ± 0.03	0.05 ± 0.03	0.05 ± 0.03
$\overline{\nu}_e$ rate, $R_{\overline{\nu}}$ [day^{-1}]	651.99 ± 1.25	663.74 ± 1.26	598.47 ± 1.09	592.67 ± 1.15	74.08 ± 0.28	74.43 ± 0.28	73.83 ± 0.28	74.70 ± 0.30
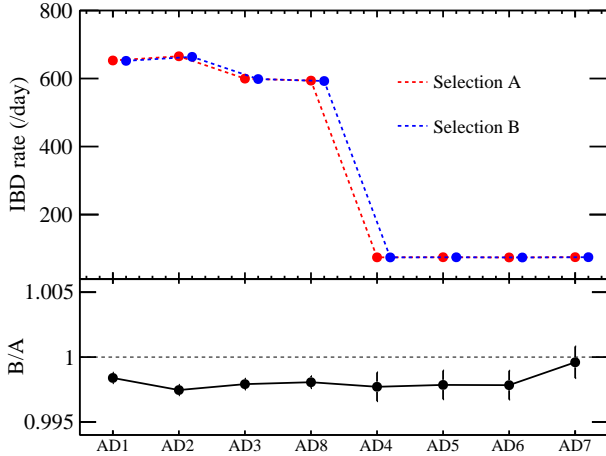
FIG. 32. (*Top*) The rates of $\overline{\nu}_e$ inverse beta decay observed in each antineutrino detector, for both selection A and selection B. (*Bottom*) The rates obtained by selection B were ~0.2% lower than those of selection A, demonstrating a difference in absolute selection efficiency within expectations. The ratio of the far versus near detector rates are consistent for the two selections, considering the statistical uncertainty from candidate signals uncommon between the two samples.

AD1 and AD8 to AD3 are shown for the near detectors. For the far hall, the distribution for each AD was divided by the site average. No significant deviations in the distributions for detectors within the same experimental hall were found.

V. OSCILLATION ANALYSIS

The $\overline{\nu}_e$ inverse beta decay interactions observed with the eight detectors were used to measure the oscillation of neutrino flavor. Comparison of the rates observed in the three experimental halls revealed $\overline{\nu}_e$ disappearance between the near and far detectors. The amplitude of the disappearance determined the value of the mixing angle θ_{13}. The energy-dependence of $\overline{\nu}_e$ disappearance distorted the energy spectra of the prompt positrons observed in the far detectors relative to the near detectors. The neutrino mass-squared difference Δm_{32}^2 was measured from this spectral distortion. The details of the measurement of neutrino oscillation are presented in this section.

A. Antineutrino Disappearance

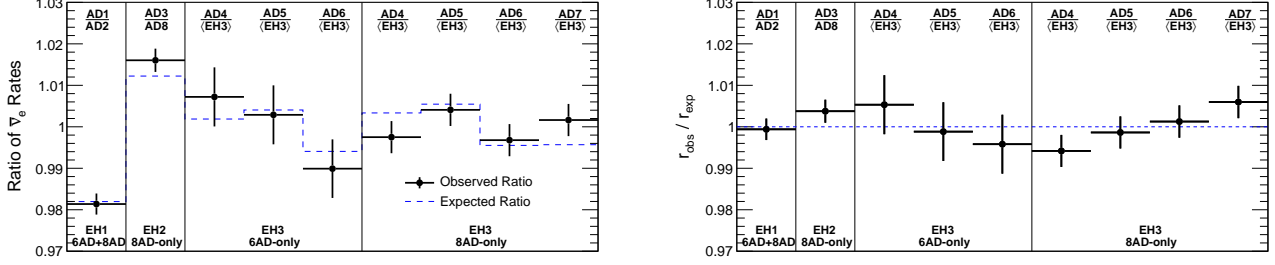Before discussing detailed statistical methods, it is useful to examine a simple ratio of the signal observed by the

FIG. 33. (*Left*) Ratios of the $\overline{\nu}_e$ interaction rates observed by detectors within the same experimental hall, $r_{\rm obs}$ (black points). The ratio of the rate in AD1 to that of AD2 is shown for EH1 for the entire data period. For the period following installation of AD8 in EH2, the ratio of AD3 to AD8 is provided. For EH3, the ratio of the rate in each detector relative to the site average is given separately for the period before and after installation of AD7. Slight differences in the distances of each detector relative to each reactor as well as small variations in detector target mass $\Delta N_{\rm p}$ predicted minor deviations in these ratios, $r_{\rm exp}$ (blue dashed line). The uncertainties are dominated by statistics and the estimated 0.13% variation in efficiency between detectors. The consistency of the side-by-side detector rates confirmed the stringent limits on this latter systematic uncertainty. (*Right*) The same figure, expressed as the double ratio $r_{\rm obs}/r_{\rm exp}$.
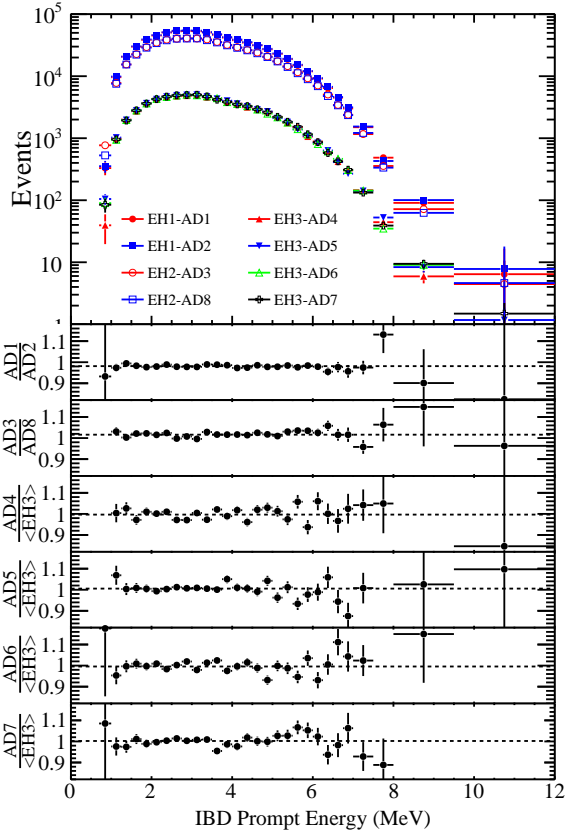

FIG. 34. (*Top*) Distributions of the reconstructed prompt energy for the selected $\overline{\nu}_e$ candidates in each of the eight detectors. (*Bottom*) The ratio of the distributions for detectors within the same experimental hall showed no significant deviations between detectors.
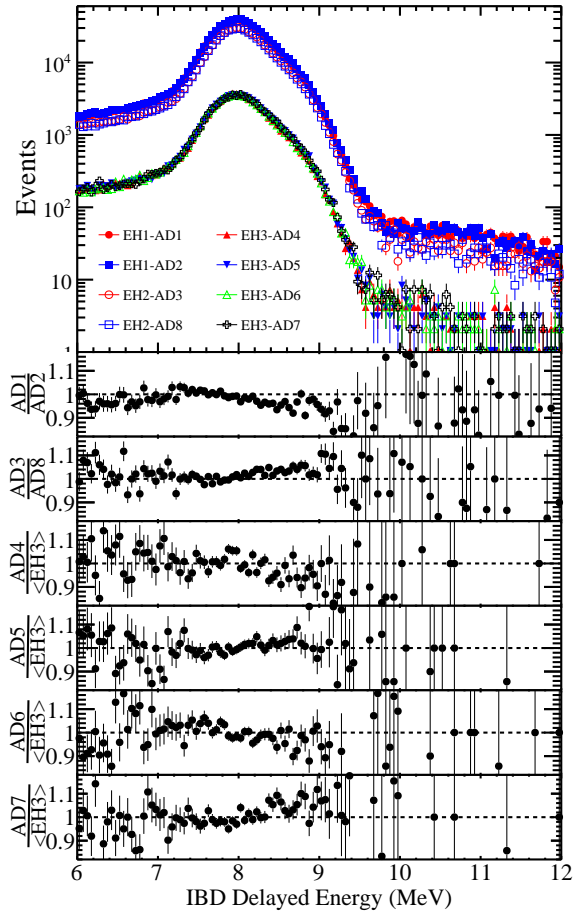

FIG. 35. (*Top*) Distributions of the reconstructed delayed energy for the selected $\overline{\nu}_e$ candidates in each of the eight detectors. (*Bottom*) The ratio of the distributions for detectors within the same experimental hall showed no significant deviations between detectors; the slight slopes in the ratios are consistent with the $\lesssim 0.2\%$ relative differences in the energy scale among the detectors.

far detectors versus the near detectors. After correcting for differences in detector exposure, any deficit in this ratio would be evidence of $\overline{\nu}_e$ disappearance. This example demonstrates the robustness of the observation of $\overline{\nu}_e$ disappearance due

to θ_{13}, independent of the statistical models that will be presented.

The estimated number of $\bar{\nu}_e$ interactions at the far site was determined from the sum of the background-subtracted $\bar{\nu}_e$ rate $R_{\bar{\nu}}^i$ times the livetime t_{live}^i of each far detector i,

$$\widetilde{N}_{\text{obs}}^{\text{far}} = \sum_{i}^{\text{FarADs}} R_{\bar{\nu}}^i t_{\text{live}}^i. \tag{36}$$

The $\bar{\nu}_e$ rates and livetimes were taken from Table VI. The estimated numbers for each near site, $\widetilde{N}_{\text{obs}}^{\text{EH1}}$ and $\widetilde{N}_{\text{obs}}^{\text{EH2}}$, are defined in the same fashion as given in Eq. 36. Assuming no oscillation, the $\bar{\nu}_e$ signal at the far site was predicted by a suitable weighted combination of the signals observed at the two near sites,

$$\widetilde{N}_{\text{exp}}^{\text{far}} = w^{\text{EH1}} \widetilde{N}_{\text{obs}}^{\text{EH1}} + w^{\text{EH2}} \widetilde{N}_{\text{obs}}^{\text{EH2}}. \tag{37}$$

The weights w^{EH1} and w^{EH2} are defined such that $\widetilde{N}_{\text{exp}}^{\text{far}}$ consisted of $\bar{\nu}_e$'s from the Daya Bay and Ling Ao reactors in roughly the same proportion as determined for the far site.

TABLE VII. Estimated relative contribution of the two Daya Bay reactors and four Ling Ao reactors to the $\bar{\nu}_e$ signal in each of the experimental halls for the combined six detector and eight detector data periods. The values are normalized relative to the total estimated signal in EH3.

	Relative $\bar{\nu}_e$ Signal, f_l^k		
Reactors	EH1	EH2	EH3
Daya Bay	3.5022	0.2338	0.2423
Ling Ao	0.9255	3.4333	0.7577

Table VII gives the estimated relative $\bar{\nu}_e$ signal contribution f_l^k of each set of reactors l to the detectors in each hall k, including hall-dependent differences in livetime, efficiency, and the number of target protons. Variations in the contributions were primarily due to the distances of each reactor to each detector, as given in Table I. Differences in the fluxes from each reactor were a minor effect given the common average thermal power of the six reactors during this data period, as listed in Table I. Minor differences in the target mass of each detector, ΔN_p in Table VI, were included in this calculation. The weights that sample the flux of the two sets of reactors in equal proportion to the far detectors are simply

$$w^{\text{EH1}} = \frac{f_{\text{D}}^{\text{far}} f_{\text{L}}^{\text{EH2}} - f_{\text{L}}^{\text{far}} f_{\text{D}}^{\text{EH2}}}{f_{\text{D}}^{\text{EH1}} f_{\text{L}}^{\text{EH2}} - f_{\text{L}}^{\text{EH1}} f_{\text{D}}^{\text{EH2}}}, \tag{38}$$

$$w^{\text{EH2}} = \frac{f_{\text{L}}^{\text{far}} f_{\text{D}}^{\text{EH1}} - f_{\text{D}}^{\text{far}} f_{\text{L}}^{\text{EH1}}}{f_{\text{L}}^{\text{EH2}} f_{\text{D}}^{\text{EH1}} - f_{\text{D}}^{\text{EH2}} f_{\text{L}}^{\text{EH1}}}. \tag{39}$$

Using the relative signal contributions provided in Table VII, $w^{\text{EH1}} = 0.05545$ and $w^{\text{EH2}} = 0.2057$. This result was independent of the specific model of reactor $\bar{\nu}_e$ emission. In fact, an equivalent result can be obtained using the average thermal power of each reactor, given in Table I, as a proxy for the relative $\bar{\nu}_e$ flux.

From this simple analytic method, a clear $\bar{\nu}_e$ rate deficit was observed in the far detectors,

$$R = \frac{\widetilde{N}_{\text{obs}}^{\text{far}}}{\widetilde{N}_{\text{exp}}^{\text{far}}} = 0.949 \pm 0.002(\text{stat.}) \pm 0.002(\text{syst.}), \tag{40}$$

for the combined six detector and eight detector data periods. The statistical uncertainty was primarily determined from the observed signal rate in the far detectors. Uncertainty from the reactor $\bar{\nu}_e$ flux was almost completely canceled in this ratio. An uncorrelated 0.9% uncertainty in the estimated flux of each reactor resulted in $\lesssim 0.1\%$ uncertainty in R, as demonstrated by simple error propagation. The β-n background and relative variations in detector efficiency contributed the most significant systematic uncertainties.

The value of θ_{13} can be estimated from the observed rate deficit using a simple calculation. The rate deficit can be expressed as

$$R = \frac{N_{\text{pred}}^{\text{far}}}{w^{\text{EH1}} N_{\text{pred}}^{\text{EH1}} + w^{\text{EH2}} N_{\text{pred}}^{\text{EH2}}}, \tag{41}$$

where N_{pred}^k is a prediction for the number of $\bar{\nu}_e$ interactions in each hall k as a function of θ_{13}. The $\bar{\nu}_e$ signal can be rewritten as the product of the $\bar{\nu}_e$ signal assuming no oscillation and the mean survival probability $\bar{P}_{\text{sur}}^k$,

$$N_{\text{pred}}^k = N_{\text{no osc}}^k \bar{P}_{\text{sur}}^k. \tag{42}$$

$\bar{P}_{\text{sur}}^k$ is approximately linear in $\sin^2 2\theta_{13}$, as shown by Eq. 2. For short-baseline reactor measurements,

$$\bar{P}_{\text{sur}}^k = 1 - \eta^k \sin^2 2\theta_{13} + O(10^{-5}), \tag{43}$$

given that θ_{13} is small. The terms η^k were determined to be 0.180, 0.206, and 0.789 for EH1, EH2, and EH3 respectively. For this calculation, values for $\sin^2 2\theta_{12}$ and Δm_{21}^2 were taken from [14]. A value of $\Delta m_{32}^2 = 2.43 \times 10^{-3}$ eV^2 was also assumed, based on the error-weighted average of measurements by the T2K and MINOS experiments [14]. Expressing R as in terms of $\sin^2 2\theta_{13}$ gives

$$R = \frac{1 - \eta^{\text{far}} \sin^2 2\theta_{13}}{1 - \eta^{\text{near}} \sin^2 2\theta_{13}}, \tag{44}$$

where

$$\eta^{\text{near}} = w^{\text{EH1}} \beta^{\text{EH1}} \eta^{\text{EH1}} + w^{\text{EH2}} \beta^{\text{EH2}} \eta^{\text{EH2}}, \tag{45}$$

and

$$\beta^k = \frac{N_{\text{no osc}}^k}{N_{\text{no osc}}^{\text{far}}} = \frac{(f_{\text{D}}^k + f_{\text{L}}^k)}{(f_{\text{D}}^{\text{far}} + f_{\text{L}}^{\text{far}})}. \tag{46}$$

Eq. 44 is interpreted as a numerator which gives the mean $\bar{\nu}_e$ survival probability at the far site, and a denominator which accounts for oscillation present in the near site measurements. Consequently,

$$\sin^2 2\theta_{13} = \frac{1 - R}{\eta^{\text{far}} - R \eta^{\text{near}}}, \tag{47}$$

$$= 0.085 \pm 0.003(\text{stat.}) \pm 0.003(\text{syst.}) \tag{48}$$

was obtained from this simple calculation.

B. Statistical Methods

Standard frequentist statistical techniques were applied to the measurement, providing (i) best estimates of θ_{13} and Δm_{32}^2, (ii) confidence intervals for these parameters, and (iii) a goodness-of-fit test for the observations relative to the three-flavor neutrino oscillation model. Five independent statistical calculations were performed, with each relying on complementary approaches. The conceptual details, approach to modeling of systematic uncertainties, and validation of the calculations are discussed in this section.

All methods defined a χ^2 expression for comparison of the observation to prediction. The observation consisted of the reconstructed energy of the prompt e^+ interaction candidates in each detector. In each case, N_{ik}^{obs} was the observed number of candidates in the k-th bin of the prompt energy spectrum from the i-th detector, while N_{ik}^{exp} was the prediction. The observed and expected counts per energy bin for all detectors can be expressed as the vectors $\boldsymbol{N}^{\mathrm{obs}}$ and $\boldsymbol{N}^{\mathrm{exp}}$. The prediction $\boldsymbol{N}^{\mathrm{exp}}$ was a function of the neutrino oscillation parameters θ_{13} and Δm_{32}^2.

Definitions of the χ^2 statistics differed primarily based on how additional model parameters and systematic uncertainties were incorporated into the calculation. In the *profile* approach, additional systematic parameters were incorporated into the prediction. The values of these nuisance parameters were profiled; that is, their value was allowed to vary during minimization of the χ^2. These nuisance parameters were described using the vector $\boldsymbol{\nu}$, following the notation of Sec. 38 of [14]. A systematic term, χ_{syst}^2, was added to the original χ^2 test statistic, now labeled χ_{stat}^2, to obtain

$$\chi_{\mathrm{prof}}^2(\theta_{13}, \Delta m_{32}^2, \boldsymbol{\nu}) = \\ \chi_{\mathrm{stat}}^2(\theta_{13}, \Delta m_{32}^2, \boldsymbol{\nu}) + \chi_{\mathrm{syst}}^2(\boldsymbol{\nu}). \quad (49)$$

The term χ_{syst}^2 penalized the total χ_{prof}^2 based on deviations of the systematic nuisance parameters from their expected values. For the analyses discussed here, either a Poisson maximum likelihood estimator (see Eq. 38.16 of [14]) or a standard Pearson χ^2 were used for χ_{stat}^2.

In an alternate *covariance* approach, the impact of systematic variations are integrated into the calculation,

$$\chi_{\mathrm{cov}}^2(\theta_{13}, \Delta m_{32}^2) = \\ \left(\boldsymbol{N}^{\mathrm{obs}} - \boldsymbol{N}^{\mathrm{exp}}\right)^T V^{-1} \left(\boldsymbol{N}^{\mathrm{obs}} - \boldsymbol{N}^{\mathrm{exp}}\right). \quad (50)$$

The covariance matrix V includes both statistical and systematic components,

$$V = V_{\mathrm{stat}} + V_{\mathrm{syst}}, \quad (51)$$

where V_{syst} accounted for the correlated variation between different energy bins and detectors within the expected deviations of the systematic parameters. This approach is mathematically equivalent to the profiling approach for the simple case of systematic uncertainties which are linear in character, and has the added benefit of significantly faster

calculation. Dependence of the covariance matrix V on the parameters, in particular θ_{13} and Δm_{32}^2, was also included. Between these two extremes are hybrid calculations where some systematic parameters are profiled while others are modeled in the covariance.

1. Modeling Systematic Uncertainties

Table VIII summarizes the systematic components incorporated into the prediction of $\boldsymbol{N}^{\mathrm{exp}}$.

a. Three-flavor parameters There was a minor impact on the $\overline{\nu}_e$ survival probability at the far detectors due to the value of the solar and long-baseline reactor oscillation parameters, as shown in Eq. 3. We adopted the best estimates of $\sin^2 2\theta_{12} = 0.846 \pm 0.021$ and $\Delta m_{21}^2 = (7.53 \pm 0.18) \times 10^{-5}$ eV^2 according to [14].

b. Reactor $\overline{\nu}_e$ Flux The far versus near detector measurement of oscillation was designed to be largely insensitive to the model of reactor $\overline{\nu}_e$ emission. Still, a nominal prediction of the $\overline{\nu}_e$ emission was used to assess the residual uncertainty not canceled by the far versus near measurement. A brief summary of the model and uncertainties are presented here, while a detailed description is given in [55].

The emission or $\overline{\nu}_e$ from each reactor was estimated as

$$\frac{d^2 R_\nu(E_\nu, t)}{dE_\nu dt} = \frac{W_{\mathrm{th}}(t)}{\langle e(t) \rangle} \sum_i^{\mathrm{isotope}} f_i(t) S_i(E_\nu) c_{\mathrm{ne},i}(E_\nu, t) \\ + S_{\mathrm{SNF}}(E_\nu, t), \quad (52)$$

with the following description for each term:

- $W_{\mathrm{th}}(t)$: The thermal power of the reactor core as a function of time t. These data were obtained at hourly intervals through collaboration with the reactor company. A systematic uncertainty of 0.5% was attributed to these data [56, 60], and assumed to be uncorrelated between reactors.

- $f_i(t)$: The fraction of nuclear fissions attributed to the parent isotope i in each reactor. The four parent isotopes of relevance were ^{235}U, ^{238}U, ^{239}Pu, and ^{241}Pu. These data were also obtained through agreement with the reactor company, and validated using an independent simulation of the reactors. An uncertainty of 5% was assumed, uncorrelated between reactors, but with a correlation among isotopes taken from [56].

- $\langle e(t) \rangle = \sum_j f_j(t) e_j$: The mean thermal energy released per fission. The energy released e_j per fission of parent j were taken from [57]. Uncertainty was <0.2% and correlated between reactors.

- $S_i(E_\nu)$: The estimated $\overline{\nu}_e$ emission versus energy per fission of parent isotope i. The predictions by Huber [58] for ^{235}U, ^{239}Pu, and ^{241}Pu, and the prediction for ^{238}U by Mueller [59] were used. Uncertainties as described in these references were adopted, and taken as correlated between reactors.

TABLE VIII. Summary of systematic uncertainties considered in the analysis of $\overline{\nu}_e$ oscillation.

Source	Uncertainty	Correlation
Reactor antineutrino flux		
Actinide fission fractions	5%	Correlation between isotopes from Ref. [56], correlated among all reactors
Average energy per fission	Uncertainties from Ref. [57]	Correlated among all reactors
$\overline{\nu}_e$ flux per actinide fission	Uncorrelated uncertainties from Huber+Mueller Model [58, 59]	Correlated among all reactors
Non-equilibrium $\overline{\nu}_e$ emission	30% of predicted contribution	Uncorrelated among all reactors
Spent nuclear fuel	100% of predicted contribution	Uncorrelated among all reactors
Reactor power	0.5%	Uncorrelated among all reactors
Detector response model		
Absolute energy scale (non-linearity)	<1%, constrained by calibration data	Correlated among all detectors
Relative energy scale	0.2%	Uncorrelated among all detectors
Detection efficiency	0.13%. See Tab. VI for the breakdown.	Uncorrelated among all detectors, partial correlation with relative energy scale
Detection efficiency and relative energy scale correlation coefficient	0.54	–
IAV thickness	4% (0.1%) of signal for energies below (above) 1.25 MeV	Uncorrelated among all detectors
Energy resolution	Negligible	Correlated among all detectors
Background prediction	*(Uncert.'s for EH1, EH2, EH3 given separately.)*	
Accidental rate	1% of predicted contribution	Uncorrelated among all detectors
Accidental spectral shape	Negligible	–
^{9}Li, ^{8}He rate	44% of predicted contribution	Correlated among same-site detectors
^{9}Li fraction	Negligible	Correlated among all detectors
^{9}Li, ^{8}He spectral shape	Negligible	–
Fast neutron rate	13%, 13%, and 17% of predicted contribution	Correlated among same-site detectors
Fast neutron spectral shape	Negligible	–
^{241}Am-^{13}C rate	45% of predicted contribution	Correlated among all detectors
^{241}Am-^{13}C spectral shape	Negligible	–
(α,n) background rate	50% of predicted contribution	Uncorrelated among all detectors
(α,n) spectral shape	Negligible	–

- $c_{\mathrm{ne},i}$: A sub-percent correction in the emitted $\overline{\nu}_e$ flux attributed to a non-equilibrium population of fission daughters, as described in [61]. This correction introduced 0.15% uncertainty in the predicted number of $\overline{\nu}_e$ interactions from one reactor.

- $S_{\mathrm{SNF}}(E_\nu, t)$: A sub-percent contribution to the $\overline{\nu}_e$ flux from spent nuclear fuel present in the cooling pool adjacent to each reactor core. An uncertainty of 100%, uncorrelated between reactors, was used for this term. This correction introduced 0.38% uncertainty in the predicted number of $\overline{\nu}_e$ interactions from one reactor.

The predictions of reactor $\overline{\nu}_e$ emission according to these models have shown a ~6% rate excess as well as a deviation in prompt positron energy spectra when compared with observations [62]. Relaxing the model uncertainties in normalization and spectral shape allowed the near detector measurements to accurately constrain the intrinsic reactor $\overline{\nu}_e$ flux and spectrum. A minor reactor-related residual uncertainty in the oscillation measurement was primarily due to the uncorrelated uncertainty in reactor thermal power and fission fractions.

c. Detector Response Detector-related systematic uncertainties were presented in Sec. IV. These included: (i) a 0.2% uncertainty in energy scale, uncorrelated between detectors, (ii) a 0.13% uncertainty in efficiency between detectors, of which 0.07% was contributed by the above-mentioned energy scale uncertainty, (iii) an absolute relation between observed positron energy and true $\overline{\nu}_e$ energy, constrained according to the model presented in Sec. III D and assumed to be common for all detectors, (iv) a slight distortion of the prompt positron spectrum caused by energy loss in the acrylic of the IAV, 4% below 1.25 MeV and 0.1% above, estimated using simulation and assumed correlated between detectors. Of these systematic effects, only the relative energy scale and efficiency variations were significant to the oscillation measurement.

While it has become common to rely on Monte-Carlo techniques to model the response of detectors to particle interactions, the specific case of $\overline{\nu}_e$ interactions in large scintillator detectors was well suited to an analytic approach. In this manner, detector systematic parameters were easily incorporated directly into the analytic response model, without incurring the computational cost of repeated Monte-Carlo simulations. Appendix A provides a description of the analytic approach to modeling the expected signal.

d. Residual Backgrounds Uncertainties in residual background rates were discussed in Sec. IV B. Rate uncertainties were assumed to be uncorrelated between detectors for the accidental background, ^{241}Am-^{13}C and (α,n)

TABLE IX. Summary of the characteristics of the five independent statistical methods (labeled A, B, C, D, and E) used to compare the $\bar{\nu}_e$ observation with the predictions of the three-flavor model of neutrino oscillation.

Model Component	Method	Description
Reactor $\bar{\nu}_e$ flux	A	Analytic prediction based on near detector observation
	B	Unconstrained absolute $\bar{\nu}_e$ spectrum, bin-to-bin uncorrelated.
	C	Huber-Mueller model [58, 59], with inflated uncertainty
	D	Unconstrained absolute $\bar{\nu}_e$ spectrum, with piece-wise continuous analytic model
	E	Unconstrained absolute $\bar{\nu}_e$ spectrum, bin-to-bin uncorrelated.
Detector response	A	Analytic model with Geant4-based correction for energy loss in the IAV acrylic
	B	Full Geant4-based detector response, tuned to reproduce the observed energy nonlinearity
	C	Analytic model with Geant4-based correction for energy loss in the IAV acrylic
	D	Analytic model with Geant4-based correction for energy loss in the IAV acrylic
	E	Analytic model including potential correlations between model components
Systematic Modeling	A	Pure χ^2 covariance approach for all systematics
	B	Full profiling of systematics via nuisance parameters, with corresponding χ^2 penalty
	C	Hybrid: Full profiling of systematics, with a covariance based penalty used to reduce the dimension of the reactor model systematics.
	Da	Full profiling of systematics, with penalties for all but reactor spectra coefficients.
	Db	Hybrid: χ^2 covariance approach for all systematics, except for reactor spectra coefficients profiled with no penalty.
	E	Full profiling of systematics via nuisance parameters, with corresponding χ^2 penalty

backgrounds. The fast neutron and β-n rate uncertainties were assumed uncorrelated between experimental halls. Uncertainty in the energy spectra of all the backgrounds were considered negligible. Of these, only the β-n background rate uncertainty was significant to the oscillation measurement.

2. Description of Models

As mentioned, five independent statistical calculations were performed. The details of each are presented in this section.

Method A was designed, in the spirit of Eq 4, to directly compare the near and far measurements with minimal dependence on models of reactor $\bar{\nu}_e$ emission. This method is identical to the method described in Ref. [28].

The data from detectors at the same site were combined into a single observed spectrum for each hall. The predicted signal in the i-th bin for the far-hall energy spectrum, $N_i^{\text{far,exp}}$, was estimated as

$$N_i^{\text{far,exp}} = w_i \left(\theta_{13}, \left| \Delta m_{\text{ee}}^2 \right| \right) \left(N_i^{\text{near,obs}} - B_i^{\text{near}} \right) + B_i^{\text{far}}, \tag{53}$$

where $N_i^{\text{near,obs}}$ was the signal observed in one of the near halls, and B_i^{near} and B_i^{far} were the estimated background contamination in each hall. The weights w_i captured the expected ratio of far signal to the near signal versus observed energy, including the dependence on oscillation via θ_{13} and $\left| \Delta m_{\text{ee}}^2 \right|$. These weights were calculated analytically, and were shown to be effectively independent of the specific model of $\bar{\nu}_e$ emission. The spectra for the six detector and eight detector data periods were kept distinct in $\boldsymbol{N}^{\text{obs}}$.

Method A used a covariance approach for χ^2 calculation, as given by Eq. 50. The statistical component of the covariance matrix was estimated analytically, while the systematic component was estimated by Monte Carlo calculations which

included the discussed systematic effects.

Method B relied on the more traditional approach of predicting the signal in all the detectors from the reactor flux model (Eq. 52) convolved with the detector response determined from a Geant4-based detector simulation. This method was used for the analysis presented in Ref. [23]. All systematic uncertainties were profiled, as reflected in Eq. 49.

To accommodate the discrepancies between the reactor flux model and observation, the normalization of each bin in the energy spectrum was allowed to deviate from the prediction. Nuisance parameters were used to implement these variations, which were uncorrelated between energy bins, but identical for all detectors. With no systematic penalty applied to these additional terms in the χ^2, the near detectors effectively constrained the predicted spectrum.

The detector response model was determined by a full Geant4-based simulation, instead of the semi-analytic model used in the other four methods. This detector response model provided a combined estimate of the various detector effects, including energy non-linearity, energy loss in the IAV acrylic, and energy resolution. The simulated energy non-linearity was adjusted so that it reproduced the non-linearity observed with data.

Method C also relied on a traditional χ^2 comparison of observation with reactor model prediction, and was used for the analysis presented in [63]. The antineutrino interaction rate and spectrum at each experimental hall was constrained based on the Huber-Mueller [58, 59] model. To avoid excess tension between the reactor model and observation, the uncertainty in the normalization of each energy bin in the model was inflated to have at least 4% uncertainty [64, 65]. The overall normalization of the reactor flux was also allowed to freely float. The detector response model was determined analytically. A profile χ^2 was used to account for systematic uncertainties. To reduce the number of nuisance parameters,
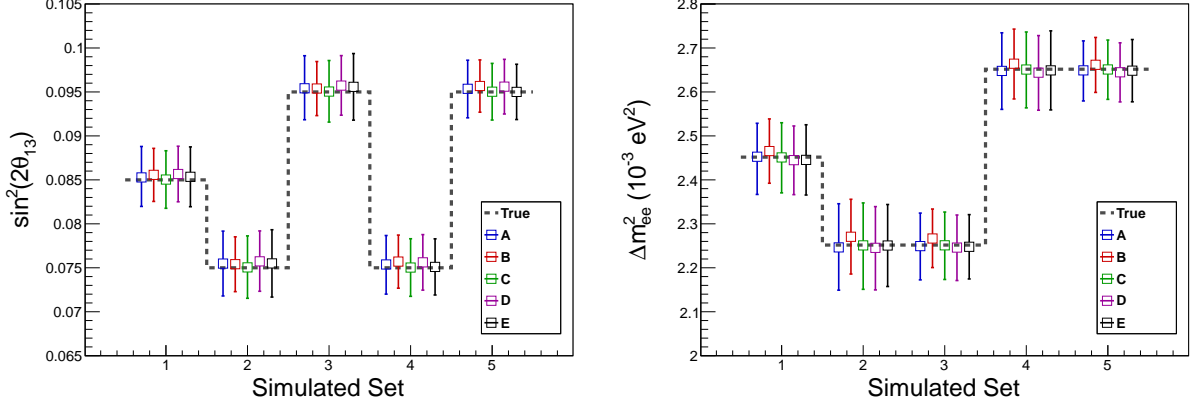
FIG. 36. Results of a validation study of the independent statistical methods (A through E) used to compare observation with the three-flavor model of neutrino oscillation. An independent program was used to generate fake observations under the assumption of a range of true values for the oscillation parameters θ_{13} and $\left|\Delta m_{ee}^2\right|$ (grey dashed lines). All methods demonstrated a consistent unbiased estimation of the true input parameters (colored points) for θ_{13} (left panel) and $\left|\Delta m_{ee}^2\right|$ (right panel). The final estimated total uncertainties, given by the error bars on each point, were also consistent between methods.

the various parameters in the reactor model were condensed to a single parameter per energy bin. The penalty on these nuisance parameters were calculated using a covariance matrix constructed from the expected variation in the Huber-Mueller model with inflated uncertainties.

Method D also used a traditional χ^2 comparison of observation with prediction based on a reactor flux model, but developed a unique approach to accommodate deviation between the flux model and observation. The $\overline{\nu}_e$ energy spectrum $S_i(E_\nu)$ of each fission parent isotope i was modeled as a parameterized piece-wise smooth function,

$$S_{ij}(E_\nu) = n_j k_{ij} \mathrm{e}^{-b_{ij}(E_\nu - E_\nu^j)}, \quad E_\nu \in \left(E_\nu^j, E_\nu^{j+1}\right), \quad (54)$$

where k_{ij} is the $\overline{\nu}_e$ intensity in the j-th energy bin. The parameters n_j allowed the combined spectral shape to vary in order to match observation, while the coefficients b_{ij} ensured that the spectrum for each isotope remained continuous.

Two versions were developed for method D in order to facilitate comparisons. In method Da, all systematic uncertainties were accommodated using nuisance parameters. In method Db, all parameters were accommodated using a covariance term, except for the reactor flux spectral parameters n_j. For both methods, the parameters n_j were profiled with no systematic penalty. The developers of method D also extended the calculation to flexibly accommodate many of the techniques seen in the other methods. As such, method D served as a valuable tool for understanding subtle differences between the various methods.

Method E was similar in design to method B, except in the approach to modeling the detector response. An analytic model was used, but special attention was given to potential correlations between the various components of the detector response. The nonlinear scintillation light emission was separately calculated for those interactions where a fraction of visible energy was lost via energy deposition in the IAV. Expected correlations between the

nonuniformity of light collection versus position and the dependence of the electronics nonlinearity with observed light were also included. The agreement between this more rigorous approach and the other analytic predictions confirmed that these potential correlations were negligible for the current analysis. This method was also used for an independent measurement of neutrino oscillation using $\overline{\nu}_e$ interactions followed by neutron capture on hydrogen. Further details of the method and the n-H measurement are given in [38].

The main features of the five statistical methods are summarized in Tab. IX. The consistency of the measurements obtained using these complementary treatments demonstrated the robustness of the final result.

3. Validation of Methods

Before application of these statistical methods to actual data, each was tested using simulation. An independent program was developed to generate simulated observations, including no statistical or systematic fluctuations. All statistical methods were then tested with the simulated samples. The resulting estimated parameter values and total uncertainties were highly consistent with the true input parameters, as demonstrated in Figure 36.

C. Analysis Results

For the final results presented here, statistical method Da was applied to the data sample provided by selection A. All results, including parameter estimation, confidence intervals, and goodness-of-fit, were consistently reproduced using the alternate statistical methods as well as when applied to selection B.

1. Rate-only Analysis

A rate-only statistical analysis was obtained by simplifying the χ^2 expression to consider only the rates observed in the eight detectors. In this case, an external estimate of $\left|\Delta m_{32}^2\right|$ was required as input. The existing value from accelerator muon neutrino disappearance, $(2.43 \pm 0.07) \times 10^{-3}\,\mathrm{eV}^2$, was used as input [14]. The rate-only measurement found

$$\sin^2 2\theta_{13} = 0.0850 \pm 0.0030(\text{stat.}) \pm 0.0028(\text{syst.}),$$
$$\frac{\chi^2}{\text{NDF}} = \frac{5.07}{8-2} = 0.85, \tag{55}$$

consistent with the simple analytic estimate given in Eq. 47. Figure 37 illustrates the ratio of the observed $\overline{\nu}_e$ signal over the no-oscillation prediction versus the effective baseline for all eight detectors. For this figure, the effective baseline L_{eff} between a given detector and the six reactors was defined as the smallest positive solution of

$$\int \sin^2(\Delta m_{\text{ee}}^2 L_{\text{eff}}/E_\nu)\frac{dN_0}{dE_\nu}dE_\nu$$
$$= \sum_j^{\text{reactors}} \int \sin^2(\Delta m_{\text{ee}}^2 L_j/E_\nu)\frac{dN_0^j}{dE_\nu}dE_\nu, \tag{56}$$

where dN_0^j/dE_ν is the expected signal in a given detector due to reactor j assuming no neutrino oscillations, $dN_0/dE_\nu = \sum_j dN_0^j/dE_\nu$, and L_j is the distance between the detector and the reactor. The deficit in the rate observed in the far detectors relative to that of the near detectors was consistent with $\overline{\nu}_e$ disappearance due to oscillation. The absolute normalization of the reactor $\overline{\nu}_e$ flux was determined from the data, ensuring a ratio of one at a baseline of zero.

2. Spectral Analysis

Figure 38 shows the reconstructed positron energy spectra for each experimental hall. Each spectrum is compared to the prediction assuming no oscillation, as well as for the three-flavor neutrino oscillation model in best agreement with the observation. The distortion of the energy spectrum at the far hall relative to near halls was consistent with oscillation, and allowed measurement of $\left|\Delta m_{\text{ee}}^2\right|$. Detailed spectral data are provided as Supplemental Material [39].

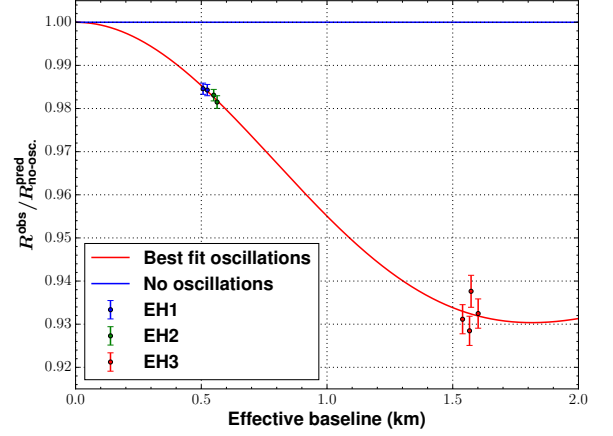The parameters of the three-flavor model in best agreement

FIG. 37. Ratio of the detected $\overline{\nu}_e$ signal to that expected assuming no oscillation versus the effective baseline for all eight antineutrino detectors. Oscillation due to θ_{13} introduced a deficit in the far detectors relative to the near detectors, and the best-fit three-flavor oscillation model from the rate-only analysis is shown (red line). Extrapolation of the model to a baseline of zero determined the absolute normalization of the reactor $\overline{\nu}_e$ flux, $R^{\text{pred}}(L = 0)$. The points representing the near (far) detectors are displaced by ± 6 m (± 30 m) for clarity.

with the observed rate and energy spectra were

$$\sin^2 2\theta_{13} =$$
$$0.0841 \pm 0.0027(\text{stat.}) \pm 0.0019(\text{syst.}),$$
$$\left|\Delta m_{\text{ee}}^2\right| =$$
$$[2.50 \pm 0.06(\text{stat.}) \pm 0.06(\text{syst.})] \times 10^{-3}\,\mathrm{eV}^2,$$
$$\Delta m_{32}^2(\text{NH}) =$$
$$[2.45 \pm 0.06(\text{stat.}) \pm 0.06(\text{syst.})] \times 10^{-3}\,\mathrm{eV}^2,$$
$$\Delta m_{32}^2(\text{IH}) =$$
$$[-2.56 \pm 0.06(\text{stat.}) \pm 0.06(\text{syst.})] \times 10^{-3}\,\mathrm{eV}^2,$$
$$\frac{\chi^2}{\text{NDF}} = \frac{234.7}{280-17} = 0.89. \tag{57}$$

The Δm_{32}^2 values were obtained using the full three-flavor expression from Eq. 2, under the assumptions of normal (NH) and inverted (IH) mass hierarchy. $\left|\Delta m_{\text{ee}}^2\right|$ was obtained from comparison of the observation with the effective oscillation model given in Eq. 3. The offset between the values of Δm_{ee}^2 and Δm_{32}^2 was identical to an analytic estimate [66].

Figure 39 compares these estimates to those obtained using the other statistical methods, as well as for the alternate sample obtained using selection B. The slight shift in the estimated value of $\sin^2 2\theta_{13}$ for selection B was consistent with statistical uncertainty from those candidate signals uncommon between the two selections. The offsets in the estimated value of Δm_{ee}^2 for the methods A, B and E were predominantly caused by the choice of binning of the prompt energy spectrum below 1.3 MeV. These three methods divided the low-energy data among multiple bins, while methods C and D combined the data from 0.7 to 1.3 MeV into a single bin. The estimated values for all methods
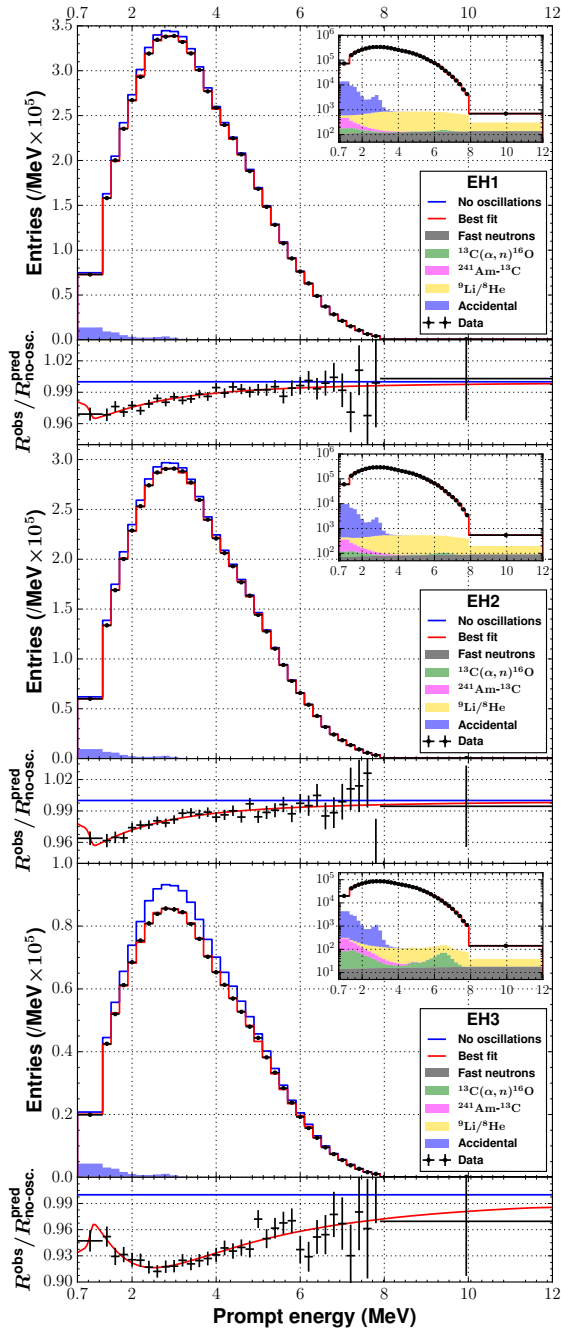
FIG. 38. Reconstructed positron energy spectra for the $\overline{\nu}_e$ candidate interactions (black points). The spectra of the detectors in each experimental hall are combined: EH1 (top), EH2 (middle), and EH3 (bottom). The measurements are compared with the prediction assuming no oscillation (blue line) and the best-fit three-flavor neutrino oscillation model (red line). The inset in semi-logarithmic scale shows the backgrounds. The ratio of the background-subtracted spectra to prediction assuming no oscillation is shown in the panel beneath each energy spectrum.

were consistent to $\lesssim 0.1\sigma$ when data below 1.3 MeV was combined into a single bin. Finely-binning the region below 1.3 MeV was also found to sizeably worsen the goodness-
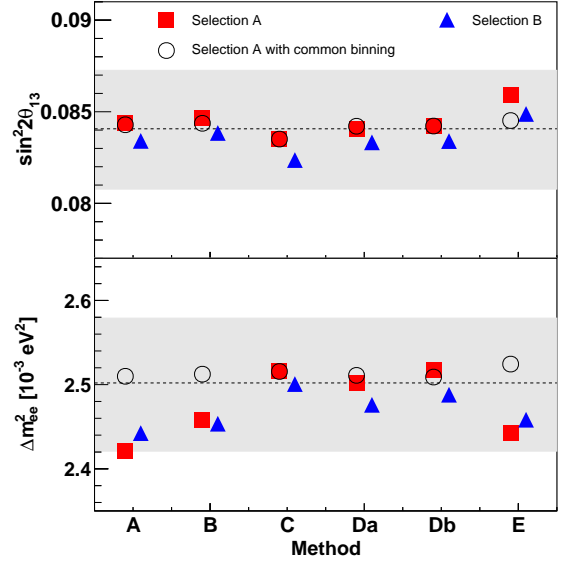
FIG. 39. A comparison of the estimated values of $\sin^2 2\theta_{13}$ (top) and Δm_{ee}^2 (bottom) obtained using various combinations of the two selected $\overline{\nu}_e$ samples, statistical methods, and reactor $\overline{\nu}_e$ flux models. The horizontal dashed lines show the best estimate of each parameter, while the gray regions show the $\pm 1\sigma$ confidence interval from the reference results (selection A, method D, and the Huber-Mueller reactor flux model). The $\lesssim 1\sigma$ offsets for methods A, B, and E were due to their choice of binning of the prompt energy spectrum, particularly below 1.3 MeV. When all methods used the same binning as method C, consistent results were obtained (open circles). See the text for details.

of-fit. For example, the χ^2 of method D increased by ~ 43 (ΔNDF=16) when the spectrum below 1.3 MeV was binned identically to method A, and the shift of the estimated value of Δm_{ee}^2 observed by method A was reproduced. Alternatively, increasing the systematic uncertainty of the finely-binned energy spectrum below 1.3 MeV also resolved the discrepancies. These observations indicated that the combined modeling of the large systematics at low energies, including relative energy scale differences and energy loss in the IAV, was insufficient for the case of a finely-binned low-energy spectrum. In contrast, the results had negligible dependence on the choice of binning above 1.3 MeV. Variations were $\lesssim 0.1\sigma$ for Δm_{ee}^2, while those for $\sin^2 2\theta_{13}$ were even smaller.

For illustrative purposes, the spectral distortion shown in Fig. 38 can be displayed as the $\overline{\nu}_e$ survival probability versus L/E_ν. The probability of $\overline{\nu}_e$ disappearance for each bin in the prompt positron energy spectrum was given by the observed signal divided by the prediction assuming no oscillation, after subtraction of background. The prediction includes corrections to the absolute reactor $\overline{\nu}_e$ flux as constrained by the observation. An average $\overline{\nu}_e$ energy $\langle E_\nu \rangle$ was estimated for each bin in the prompt positron spectra from the model of the detector response previously discussed. Given that it was not possible to determine the reactor-of-origin for each $\overline{\nu}_e$ interaction, an effective baseline L_{eff} was determined for each experimental hall, according to Eq. 56. Figure 40 shows

the observed $\overline{\nu}_e$ survival probability as a function of effective baseline L_{eff} divided by the average antineutrino energy $\langle E_\nu \rangle$. Almost one full oscillation cycle was sampled, given the range of L/E_ν values which were measured. The data from all three experimental halls were consistent with the three-flavor oscillation hypothesis.
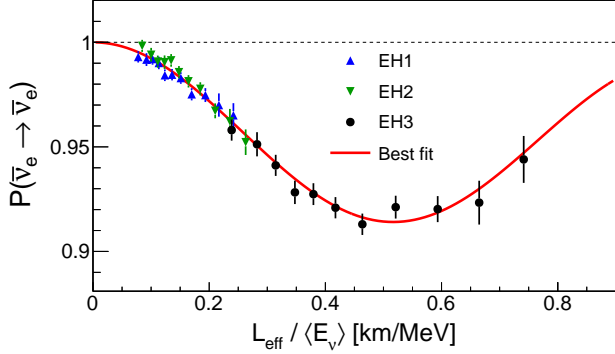

FIG. 40. Measured reactor $\overline{\nu}_e$ spectral distortion, displayed as the oscillation survival probability versus L_{eff}/E_ν. The effective propagation distance L_{eff} was estimated for each hall based on the distribution of reactors contributing to the signal (see Eq. 56). The average true $\overline{\nu}_e$ energy $\langle E_\nu \rangle$ was determined for each bin in the observed prompt positron spectrum based on the model of the detector response. The $\overline{\nu}_e$ survival probability was given by the observed signal in each bin divided by the prediction assuming no oscillation. The measurement sampled $\overline{\nu}_e$ survival over almost one full cycle, demonstrating distinct evidence in support of neutrino flavor oscillation.

The confidence regions for Δm_{ee}^2 versus $\sin^2 2\theta_{13}$ are shown in Figure 41. The confidence regions were obtained using the change of the χ^2 value relative to that of the best fit, $\Delta\chi^2 = \chi^2 - \chi_{\min}^2$, as a function of $\sin^2 2\theta_{13}$ and $\left| \Delta m_{\text{ee}}^2 \right|$. All other model parameters were profiled during the determination of the value of $\Delta\chi^2$. The confidence regions are defined as $\Delta\chi^2$ less than 2.30 (68.27% C.L.), 6.18 (95.45% C.L.), and 11.83 (99.73% C.L.). The 1-D distribution of $\Delta\chi^2$ are also provided for each individual parameter, where the alternate parameter has been profiled. A table of $\Delta\chi^2$ values as a function of $\sin^2 2\theta_{13}$ and $\left| \Delta m_{\text{ee}}^2 \right|$ is provided as Supplemental Material [39].

The precision of this measurement of θ_{13} was limited by statistics, although systematic uncertainty from differences of the $\overline{\nu}_e$ efficiency between detectors and predicted reactor flux also contributed significantly. For $\left| \Delta m_{\text{ee}}^2 \right|$, statistical and systematic uncertainties were approximately equal in size. The largest systematic uncertainty arose from potential variation in the energy calibration of the far versus near detectors, which was well characterized using multiple redundant low-energy radioactive sources. Systematic uncertainty from $\overline{\nu}_e$ interactions in the IAV also contributed.

Figure 42 compares the estimate of $\sin^2 2\theta_{13}$ with those values obtained by other experiments, while Figure 43 provides a similar comparison for measurements of Δm_{32}^2. The measurements relied on a variety of ν observations:
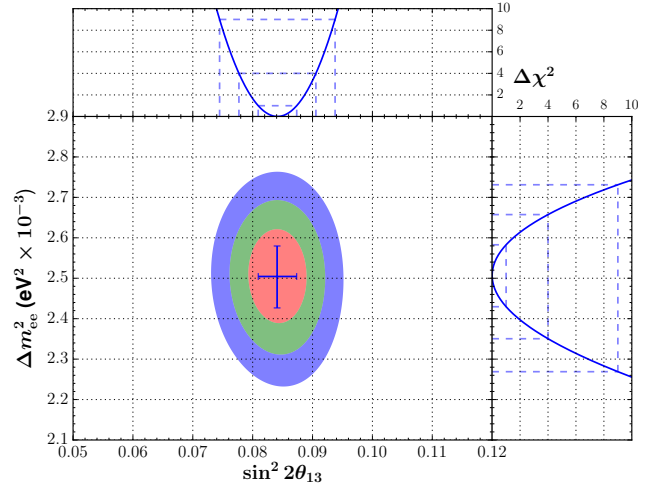
- the disappearance of MeV-energy reactor $\overline{\nu}_e$'s over

FIG. 41. Confidence regions of $\sin^2 2\theta_{13}$ and $\left| \Delta m_{\text{ee}}^2 \right|$ from a combined analysis of the prompt positron spectra and rates. The 1σ, 2σ, and 3σ 2-D confidence regions are estimated using $\Delta\chi^2$ values of 2.30 (red), 6.18 (green), and 11.83 (blue) relative to the best fit. The upper panel provides the 1-D $\Delta\chi^2$ for $\sin^2 2\theta_{13}$ obtained by profiling $\left| \Delta m_{\text{ee}}^2 \right|$ (blue line), and the dashed lines mark the corresponding 1σ, 2σ, and 3σ intervals. The right panel is the same, but for $\left| \Delta m_{\text{ee}}^2 \right|$, with $\sin^2 2\theta_{13}$ profiled. The point marks the best estimates, and the error bars display their 1-D 1σ confidence intervals.

$\sim$km distances,

- the disappearance of ν_μ produced by particle accelerators with mean energies of $\sim$600 MeV [67], $\sim$3 GeV [68], and $\sim$2 GeV [69] which had propagated distances of $\sim$295 km, $\sim$735 km, and $\sim$810 km respectively,

- the appearance of ν_e in those same neutrino beams, and

- the disappearance of ν_μ produced by particle interactions in the upper atmosphere [70, 71], with energies >1 GeV and baselines up to the diameter of the Earth.

The consistency of the values of Δm_{32}^2 measured via these various techniques firmly establishes the three-flavor model of neutrino mass and mixing.

VI. SUMMARY

From Dec. 4, 2011 to Jul. 28, 2015, the Daya Bay experiment measured the rate and energy spectrum of electron antineutrinos emitted by the six 2.9 GW$_{\text{th}}$ reactors of the Daya Bay and Ling Ao nuclear power facilities. Combining 217 days of data collected using six antineutrino detectors with 1013 days of data using eight detectors, a total of 2.5×10^6 $\overline{\nu}_e$ inverse beta decay interactions were observed. The unprecedented statistics of this sample allowed the most precise measurement of $\overline{\nu}_e$ disappearance to date. A relative comparison of the rates and positron energy spectra of the detectors located far ($\sim$1500-1950 m) relative to those near
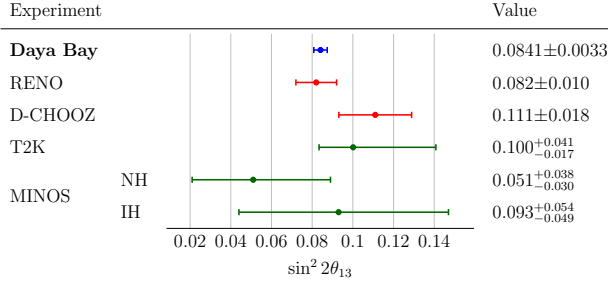
FIG. 42. Comparison of measurements of $\sin^2 2\theta_{13}$: this measurement (blue point); RENO [72] and Double-CHOOZ [73] (red points); T2K [74] and MINOS [75] (green points). The T2K and MINOS values were deduced from $2\sin^2\theta_{23}\sin^2 2\theta_{13}$, and are presented for the two cases of the normal (upper) and inverted (lower) mass hierarchy. The MINOS measurement assumed $\sin^2\theta_{23} = 0.5$, $\delta_{\mathrm{CP}} = 0$, while the T2K measurement marginalized over these unknown parameters.
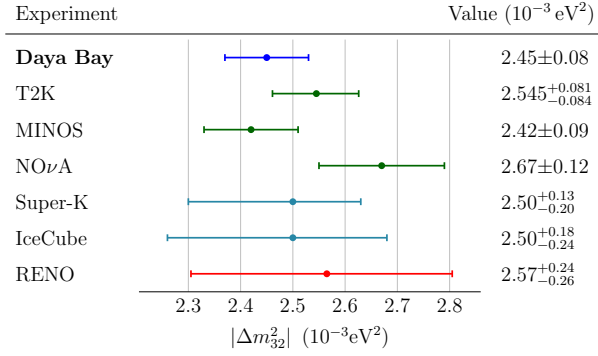
FIG. 43. Comparison of measurements of Δm^2_{32}: this measurement (blue point); RENO [72] (red point); T2K [74], MINOS [76], and NOνA [77] (green points); Super-Kamiokande [78] and IceCube [79] (cyan points). All values are given for the case of the normal mass hierarchy; the comparison for the inverted ordering was qualitatively similar.

the reactors ($\sim$350-600 m) gave $\sin^2 2\theta_{13} = 0.0841 \pm 0.0027(\mathrm{stat.})\pm 0.0019(\mathrm{syst.})$ and the effective neutrino mass-squared difference of $\left|\Delta m^2_{\mathrm{ee}}\right| = (2.50 \pm 0.06(\mathrm{stat.}) \pm 0.06(\mathrm{syst.})) \times 10^{-3}$ eV^2. This is equivalent to $\Delta m^2_{32} = (2.45 \pm 0.06(\mathrm{stat.}) \pm 0.06(\mathrm{syst.})) \times 10^{-3}$ eV^2 assuming the normal mass hierarchy, or $\Delta m^2_{32} = (-2.56 \pm 0.06(\mathrm{stat.}) \pm 0.06(\mathrm{syst.})) \times 10^{-3}$ eV^2 assuming the inverse hierarchy. The consistency with Δm^2_{32} measured using $\sim$GeV accelerator and atmospheric ν_μ disappearance strongly supports the three-flavor model of neutrino oscillation.

ACKNOWLEDGMENTS

Appendix A: Prediction of the $\overline{\nu}_e$ Signal

A method to calculate the expected rate and reconstructed positron energy spectrum from $\overline{\nu}_e$ inverse beta decay interactions in the Daya Bay detectors is summarized in this appendix. The total number of signals in the reconstructed energy interval $\{E^k_{\mathrm{rec}}, E^{k+1}_{\mathrm{rec}}\}$ of the prompt energy spectrum for detector i is given by

$$N^{\mathrm{exp}}_{ik} = N^{\mathrm{IBD}}_{ik} + N^{\mathrm{bkg}}_{ik}, \qquad (A1)$$

where N^{IBD}_{ik} are from $\overline{\nu}_e$ inverse beta decay positrons and N^{bkg}_{ik} are the contributions from backgrounds. The background spectra are displayed in Fig. 38, while their rates are summarized in Table VI. The IBD signal is given by

$$N^{\mathrm{IBD}}_{ik} = \int_{E^k_{\mathrm{rec}}}^{E^{k+1}_{\mathrm{rec}}} dE_{\mathrm{rec}} \int_{t_{\mathrm{DAQ}}} dt \, \frac{d^2 N_i}{dE_{\mathrm{rec}}dt} \, \varepsilon_i(t), \qquad (A2)$$

where $d^2 N_i(E_{\mathrm{rec}},t)/dE_{\mathrm{rec}}dt$ is the expected signal number density as a function of time and reconstructed energy. The integral includes the efficiency of detector i, $\varepsilon_i(t)$, which accounts for the slight variations in detector livetime and veto efficiency versus time. Eq. A2 was designed for use in the combined analysis of the spectrum and rate, but was also applied to the rate-only analysis by using only a single energy interval per detector.

Given the true IBD positron energy, including the energy from annihilation,

$$E_{\mathrm{true}} = E_e + m_e, \qquad (A3)$$

the expected signal number density can be obtained by a convolution of the true signal number density with the estimated detector response,

$$\frac{d^2 N_i}{dE_{\text{rec}}dt} = \int_{2m_e}^{\infty} dE_{\text{true}} \, \frac{d^2 N_i}{dE_{\text{true}}dt} \, P(E_{\text{rec}}; E_{\text{true}}). \quad \text{(A4)}$$

The estimated detector response, $P(E_{\text{rec}}; E_{\text{true}})$, describes the conditional probability of obtaining a reconstructed energy E_{rec} given a true energy of E_{true}.

The expected number density of IBD signals per interval of true positron energy,

$$\frac{d^2 N_i}{dE_{\text{true}}dt} = N_i^p \int_{-1}^{1} d\cos\theta_e \frac{d\sigma}{d\cos\theta_e} \frac{d^2 N_i^\nu}{dE_\nu dt} \frac{dE_\nu}{dE_{\text{true}}}. \quad \text{(A5)}$$

is the product of the number density of antineutrinos, $d^2 N_i^\nu / dE_\nu dt$, the number of protons in the detector, N_i^p, and the $\overline{\nu}_e$-proton IBD interaction cross section, $d\sigma/d\cos\theta_e$. The emission angle of the positron, θ_e, was not resolved by the detectors, and so it is integrated in this calculation.

The IBD cross-section as a function of positron scattering angle and $\overline{\nu}_e$ energy, $d\sigma/d\cos\theta_e$, was taken from [17]. This tree-level calculation was performed up to first order in $1/m_p$, and accounted for recoil, weak magnetism, and inner radiative corrections.

The dependence of the positron's energy E_e and scattering angle θ_e on antineutrino energy E_ν is

$$E_\nu = E_\nu(E_e, \cos\theta_e) = \frac{E_e + \widetilde{\Delta}}{1 - \frac{E_e}{m_p}(1 - \beta_e \cos\theta_e)}, \quad \text{(A6)}$$

where $\widetilde{\Delta} = (m_n^2 - m_p^2 - m_e^2)/2m_p \approx m_n - m_p$ and β_e is the positron velocity. The corresponding Jacobian is,

$$\frac{dE_\nu}{dE_{\text{true}}} = \frac{1 + \frac{E_\nu}{m_p}(1 - \beta_e^{-1} \cos\theta_e)}{1 - \frac{E_e}{m_p}(1 - \beta_e \cos\theta_e)}, \quad \text{(A7)}$$

and is shown in Fig. 44 as a function of positron energy E_e.

The number density of reactor $\overline{\nu}_e$ passing through the detector is estimated as

$$\frac{d^2 N_i^\nu(E_\nu, t)}{dE_\nu dt} = \sum_j \frac{d^2 R_\nu^j(E_\nu, t)}{dE_\nu dt} \frac{P_{\text{sur}}(E_\nu, L_{ij})}{4\pi L_{ij}^2}, \quad \text{(A8)}$$

where $d^2 R_\nu^j(E_\nu, t)/dE_\nu dt$ is given by Eq. 52, L_{ij} is the distance between centers of reactor core j and detector i, and $P_{\text{sur}}(E_\nu, L)$ is the $\overline{\nu}_e$ survival probability given by Eq. 2.

The detector response, $P(E_{\text{rec}}; E_{\text{true}})$, accounted for the detector and reconstruction effects discussed in Sec. III. Two approaches were used to estimate this relationship. The first method decomposed the detector response into three prominent components:

- $P(E_{\text{dep}}; E_{\text{true}})$: The probability to have an energy E_{dep} deposited in the scintillator for a given true

positron energy E_{true}. The two energies are usually identical, except for ∼1% of positrons which lost a fraction of their energy in the inner acrylic vessel. This component, commonly referred to as the IAV effect, was modeled via a Geant4-based simulation.
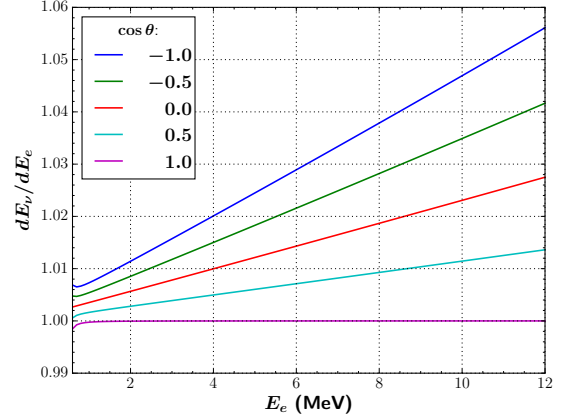

FIG. 44. The Jacobian dE_ν/dE_{true} as a function of positron energy E_e for a range of values of the positron emission angle $\cos\theta_e$.

- $P(\bar{E}_{\text{rec}}; E_{\text{dep}})$: The probability to obtain a mean reconstructed energy $\bar{E}_{\text{rec}}$ given a given deposited energy E_{dep}. This component accounts for the nonlinear light emission of the scintillator and the nonlinear response of the PMT charge measurement, and is given by the function shown in Fig. 15.

- $P(E_{\text{rec}}; \bar{E}_{\text{rec}})$: The probability to obtain a reconstructed energy E_{rec} for a given expected mean reconstructed energy $\bar{E}_{\text{rec}}$. This term accounts for the detector resolution, and was modeled as a Gaussian distribution about $\bar{E}_{\text{rec}}$ with a standard deviation given by Eq. 14.

The total detector response is simply the consecutive convolution of these three distributions. The distributions $P(E_{\text{dep}}; E_{\text{true}})$ and $P(\bar{E}_{\text{rec}}; E_{\text{dep}})$, as well as the combined distribution $P(E_{\text{rec}}; E_{\text{true}})$, are provided as Supplemental Material [39].

The second method used full Geant4-based simulation to construct the detector response as a single unified distribution $P(E_{\text{rec}}; E_{\text{true}})$. The simulation was adjusted to reproduce the observed calibration data, and naturally included the potential interplay between the different components of the detector response. In principle, this technique allowed for more accurately modeling of the detector response near $E_{\text{rec}} \simeq 1$ MeV where the effect of the IAV was most significant. The two methods yielded consistent predictions for the observed prompt energy spectrum.

[1] B. T. Cleveland, T. Daily, R. Davis, Jr., J. R. Distel, K. Lande, C. K. Lee, P. S. Wildenhain, and J. Ullman, Astrophys. J. **496**, 505 (1998).

[2] F. Kaether, W. Hampel, G. Heusser, J. Kiko, and T. Kirsten, Phys. Lett. **B685**, 47 (2010), arXiv:1001.2731 [hep-ex].

[3] J. N. Abdurashitov *et al.* (SAGE Collaboration), Phys. Rev. **C80**, 015807 (2009), arXiv:0901.2200 [nucl-ex].

[4] K. S. Hirata *et al.* (Kamiokande-II Collaboration), Phys. Rev. Lett. **65**, 1297 (1990).

[5] Y. Fukuda *et al.* (Super-Kamiokande Collaboration), Phys. Rev. Lett. **81**, 1158 (1998), [Erratum: Phys. Rev. Lett.81,4279(1998)], arXiv:hep-ex/9805021 [hep-ex].

[6] Y. Fukuda *et al.* (Super-Kamiokande Collaboration), Phys. Rev. Lett. **81**, 1562 (1998).

[7] M. H. Ahn *et al.* (K2K Collaboration), Phys. Rev. Lett. **90**, 041801 (2003).

[8] Q. R. Ahmad *et al.* (SNO Collaboration), Phys. Rev. Lett. **87**, 071301 (2001).

[9] Q. R. Ahmad *et al.* (SNO Collaboration), Phys. Rev. Lett. **89**, 011301 (2002).

[10] S. Abe *et al.* (KamLAND Collaboration), Phys. Rev. Lett. **100**, 221803 (2008).

[11] A. de Gouvea *et al.* (Intensity Frontier Neutrino Working Group), (2013), arXiv:1310.4340 [hep-ex].

[12] A. de Gouvea, Mod. Phys. Lett. **A19**, 2799 (2004), arXiv:hep-ph/0503086 [hep-ph].

[13] R. N. Mohapatra *et al.*, Rept. Prog. Phys. **70**, 1757 (2007), arXiv:hep-ph/0510213 [hep-ph].

[14] K. A. Olive *et al.* (Particle Data Group), Chin.Phys. **C38**, 090001 (2014), and 2015 update.

[15] M. Apollonio *et al.* (CHOOZ Collaboration), Eur. Phys. J. **C27**, 331 (2003).

[16] F. Boehm *et al.*, Phys. Rev. **D64**, 112001 (2001), arXiv:hep-ex/0107009 [hep-ex].

[17] P. Vogel and J. F. Beacom, Phys. Rev. **D60**, 053003 (1999), arXiv:hep-ph/9903554 [hep-ph].

[18] H. Minakata, H. Nunokawa, S. J. Parke, and R. Zukanovich Funchal, Phys.Rev. **D74**, 053008 (2006).

[19] L. Mikaelyan and V. Sinev, Phys. Atom. Nucl. **62**, 2008 (1999), [Yad. Fiz.62,2177(1999)], arXiv:hep-ph/9811228 [hep-ph].

[20] F. P. An *et al.* (Daya Bay Collaboration), (2007), arXiv:hep-ex/0701029.

[21] J. K. Ahn *et al.* (RENO Collaboration), (2010), arXiv:1003.1391 [hep-ex].

[22] F. Ardellier *et al.* (Double Chooz Collaboration), (2006), arXiv:hep-ex/0606025.

[23] F. P. An *et al.* (Daya Bay Collaboration), Phys. Rev. Lett. **108**, 171803 (2012).

[24] J. Ahn *et al.* (RENO Collaboration), Phys. Rev. Lett. **108**, 191802 (2012).

[25] Y. Abe (Double Chooz Collaboration), Phys. Rev. Lett. **108**, 131801 (2012).

[26] K. Abe *et al.* (T2K Collaboration), Phys. Rev. **D91**, 072010 (2015), arXiv:1502.01550 [hep-ex].

[27] P. Adamson *et al.* (NOvA Collaboration), Phys. Rev. Lett. **116**, 151806 (2016), arXiv:1601.05022 [hep-ex].

[28] F. P. An *et al.* (Daya Bay Collaboration), Phys. Rev. Lett. **115**, 111802 (2015), arXiv:1505.03456 [hep-ex].

[29] F. P. An *et al.* (Daya Bay Collaboration), Nucl. Instrum. Meth. **A685**, 78 (2012), arXiv:1202.6181 [physics.ins-det].

[30] F. P. An *et al.* (Daya Bay Collaboration), Nucl. Instrum. Meth. **A811**, 133 (2016), arXiv:1508.03943 [physics.ins-det].

[31] W. Beriguete *et al.*, Nucl. Instrum. Meth. **A763**, 82 (2014), arXiv:1402.6694 [physics.ins-det].

[32] J. L. Liu, B. Cai, R. Carr, D. A. Dwyer, W. Q. Gu, G. S. Li, X. Qian, R. D. McKeown, R. H. M. Tsang, W. Wang, *et al.*, Nucl. Instr. Meth. A **750**, 19 (2014).

[33] F. P. An *et al.* (Daya Bay Collaboration), Nucl. Instr. Meth. A **773**, 8 (2015).

[34] G. Knoll, *Radiation Detection and Measurement (4th ed.)* (John Wiley, Hoboken, NJ, 2010).

[35] E. H. Bellamy *et al.*, Nucl. Instr. Meth. A **339**, 468 (1993).

[36] T. Skwarnicki, Ph.D Thesis, DESY F31-86-02(1986), Appendix E; M.J. Oreglia, Ph.D Thesis, SLAC-236(1980), Appendix D; J. E. Gaiser, Ph.D Thesis, SLAC-255(1982), Appendix F.

[37] S. Agostinelli *et al.* (GEANT4 Collaboration), Nucl. Instrum. Meth. **A506**, 250 (2003).

[38] F. P. An *et al.* (Daya Bay Collaboration), Phys. Rev. **D93**, 072011 (2016), arXiv:1603.03549 [hep-ex].

[39] See the Supplemental Material at (provide link) for the following tabulated data: the observed prompt energy spectra for $\overline{\nu}_e$ inverse beta decay candidates and estimated backgrounds for each experimental hall, the distribution of $\Delta\chi^2$ versus $\sin^2(2\theta_{13})$ and Δm_{ee}^2, and the components of the detector response model $P(E_{rec}; E_{true})$.

[40] F. P. An *et al.* (Daya Bay Collaboration), Phys. Rev. D **90**, 071101 (2014).

[41] S. Abe *et al.* (KamLAND Collaboration), Phys. Rev. **C81**, 025807 (2010), arXiv:0907.0066 [hep-ex].

[42] L.-j. Wen, J. Cao, K.-B. Luk, Y.-q. Ma, Y.-f. Wang, and C.-g. Yang, Nucl. Instrum. Meth. **A564**, 471 (2006), arXiv:hep-ex/0604034 [hep-ex].

[43] S. W. Li and J. F. Beacom, Phys. Rev. **D92**, 105033 (2015), arXiv:1508.05389 [physics.ins-det].

[44] D. R. Tilley, J. H. Kelley, J. L. Godwin, D. J. Millener, J. E. Purcell, C. G. Sheu, and H. R. Weller, Nucl. Phys. **A745**, 155 (2004).

[45] G. Nyman *et al.*, Nucl. Phys. A **510**, 189 (1990).

[46] T. Bjornstad *et al.* (ISOLDE Collaboration), Nucl.Phys. **A366**, 461 (1981).

[47] J. Liu, R. Carr, D. A. Dwyer, W. Q. Gu, G. S. Li, R. D. McKeown, X. Qian, R. H. M. Tsang, F. F. Wu, and C. Zhang, Nucl. Instrum. Meth. **A797**, 260 (2015), arXiv:1504.07911 [physics.ins-det].

[48] F. P. An *et al.* (Daya Bay Collaboration), Chin. Phys. C **37**, 011001 (2013).

[49] W. Q. Gu, G. F. Cao, X. H. Chen, X. P. Ji, G. S. Li, J. J. Ling, J. Liu, X. Qian, and W. Wang, (2015), arXiv:1512.00295 [physics.ins-det].

[50] J. Zhao, Z. Y. Yu, J. L. Liu, X. B. Li, F. H. Zhang and D. M. Xia, Chin. Phys. C **38**, 116201 (2014).

[51] M. Wojcik and G. Zuzel, J. Radioanal. Nucl. Chem. **296**, 639 (2013).

[52] K. Shibata *et al.*, J. of Nucl. Sci. and Tech. **48**, 1 (2011).

[53] N. Otuka *et al.*, Nuclear Data Sheets **120**, 272 (2014).

[54] http://www.srim.org.

[55] F. P. An *et al.* (Daya Bay), (2016), arXiv:1607.05378 [hep-ex].

[56] Z. Djurcic, J. Detwiler, A. Piepke, V. J. Foster, L. Miller, *et al.*, J.Phys. **G36**, 045002 (2009), arXiv:0808.0747 [hep-ex].

[57] X. B. Ma *et al.*, Phys.Rev. **C88**, 014605 (2013).

[58] P. Huber, Phys. Rev. C **84**, 024617 (2011).

[59] T. Mueller *et al.*, Phys. Rev. C **83**, 054615 (2011).

[60] J. Cao, Nucl. Phys. B. (Proc. Suppl.) **229-232**, 205 (2012), arXiv:1101.2266 [hep-ex].

[61] V. I. Kopeikin, Phys. Atom. Nucl. **75**, 143 (2012), [Yad. Fiz.75N2,165(2012)].

[62] F. P. An *et al.* (Daya Bay Collaboration), Phys. Rev. Lett. **116**, 061801 (2016), arXiv:1508.04233 [hep-ex].

[63] F. P. An *et al.* (Daya Bay Collaboration), Phys. Rev. Lett. **112**, 061801 (2014).

[64] A. C. Hayes, J. L. Friar, G. T. Garvey, G. Jungman, and G. Jonkmans, Phys. Rev. Lett. **112**, 202501 (2014), arXiv:1309.4146 [nucl-th].

[65] A. C. Hayes, J. L. Friar, G. T. Garvey, D. Ibeling, G. Jungman, T. Kawano, and R. W. Mills, Phys. Rev. **D92**, 033015 (2015), arXiv:1506.00583 [nucl-th].

[66] H. Nunokawa, S. J. Parke, and R. Zukanovich Funchal, Phys. Rev. **D72**, 013009 (2005), arXiv:hep-ph/0503283 [hep-ph].

[67] K. Abe *et al.* (T2K Collaboration), Phys. Rev. Lett. **112**, 181801 (2014).

[68] P. Adamson *et al.* (MINOS Collaboration), Phys. Rev. Lett. **112**, 191801 (2014), arXiv:1403.0867 [hep-ex].

[69] P. Adamson *et al.* (NOvA Collaboration), Phys. Rev. **D93**, 051104 (2016), arXiv:1601.05037 [hep-ex].

[70] R. Wendell (Super-Kamiokande Collaboration), XXVI International Conference on Neutrino Physics and Astrophysics (2014), arXiv:1412.5234 [hep-ex].

[71] M. G. Aartsen *et al.* (IceCube Collaboration), Phys. Rev. **D91**, 072004 (2015), arXiv:1410.7227 [hep-ex].

[72] J. H. Choi *et al.* (RENO Collaboration), Phys. Rev. Lett. **116**, 211801 (2016), arXiv:1511.05849 [hep-ex].

[73] M. Ishitsuka (Double Chooz Collaboration), 51$^{\text{st}}$ Rencontres de Moriond, Electroweak Interactions and Unified Theories (2016).

[74] K. Iwamoto (T2K Collaboration), 38th International Conference on High Energy Physics (2016).

[75] P. Adamson *et al.* (MINOS Collaboration), Phys. Rev. Lett. **110**, 171801 (2013).

[76] J. Evans (MINOS and MINOS+ Collaborations), XXVII International Conference on Neutrino Physics and Astrophysics (2016).

[77] P. Vahle (NOνA Collaboration), XXVII International Conference on Neutrino Physics and Astrophysics (2016).

[78] S. Moriyama (Super-Kamiokande Collaboration), XXVII International Conference on Neutrino Physics and Astrophysics (2016).

[79] J. Koskinen (IceCube Collaboration), XXVII International Conference on Neutrino Physics and Astrophysics (2016).